NASA
Technical
Paper
2420
C.2

AVSCOM
Technical
Report
85-B-2

June 1985

Wind-Tunnel Evaluation of a 21-Percent-Scale Powered Model of a Prototype Advanced Scout Helicopter

Arthur E. Phelps III
and John D. Berry

NASA

Wind-Tunnel Evaluation of a 21-Percent-Scale Powered Model of a Prototype Advanced Scout Helicopter

Arthur E. Phelps III
and John D. Berry

Structures Laboratory
USAAVSCOM Research and Technology Laboratories
Langley Research Center
Hampton, Virginia

Summary

A 21-percent-scale powered model of a prototype configuration of the U.S. Army advanced scout helicopter was tested in the Langley 4- by 7-Meter Tunnel. The model included a nonrotating mast-mounted sight and used a fully articulated, four-bladed general research rotor driven by a 29-hp electric motor. The investigation was exploratory in nature and was conducted to define the overall aerodynamic characteristics of the Army Helicopter Improvement Program (AHIP) configuration, to determine the effects of the rotor on the aerodynamic characteristics, and to evaluate the effect of a mast-mounted sight on the stability characteristics of the aircraft. Tests were conducted for angles of attack from $-16°$ to $16°$, angles of sideslip from $-30°$ to $30°$, advance ratios from 0 (hover) to 0.22, based on a hover tip speed of 650 ft/sec, and thrust coefficients from 0.0018 to 0.0065. Six components of force and moment data were measured for both the rotor and the airframe at each data point, and the results have been reduced both to nondimensional form and to equivalent full-scale dimensional form customarily used by the U.S. helicopter industry.

The results of the investigation showed that the prototype aircraft was longitudinally unstable with angle of attack for all configurations and flight conditions tested. Evaluation of the airframe forces and moments and analysis of smoke-flow visualization indicated that the primary cause of the longitudinal instability was a strong turbulent wake shed by the engine pylon, rotor hub, and pitch-change pushrods interfering with the horizontal tail. This wake caused premature stalling of the tail and reduced dynamic pressure at the tail. The addition of the mast-mounted sight had little effect on the stability characteristics of the model, but the wake shed from the sight caused an alteration in the rotor lift distribution and resulted in very high interference drag for the sight.

Introduction

The Army Helicopter Improvement Program (AHIP) is the latest in a series of U.S. Army efforts to develop and acquire an advanced scout helicopter (ref. 1). Although earlier work dating back to 1972 envisioned an entirely new airframe, a 1980 review of Army requirements by the Aviation Systems Acquisition Review Committee (ASARC) led to the recommendation for a competitive modification program to provide an improved version of the existing OH-58A or OH-6A light observation-type helicopters as a near-term advanced scout helicopter. Subsequently, a contract was awarded to Bell Helicopter Textron, Fort Worth, Texas, for the development of the scout helicopter (referred to as AHIP) from the OH-58A. One of the more unusual features to be incorporated in the AHIP is a mast-mounted sight (MMS) located above the rotor hub. The sight contains a laser range finder and target designator, a television for daytime imagery, and a forward-looking infrared radar (FLIR) system for night imagery. The location of the sight above the rotor hub was chosen to permit the aircraft to be partially concealed behind terrain features or vegetation in order to evade detection and targeting.

The present investigation was conducted to define the basic aerodynamic characteristics of the aircraft without the MMS, to investigate the effect of the rotor wake on the basic aerodynamic characteristics of the airframe, and to determine the gross effects of the MMS installation, particularly with respect to drag and stability.

Since the primary purpose of the test was to evaluate major aircraft flow-field characteristics rather than to define rotor performance parameters or to evaluate dynamic properties of the rotor itself, an existing general-research model rotor was used in conjunction with a 21-percent-scale model of the prototype AHIP airframe.

Rotor-off tests, conducted to assess the relative interference effects between the airframe and the rotor wake, were made over a range of angles of attack and sideslip for a variety of configurations including hub on and hub off. Free-stream dynamic pressure for the rotor-off tests was held constant at a dynamic pressure of 20.1 lb/ft^2, which corresponded to a rotor-on advance ratio of 0.20.

Rotor-on tests were conducted over a range of advance ratios from 0 (hover) to 0.22 for values of thrust coefficients ranging from 0.0018 to 0.0065. Rotor rotational speed was kept constant at 1862 rpm, which provided a tip speed of 650 ft/sec in hover. Six components of force and moment data were recorded separately for both the airframe and rotor at each test point.

Symbols

Data in this report are referenced to the axis system shown in figure 1, and the location of the moment center is shown in the general-arrangement drawing in figure 2. Measurements were made in the U.S. Customary Units and are presented in both dimensional and nondimensional form. Dimensional data have been converted to equivalent full-scale values and are presented in U.S. Customary Units since the primary users of the data are intended to be U.S. government agencies and their contractors.

A	rotor disk area, 34.907 ft^2
C_D	drag coefficient, $D/\rho(\Omega R)^2 A$ (for rotor-off cases, $\Omega R = 650$ ft/sec)
C_L	lift coefficient, $L/\rho(\Omega R)^2 A$ (for rotor-off cases, $\Omega R = 650$ ft/sec)
C_l	rolling-moment coefficient, $M_X/\rho(\Omega R)^2 AR$ (for rotor-off cases, $\Omega R = 650$ ft/sec)
C_m	pitching-moment coefficient, $M_Y/\rho(\Omega R)^2 AR$ (for rotor-off cases, $\Omega R = 650$ ft/sec)
C_n	yawing-moment coefficient, $M_Z/\rho(\Omega R)^2 AR$ (for rotor-off cases, $\Omega R = 650$ ft/sec)
C_T	rotor thrust coefficient, $T/\rho A(\Omega R)^2$
C_Y	side-force coefficient, $F_Y/\rho(\Omega R)^2 A$
D	drag force, lbf
F_Y	side force, lbf
L	lift force, lbf
M_X	rolling moment, in-lbf
M_Y	pitching moment, in-lbf
M_Z	yawing moment, in-lbf
q	free-stream dynamic pressure, $\frac{1}{2}\rho V_\infty^2$, lb/ft^2
R	rotor radius, 40.00 in.
T	rotor resultant force (thrust), $\sqrt{L^2 + D^2 + F_Y^2}$, lbf
V_{tip}	rotor tip speed in hover, $\Omega R/12$, ft/sec
V_∞	free-stream speed, ft/sec
α	fuselage angle of attack, deg
β	fuselage angle of sideslip, deg
Δ	change due to interference
μ	rotor advance ratio V_∞/V_{tip}
ρ	atmospheric density, slugs/ft^3
χ	rotor wake skew angle, deg
Ω	rotor rotational speed, rad/sec

Subscripts:

B	airframe, excluding rotating hub and controls
R	rotor, including hub and controls
T	combined body and rotor

Abbreviations:

AHIP	Army Helicopter Improvement Program
ASARC	Aviation Systems Acquisition Review Committee
FLIR	forward-looking infrared radar
MMS	mast-mounted sight

Model and Apparatus

General

Tests were conducted in the Langley 4- by 7-Meter Tunnel by using the 21-percent-scale model shown in figures 2 to 4. The fuselage portion of the model, including the engine pylon, consisted of the following parts: a fiberglass-reinforced plastic shell made in two halves and mounted to the body balance by means of an aluminum bulkhead, and a tail boom supporting the tails. The horizontal and vertical tails, wire cutters, and landing-gear skids were all removable in order to allow assessment of the individual effects of the various components. The pylon and fuselage were not separable, and there was no simulation of engine inlet or exhaust flows.

The model was equipped with a main rotor drive system and four-bladed rotor, but there was no tail rotor simulation. The rotor drive system used for the tests was an existing small general research unit designed to provide rotor power for a wide range of helicopter models. The rotor system consists of a 29-hp, three-phase synchronous electric motor, a two-stage transmission having a 4-to-1 reduction ratio, a swashplate-type collective and cyclic pitch rotor control system, and a four-bladed fully articulated hub, all mounted on a spring-damper gimbal designed to decouple rotating natural frequencies from the support-system frequencies. The rotor drive system, including the gimbal, is mounted on a six-component strain-gauge balance that is used to measure rotor loads, and a second balance supports the fuselage shell independently of the rotor and transmission. The location of the two balances is shown in figure 4, and the moment reference center for data reduction purposes is shown in figure 2.

The four-bladed rotor was an existing rotor and hub that has been used in previous studies and, hence, was not true to scale. The rationale for the use of this rotor is discussed in detail in the next section entitled "Deviation From Scale." Pertinent configuration details of the rotor blades used in the test program are given in figures 5 and 6. The model blades were of composite construction utilizing prepreg graphite cloth, polyurethane foam cores,

2

fiberglass and epoxy external skins, and tungsten leading-edge balance weights, as shown in figure 5. Instrumentation was provided on the hub and rotor blades to allow continuous monitoring of rotor in-plane and out-of-plane motion and blade internal bending and torsional stresses. Data were transmitted from the rotating system to the fixed system by means of a 36-channel slip-ring assembly installed in the bottom of the rotor shaft during the MMS-off portion of the investigation. A special fixture including eight slip-ring channels was attached to the hub to provide a mount for the nonrotating MMS during the portions of the investigation in which the MMS was installed.

Deviation From Scale

Model testing was desired to answer four specific questions:

1. What were the basic aerodynamic characteristics of the model?
2. How did the presence of the thrusting rotor affect the basic aerodymamic characteristics?
3. What was the gross effect of the MMS on the overall aerodynamic characteristics of the model?
4. What was the effect of the MMS on the stability characteristics of the model?

Based on a number of other experimental studies, it was recognized that a high-fidelity, dynamically scaled, powered model would provide the best evaluation of the AHIP aerodynamic characteristics, but that such a model would require extensive time and cost for development. However, since the overall aerodynamic properties were of primary interest, the objective of the test could be met by using a model having substantial geometric similarity without resorting to the additional expense of high-fidelity rotor dynamic similarity.

It was therefore decided to use existing hardware to the maximum extent possible for the present investigation. A set of rotor blades, having a 3-to-1 taper ratio over the outer 20-percent span, were available for immediate use and had already been tested in hover by using the small rotor drive system. The rotor had a diameter of 80.00 in., which dictated a model scale of 19.05 percent based on a full-scale AHIP rotor diameter of 35 ft. Unfortunately, the rotor drive system would not fit into a 19-percent-scale body without substantial modifications to the body contours. By increasing the model scale to 21 percent, it was possible to mount the drive system inside the model and restrict the contour changes to minor modifications in the aft-fuselage/tail-boom intersection area. The extent of these changes is shown in figure 6. Although the use of a 21-percent-scale body

resulted in a rotor diameter approximately 9 percent too small, it was felt that the gross effects of the rotor would be sufficiently well modeled to warrant preliminary testing, particularly in view of the time and cost advantages involved. The total cost of the model, as eventually configured, was approximately 5 percent of the minimum estimated cost for a fully scaled model with an aeroelastically scaled rotor. The known deviations from precise scale are summarized in table I.

Instrumentation and Data Analysis

The primary instrumentation used for this investigation consisted of the two six-component strain-gauge balances mentioned earlier, existing tunnel flow-measurement transducers, and data signals passed from the rotor and model attitude control systems. The rotor signals were low-pass filtered and were recorded by the wind-tunnel static data acquisition system, which provided no measure of the signal dynamics. The static data system allows continuous acquisition of the transducer signals and computation of coefficients and balance interactions; the resulting "real-time" displays allow the test conductor to establish test conditions based on computed values such as total lift and drag. Data points were taken by averaging sequential measurements over a selected interval and then storing the resulting average on both magnetic tape and a disk-based data-base system. Summaries and plots of the data points were available from the system as soon as a run (sequence of data points) was recorded.

Each data point represents a statistical mean of 100 points taken at the rate of 20 points per second for a period of 5 sec. Strain-gauge balance data were low-pass filtered and sampled randomly; that is, there was no specific correlation between blade azimuthal position and data sampling time. Accordingly, the data presented herein represent steady-state time-averaged conditions over a sample time of approximately 150 rotor revolutions. A "safety of flight" station was established to protect the model; this station provided a test engineer with the capability to monitor the dynamics of the model system. Selected signals were recorded by frequency modulation (FM) on magnetic tape for "postmortem" analysis in the event of a catastrophic model failure.

The method of reference 2 was used to compute corrections to the data due to jet-boundary interactions. The analysis showed that the maximum correction to be applied to the data would be an angle-of-attack correction of less than 0.2° and a free-stream dynamic-pressure correction of less than 0.15 percent at the worst case condition of $\mu = 0.04$ and $C_T = 0.0064$ (at 225 lbf of rotor thrust). These

TABLE I. CONFIGURATION DETAILS[a]

Main rotor characteristics	Full scale	0.21 scale	As tested
Diameter	35.00 ft	88.20 in.	80.00 in.
Solidity, thrust weighted	0.0580	0.0580	0.0825
Taper ratio, Tip chord/Root chord . .	1.75/1	1.75/1	3/1
Root cutout, percent of R	19.60	19.60	23.13
Twist, deg	−16 (nonlinear)	−16 (nonlinear)	−16 (linear)
Airfoil, rectangular section	BHTI M 406183	BHTI M 406183	NACA 0012
Hover tip speed, ft/sec	724	724	650

[a]The configuration had the following modifications and/or restrictions: no tail rotor simulation on model; no engine inlet or exhaust flow on model; nonscale main rotor hub and pushrods on model; incorrect contour on fuselage aft end; and no modeling of minor appendages to fuselage, such as small antennas, hinges, door handles, bolt heads, and similar items.

values were judged to be sufficiently small with the result that no jet-boundary corrections have been applied to the data.

Tests and Procedures

The investigation was conducted in the Langley 4- by 7-Meter Tunnel with the movable test-section walls and ceiling raised to form an open-jet configuration that was closed on the bottom, as can be seen in figure 3. The model and strain-gauge balances were attached to a vertical strut, which contained the mechanism for changing angle of attack and which could be raised or lowered through a range of about 1 rotor diameter. Changes in sideslip angle were accomplished by rotating the large turntable to which the model strut support structure was secured.

Tests were conducted for both rotor-on and rotor-off configurations of the model. For the rotor-off tests, free-stream dynamic pressure was held constant at $q = 20.1$ lb/ft^2, which corresponded to a rotor-on advance ratio of 0.20. Longitudinal aerodynamic characteristics were obtained by sweeping the model through an angle-of-attack range from $-16°$ to $16°$ at an angle of sideslip of $0°$, and lateral-directional characteristics were obtained by sweeping the model through an angle-of-sideslip range from $-30°$ to $30°$ at angles of attack of $-6°$, $0°$, and $6°$. All hub-on rotor-off tests were conducted with the hub rotating at 1862 rpm and with the control pushrods installed; all hub-off tests were conducted with the rotor drive shaft extending above the fuselage, but with the control pushrods removed. Thus, the wake from the exposed rotor shaft was included in the hub-off data.

Rotor-on tests were conducted over a range of advance ratios from 0 (hover) to 0.22, based on a rotor tip speed of 650 ft/sec. Forward-flight testing with the rotor on was conducted with the model positioned so that the rotor center of rotation was located on the tunnel centerline, which was 1.09 rotor diameters above the tunnel floor. Variations in advance ratio were accomplished by varying tunnel dynamic pressure over a range from 0.80 lb/ft^2 for $\mu = 0.04$ to 24.3 lb/ft^2 for $\mu = 0.22$. Rotor rotational speed was maintained constant at 1862 rpm for all wind-on testing, and the rotor tip path plane was maintained perpendicular to the rotor shaft (with shaft axis and tip path plane axis parallel). Control of the tip path plane orientation was accomplished by the model pilot monitoring the blade out-of-plane (flapping) motion transducer and "flying" the rotor cyclic controls to produce zero 1-per-revolution blade cyclic flapping motion, thus leaving only blade coning and small values of flapping greater than 1 per revolution.

Wind-on tests with the rotor on were conducted according to three different procedures, depending on the information desired as noted subsequently.

Effect of Rotor Thrust on Body Aerodynamics

For these tests, body angle of attack was first set to a value of $\alpha = -2°$, which was selected because it was somewhat representative of a typical cruise attitude and because the rotor was easier to "fly" for a nose-down attitude. Rotor speed was brought up to 1862 rpm, and a modest amount of thrust was applied while the tunnel speed was increased to the desired condition. Once the tunnel speed was set, the collective pitch was varied over the range necessary to provide the desired thrust range. Data were taken at various increments, usually at every 20 lbf, from a low value near zero thrust up to the maximum capability of the drive motor, usually about 225 lbf.

Effect of Angle of Attack at Constant Rotor Thrust

For these tests, body angle of attack was set slightly negative, and the rotor speed and tunnel velocity were brought up to condition as in the preceding section. Once the desired condition was established, tunnel speed was held constant and the model was swept through an angle-of-attack range while using the real-time data display and model cyclic and collective pitch control to maintain constant rotor thrust and zero cyclic blade flapping. Following the completion of a run at one advance ratio, tunnel speed was changed to the next value, the rotor thrust was reset, and the next run was made. These were, in effect, rotor propulsive-force sweeps.

Angle-of-Attack Stability Sweeps

For these tests, the tunnel and rotor were brought up to speed as before. When the desired tunnel speed was reached, the model was trimmed by using collective pitch to set total lift to 190 lbf (with full-scale lift being 4300 lbf). Model angle of attack was then changed as necessary to trim the total drag to 0 (with $C_{D,T} = 0$) while maintaining total model lift at 190 lbf with zero cyclic blade flapping on the rotor. This was an iterative procedure that usually took three or four cycles to complete. Because there was no tail rotor, no attempt was made to trim yawing moment by using sideslip angle. After the trim condition was reached (with $C_{D,T} = 0$ and $L = 190$ lbf), the model was swept through an angle-of-attack range around the trim angle of attack without changing the rotor control settings. In this way, the static stability characteristics of the flight vehicle were simulated; this procedure was repeated

for advance ratios of 0.04, 0.10, 0.15, and 0.20, based on a rotor tip speed of 650 ft/sec.

Presentation of Results

The results of this investigation are presented in both dimensional and coefficient form. Where given, dimensional data for the model are presented as equivalent full-scale parameters of the form Force/q and Moment/q customarily used in the helicopter industry, and coefficient parameters are presented according to the definitions already given. Most of the data are given in coefficient form, but full-scale dimensional data can be obtained easily by means of the following conversion factors:

To obtain:	Multiply coefficient by:
Force/q, ft^2	777306.1/q
Moment/q, ft^3	12339524.7/q

Two sets of data are presented for each configuration. The first set, termed "model" data, includes all forces and moments due to the airframe, hub, rotor, and controls; and the second set, termed "airframe" data, consists of the forces and moments measured by the fuselage balance. The second set of data includes the interference effects of the hub, rotor, and MMS on the airframe, but it does not include the actual forces and moments due to the various rotor-related components. The data are presented in figures 7 to 33 as follows:

Results and Discussion

Rotor-Off Aerodynamic Characteristics

Longitudinal aerodynamic characteristics. The basic longitudinal aerodynamic characteristics of the aircraft with the rotor off are presented in figures 7 to 10. Data were presented for the fuselage alone and for the successive addition of tails, hub, and MMS so that the individual effects of each of these major components could be determined. As was noted previously, two balances were used in this investigation— one for the rotor, including hub and MMS when present, and one for the body, including all protuberances. The data of figure 7 are for the model forces and moments, whereas the data of figure 8 are for the airframe. The data of figure 8, therefore, include the basic aerodynamic characteristics of the body as well as any interference effect of the hub and MMS.

When referring to figure 7, it can be seen that the aircraft had negative lift over the entire range of α tested. The addition of the horizontal tail resulted in

a large negative lift increment as expected, and it was attended by an increase in drag which, though small, was measurable. The lift and pitching-moment data of figure 7 show that the horizontal-tail effectiveness was sharply reduced at about $\alpha = 0°$, and it was stalled at about $\alpha = -8°$ with the rotor hub and MMS removed. Addition of the hub caused a sharp stall of the tail at $\alpha = 0°$, and the MMS caused an even earlier stall at about $\alpha = 4°$, resulting in a longitudinal instability over an angle-of-attack range from 4° to −6°. The fact that the moment curve for the complete configuration is parallel to the body-alone curve over the range of α tested from 4° to −6° indicates that the horizontal tail was completely ineffective in providing stability in this range and was apparently being washed by the strong wake from the hub, pylon, and MMS.

The body-balance force and moment data of figure 8 provide some insight into the hub and sight wake effects on the horizontal tail. By referring to the moment data of figure 8, it can be seen that the addition of the hub resulted in a reduction in the pitching moment contributed by the tail for angles of attack less than about 4°. Since these are body data and do not include the hub forces, the observed reduction in positive pitching moment with the hub on is apparently the result of reduced dynamic pressure at the tail caused by the wake of the hub, and it is very much like the cases discussed in reference 3. The problem is made somewhat worse by the addition of the MMS, as can be seen from the lift data of figure 8. The pitching-moment data of figure 8 also indicate that once the tail is stalled, the aircraft had the same longitudinal instability as the tail-off configuration, but with a large nose-up moment applied. At angles of attack below about −6° to −8°, a measure of longitudinal stability had been restored. As a result of these wake interaction effects, the tail provided no contribution to longitudinal stability over an angle-of-attack range from −8° to 2°, although the presence of a nose-up moment indicates that the tail could provide some longitudinal control power if its angle of attack were varied.

A comparison of the pitching-moment data of figures 7 and 8 shows that the loss in the pitching moment of the tail due to the wake effects is approximately balanced by the nose-up moment of the hub and sight drag acting above the moment reference center. Thus, over the normal operating angle-of-attack range of approximately −10° to 10°, there would be little reason to expect a pitching-moment trim change to result from the addition of the MMS (particularly near $\alpha = 0°$), provided that the addition of a thrusting rotor did not change the aerodynamic characteristics of the basic airframe. In

view of the substantial interference effects of the hub and pushrods, there was some concern that the nonscale general-research hub might have been affecting the horizontal tail in a manner unlike the full-scale hub. A comparison of the swept volumes and general shape of the model hub used in the tests with the flight hardware showed, however, that the differences in the two configurations were extremely small. The swept volume of the model hub, pushrods, and rotating scissors was only 5 percent larger than that for the full-scale aircraft (147 in^3 vs 140 in^3) and should not be a significant factor. It is felt, therefore, that these data are representative of the prototype flight configuration.

The drag data of figures 7 and 8 are somewhat unusual in that they do not have the characteristic "bucket" shape normally seen but, instead, are fairly uniform at angles of attack above 0°. The body data of figure 8 are more conventional in nature, although for $\alpha > 4°$, the drag tended to decrease slightly with increasing α. The fact that neither the lift curve nor the pitching-moment curve is linear and that both curves actually have two inflection points indicates that a process of flow separation and reattachment was occurring over the upper and lower surfaces of the body as angle of attack was changed. In any event, the uncharacteristic drag data occur at angles of attack greater than 5°, which is generally outside the operational range for this aircraft. Below $\alpha = 5°$, the drag data are more typical in character and contain no real surprises.

The data of figure 7 indicate that both the hub and the MMS had significant drag, as was to be expected, and that the drag of the tails was a function of tail lift coefficient. The fact that the tail drag increment is gradually reduced for positive angles of attack indicates that there was attached flow over the tail and fairly low tail lift coefficients over the range of aircraft angle of attack above about 4°. The lower dynamic pressure over the tail at the higher angles of attack due to the wake effects already noted would also result in somewhat reduced drag at the tail. Note that the lift on the tail is nearly 0 in the lift data of figure 8 at an aircraft angle of attack of about 14° or so (e.g., the lift on the body alone is the same as the lift on the body and tail combination); it would therefore be reasonable to expect a gradually reduced tail drag component as the tail lift coefficient approached 0.

The interference drag of the hub and MMS are presented in figures 9 and 10, respectively. The data in figures 9(b) and 10(b) are the measured forces on the body due to the presence of the appropriate items, and thus indicate true interference components. At $\alpha = 0°$, the interference drag incre-

ment of the hub was about 19 percent of the total drag increment due to the hub. (Compare fig. 9 with fig. 7.) These increments are fairly uniform down to an angle of attack of about $-8°$, at which point the interference drag reduced quickly to near 0, and actually became slightly favorable at $\alpha \approx -12°$.

Figure 9(b) shows that the minimum full-scale drag D/q of the airframe without hub or MMS was 8.62 ft^2 at $\alpha = -2.4°$. The model hub and controls had an equivalent full-scale drag increment of 5.20 ft^2 (fig. 9). In the presence of the hub used for these tests, the minimum airframe drag increased from 8.62 to 9.26 ft^2 at $\alpha = -2.4°$ (fig. 9(b)). Adding the MMS caused an increase in interference drag that resulted in an airframe minimum drag of 9.42 ft^2 at $\alpha = -2.4°$, and the minimum drag of the airframe and MMS in the presence of the hub was 12.34 ft^2 at $\alpha = -2.4°$, exclusive of the hub.

Lateral-directional aerodynamic characteristics. The basic lateral-directional aerodynamic characteristics of the model at $\alpha = 0°$ with the rotor off are presented in figures 11 and 12. Data are presented for the fuselage with and without tails, hub, and MMS so that the individual effects of each of these major components may be assessed. The data of figure 11 present the total forces and moments of the complete configuration, whereas figure 12 presents force and moment data for the airframe.

The data of figure 11 indicate that the basic fuselage without tails was directionally unstable, as was to be expected, and that it had a modest positive dihedral effect $(\partial C_l / \partial \beta < 0)$. Adding the horizontal and vertical tails to the basic fuselage resulted in somewhat erratic directional characteristics. At sideslip angles greater than $\beta = 5°$, the model had high directional stability. Between $\beta = 5°$ and $-15°$, the model had very low or neutral directional stability and was unstable for angles of sideslip beyond $-15°$. The apparent cause for this behavior is that the vertical tail was stalled for sideslip angles below about 5°. As was the case for the longitudinal stability characteristics, the addition of the hub and MMS caused a slightly earlier tail stall than in the case with the hub off. Note in figure 11(a), however, that with either the hub alone or the hub and MMS installed, there was a significant increase in the directional stability at angles of sideslip between $-5°$ and $-15°$. Figure 12(a) shows that the airframe was directionally unstable in the range of sideslip angles from $-5°$ to 5°, suggesting that the vertical tail too was immersed in the wake from the hub and MMS. The positive dihedral effect was progressively improved by the addition of the hub and MMS. These directional stability characteristics are consistent with the observa-

tion reported in reference 3 in which the hub and pylon wakes were responsible for serious degradation of both the longitudinal and directional characteristics.

The effect of angle of attack on the lateral-directional characteristics is shown in figures 13 and 14 in which the lateral and directional components versus sideslip are presented for $\alpha = 0°$, 6°, and $-6°$. For the MMS off, increasing the angle of attack led to greater directional instability over a sideslip range from about $-5°$ to 5° and to an increase in dihedral effect, whereas decreasing the angle of attack caused an increase in directional stability over a sideslip range from about $-5°$ to 5° and to a decrease in dehedral effect. The same general characteristics may be seen in the data of figure 14 for the configuration with the MMS installed.

Rotor-On Longitudinal Aerodynamic Characteristics

Effects of thrust. The basic longitudinal aerodynamic characteristics of the helicopter as a function of thrust coefficient are presented in figures 15 and 16 for a range of advance ratios. Data are presented both for the complete configuration, which includes rotor forces and moments, and for the airframe alone, which includes the effect of the thrusting rotors on the airframe, but excludes all rotor components, including the hub and MMS when appropriate.

The data of figures 15 and 16 were all obtained for an angle of attack of $-1.2°$. The total force data of figure 15, which show the expected increase in total lift and propulsive force with increasing thrust coefficient, are nearly linear, as would be expected. The pitching-moment data are somewhat erratic and generally show little effect on pitching moment as power was increased. At the lowest advance ratio of 0.04, the data show an increase in $C_{m,T}$ from 0.00012 to 0.00023 over the range of thrust coefficients as the wake swept over the tail. At $\mu = 0.10$, there was a sharp increase in $C_{m,T}$ as thrust was increased up to about $C_T = 0.003$, after which the pitching-moment increment was more uniform. This result is not too surprising when the performance of the horizontal tail with the rotor off is recalled (see fig. 8) and the impact of the wake skew angle is considered. Figure 17 is a plot of the undeformed wake skew angle χ at the hub as a function of C_T where χ has been computed by means of the following equations, taken from reference 4. The wake skew angle is given by

$$\chi = \tan^{-1}\frac{\mu}{\lambda}$$

where

$$\mu = \frac{V_\infty}{\Omega R}$$

$$\lambda = \frac{V_\infty \sin \alpha + w_o}{\Omega R}$$

The rotor inflow velocity is given by

$$w_o = \sqrt{\frac{T}{2\rho\pi R^2}}$$

If the path of the undeformed wake is traced on a scaled drawing of the aircraft aligned at $-1.2°$ to the free-stream flow, it is evident that the wake from the rotating hub and controls lies very close to the horizontal tail for the full range of thrust coefficients at $\mu = 0.15$; this would be true even for the more realistic case of a distorted wake axis. For advance ratios less than 0.15, the horizontal tail was swept by the more outboard portions of the rotor wake that have a higher velocity. From referring to figure 15, it can be seen that the model pitching moment was fairly constant with increasing thrust coefficient for advance ratios above 0.15; whereas for advance ratios below 0.15, there was a relatively larger effect on pitching moment as power was increased. Figure 16 shows that the airframe pitching moment was a strong function of C_T at lower advance ratios, whereas for advance ratios of 0.20 and 0.22 there was a more moderate influence of power on the moment increment.

The longitudinal aerodynamic characteristics shown in figures 15 and 16 illustrate the powerful influence that the rotor wake exerts on the airframe aerodynamics. At the lowest advance ratio, it is evident that both direct thrust and induced aerodynamic components contribute to the change in airframe aeodynamic characteristics with changes in thrust; but at the higher advance ratios, the relative influence of direct effects versus induced effects is not very clear, particularly for lift and pitching moment. The incremental nature of the data of figures 15(b) and 16(b), for the model and airframe drag, respectively, indicates that it may be possible to "collapse" the curves for different advance ratios onto a single curve independent of μ by using a suitable normalizing parameter that could account for variations in both thrust and forward speed. If such a parameter were identified, it may then be possible to account accurately for interference drag when attempting to use rotor-off model data to predict complete-configuration aerodynamic characteristics, at least insofar as propulsive force requirements were concerned. References 5 and 6 suggest that plotting body lift/thrust (L/T) and drag/thrust (D/T) against a thrust parameter, which is defined as the ratio of free-stream dynamic pressure to rotor disk loading $(q/(T/A))$, would cause the body

lift and drag characteristics to collapse onto a single line. This operation was performed for the thrust-dependent data of figures 15 and 16, and the results are shown in figure 18.

It is immediately apparent from figure 18 that the suggested normalizing parameter $q/(T/A)$ was effective in normalizing the data at the higher advance ratios, but it was less effective at the lower advance ratios, particularly for the lift data. The drag data collapse nicely onto a single line for most of the speed range tested except for those at $\mu = 0.04$, and the data for $\mu = 0.10$ are somewhat less out of line. These data are in general agreement with the conclusions of references 6 and 7; but unfortunately the data reveal little about the interference effects between the body and rotor, other than to illustrate the fact that the body lift and drag components are strong functions of rotor thrust. Having independent measurements of airframe and rotor forces, however, made it possible to calculate the interference drag due to the addition of the thrusting rotor by merely subtracting rotor-off data from rotor-on data. By dividing the resultant increment by the rotor-on airframe data, the interference components are conveniently expressed as a percentage of the measured rotor-on components and should reflect more accurately the effect of the rotor on the basic aerodynamic characteristics.

The results of conducting this operation on the data of figures 15 and 16 are shown in figure 19 for the lift and drag components and exhibit the same trends as the data of figure 18, although in a different form. At lower advance ratios, the interference effects of rotor thrust were strong, nonlinear functions of the relative momentum in the rotor wake, particularly for smaller values of $q/(T/A)$ that corresponded to the higher thrust conditions. The interference lift component was considerably more sensitive to local flow-field conditions than was the drag, as might be expected, and not until the advance ratios were 0.20 and 0.22 could the curve for $\Delta L/L$ be legitimately regarded as having been normalized sufficiently to consider it as a single trend curve. For $\mu > 0.15$, the interference lift ranged from about 10 to 16 percent of the total measured lift, and the mean value tended to be about 14 percent.

The drag data, on the other hand, were somewhat better behaved, tended to collapse more quickly to a relatively stable value for advance ratios greater than 0.10, and exhibited less general scatter at the two lowest advance ratios than did the lift. The interference drag increment, once established, ranged from 4 to 6.5 percent, with the greater part of the data tending to cluster around approximately 6 percent over a range of $q/(T/A)$ from about 3.0 upwards. In

9

considering the disparity in the data at lower values of the thrust parameter $(q/(T/A))$ at lower advance ratios, there does not seem to be any immediately obvious reason that the interference components should not be the same for any given value of the thrust parameter, irrespective of advance ratio, particularly since that is the case at higher advance ratios. It is therefore reasonable to consider the behavior of the aerodynamic components themselves as functions of advance ratio or, more precisely, forward speed, since rotor speed is essentially constant.

Figure 20 is a plot of the lift and drag characteristics (expressed as full-scale L/q and D/q, respectively) of the airframe with the rotor removed as function of free-stream dynamic pressure. These data, obtained early in the test program, were used to establish the lower boundary of tunnel speed at which reliable rotor-off data could be obtained and are useful here in providing some explanations for the data spread of figures 18 and 19. The darkened triangles on the abscissa of figure 20 identify the dynamic pressures for the range of advance ratios covered in the investigation. Presented in this way, the lift and drag data reflect the influence of Reynolds number. As can be seen, data taken at the two lowest advance ratios were considerably affected by Reynolds number. For example, the drag obtained at $q = 0.8$ lb/ft^2, which correspond to $\mu = 0.04$, was 8.2 percent higher than the drag taken at $q = 20.1$ lb/ft^2, which corresponded to $\mu = 0.20$. On the other hand, the download measured at $q = 0.8$ lb/ft^2, was 180 percent greater in magnitude than that measured at $q = 20.1$ lb/ft^2.

Although the data of figure 20 do not allow a quantitative evaluation of the trends in figures 18 and 19, they do provide a qualitative explanation. The spread in the measured interference components shown in figures 18 and 19 is almost certainly due in large part to Reynolds number effects. For example, for the case when $\mu = 0.04$, the Reynolds number based on the estimated velocity in the rotor wake (in which the body is almost completely submerged) varies from about 1.9×10^5 to 3.0×10^5 per foot over the thrust range tested. This range of Reynolds number for the rotor-on tests is about the same as would be encountered during rotor-off testing at free-stream dynamic pressures from 1.14 to 2.50 lb/ft^2, and it is clear that there are significant Reynolds number effects at these low dynamic pressures. It should be noted here that these types of Reynolds number effects are not confined to model tests only. The full-scale helicopter will also encounter Reynolds number effects through the transition speed range, but they should be far less severe than those encountered at model scale, and it is reasonable to expect the inter-

ference data for the rotor-on case to collapse more quickly to a fairly uniform increment.

Effect of angle of attack. The longitudinal aerodynamic characteristics as a function of angle of attack are presented for the basic AHIP configuration without the MMS in figures 21 to 26. The lift and drag characteristics were essentially what would be expected: the lift-curve slope for the complete configuration was positive, and the overall lift was almost entirely a function of the rotor properties. The pitching-moment data of figure 21 show the model to have been unstable with angle of attack for all advance ratios tested. Although the data of figure 22 show that the tail did provide some stability at low advance ratios, it was unable to overcome the instability of the rotor, as can be seen in figure 21. Note in the pitching-moment data for $\mu = 0.10$ in figure 22 that the airframe alone had a stable slope for $\alpha < 2°$. At $\mu = 0.15$, the stability of the body/tail combination was reduced somewhat; and at $\mu = 0.20$, the pitching-moment data were much like the rotor-off data, except with a moment increment applied. By referring to the complete-configuration data for $\mu = 0.10$ in figure 21, it can be seen that the model had approximately neutral stability over the angle-of-attack range from 2° to 7°; whereas for all other conditions with the rotor on, the model had a substantial degree of longitudinal instability. These data suggest that the wake from the pylon, hub, and pushrods was blown away from the tail for nose-up attitudes at low advance ratio, with the result that the tail was operating in relatively smooth conditions. At higher speeds, the wake skew angle was apparently sufficiently high for the tail to be immersed in the wake of the pylon, hub, and pushrods, as was the case with the rotor off. Some additional insight into this phenomenon can be gained from figures 23 and 24.

Figure 23 presents the lift and pitching-moment characteristics of the model as a function of angle of attack for tail-on and tail-off conditions at four advance ratios, and figure 24 presents the same data for the airframe. The lift data of figure 23 were straightforward and were generally as expected. Unfortunately, there was an error in setting model conditions for the tail-off data of figure 23(d), with the result that tail-on lift is shown to be greater than tail-off lift. The main feature to be noted in the lift data of figure 23 is that the lift-curve slope is largely unaffected by the tail. The pitching-moment data of figure 23(a) show that the configuration was slightly unstable at $\mu = 0.04$, both with tail on and tail off. The addition of the tail had little effect on stability, but it resulted in nose-up moment. The data of

figure 23(b) for $\mu = 0.10$ indicate that adding the tail actually resulted in not only a slight reduction in stability $((\partial C_m/\partial\alpha)_{\text{tail on}} > (\partial C_m/\partial\alpha)_{\text{tail off}})$ but also a more nose-down increment in C_m over a range of α from about $-2°$ to $2°$. The reason for this apparently contradictory contribution of the tail is not clear from the available data. Figures 23(c) and 23(d) indicate that at the higher advance ratios, the model was longitudinally unstable over the entire range of α tested, although the tail did provide a small measure of stability, as can be seen by the slightly reduced positive slopes for the pitching-moment curves with the tail on.

The pitching-moment data of figure 24 give an indication of the a rodynamic characteristics of the tail in the presence of the rotor. At $\mu = 0.04$, there was a strong nose-up increment in pitching moment, but very little effect on stability. This is not too surprising in view of the fact that the downwash angle at the tail at $\alpha = 0°$ was about $55°$, based on undistorted skew-angle calculations, and the tail was undoubtedly stalled. The data of figure 24(b) for $\mu = 0.10$, however, show markedly different characteristics. Below $\alpha = 2°$, the tail was stalled and the airframe had neutral stability. For angles of attack greater than $2°$, however, the airframe had a significant measure of stability, indicating well-attached flow over the horizontal tail. Note that the stability of the airframe with the tail off was neutral and that the pitching moment was slightly negative.

A comparison of the rotor-off and rotor-on data in figure 24(b) illustrates the expected alteration in the basic flow field around the helicopter caused by the rotor. At $\mu = 0.04$, the aerodynamic characteristics were completely dominated by the rotor; and and as the advance ratio was increased from 0.10 to 0.15, there was a progressive loss in stability of the airframe with the tail on so that at $\mu = 0.20$, the stability was neutral. At $\mu = 0.15$, the airframe stability with the rotor on was the same as that with the rotor off at positive angles of attack, both in terms of slope and magnitude. At $\mu = 0.20$, the airframe was neutrally stable with the rotor on, and the rotor induced a nose-up moment. Note that the rotor increment was wholly an interference effect, since the rotor components themselves are not included in the data of figure 24. These results suggest that rotor-off wind-tunnel data should be used with caution when attempting to predict the longitudinal stability characteristics of complete configurations. In fact, low-speed stability characteristics in the speed range through transition and up to about $\mu = 0.15$ or so will almost certainly be in error unless the viscous effects of the skewed rotor wake, including wake-induced stall effects, are included analytically in experimental data obtained without a rotor.[1]

Drag characteristics are presented in figure 25 for the model and in figure 26 for the airframe alone. The data of figure 25 show the drag characteristics of the model to be almost wholly dominated by the rotor, as would generally be expected. What is not evident in figure 25 is the extent to which the rotor wake influenced the body drag development; these data are provided in figures 26 and 27. The data show that the rotor had a substantial effect on drag characteristics that was similar to the results noted in reference 7, in which an interference drag component of about 10 percent was reported. Figure 26(a) shows the drag for the tail-on and tail-off configurations at $\mu = 0.04$, along with the tail-on drag for the rotor off, and it also shows that the rotor-on drag was much lower than the rotor-off drag. This reduction in airframe drag is due primarily to the powerful effect of the skewed rotor wake in causing a substantial realignment of the body normal and axial-force vectors, and it may also be the result of reduced separation over the upper surface of the model. The fact that the drag increment due to the tail is approximately a linear function of α is a further indication that the tail was fully stalled for this advance ratio. As the forward speed was increased, the drag increment due to rotor interference effects was reduced, as would be expected, until the airframe drag at $\mu = 0.20$ was nearly the same with rotor on as with rotor off. In addition, however, the drag increment began to vary nonlinearly with α until the shape of the tail-on and tail-off curves at $\mu = 0.20$ was very much like that for the rotor off. (Compare fig. 26 with 8(b).)

Effect of mast-mounted sight. The longitudinal characteristics of the aircraft with the MMS installed are presented in figure 28 for the model and in figure 29 for the airframe alone. The overall characteristics of the model are generally similar to those shown in figure 21 for the MMS-off case. The lift-curve slopes were nearly identical for the two conditions, but the pitching-moment data showed that the configuration with the MMS on was slightly more unstable than with the MMS off. The drag data were

---

[1] The present investigation was conducted as an independent research activity of the U.S. Army Structures Laboratory (USAAVSCOM) and was not a part of the development program. During flight testing of the prototype configuration, the AHIP contractor encountered significant vibrations and directional stability problems that were found to be caused by the wake from the engine cowling. Major modifications to the cowling were subsequently designed and tested in flight, and the current configuration of the AHIP has demonstrated satisfactory handling qualities.

fairly straightforward and were generally as expected in that there was a more-or-less uniform drag increment because of the MMS. The angles of attack at which propulsive trim occurred were somewhat more nose down with the MMS on, as was expected, and can be seen in figure 30, which was obtained from the data of figures 18(b) and 28(b). At $\mu = 0.15$ and 0.20, an additional nose-down attitude of about 2° was required for the total drag to be 0; whereas at $\mu = 0.10$, an additional nose-down pitch attitude of about 1° was required.

These increments in nose-down pitch attitudes may be used to estimate the rotor-on drag of the MMS by computing the increment in propulsive force required of the rotor between the MMS-off and MMS-on configurations at equal values of total configuration lift for zero net drag. Calculations conducted in this way then include both the basic and interference drag components of the MMS. By comparing the values obtained by these calculations with the rotor-off measurements shown in figure 7(b), the total interference drag component due to the MMS may be estimated. When these calculations were performed, the full-scale D/q values presented in table II were obtained. As can be seen from table II, there was substantial interference drag with the rotor on. No doubt a portion of the indicated interference drag was due to Reynolds number, since the Reynolds number is 4.15×10^5 per foot for $\mu = 0.10$ and 8.3×10^5 per foot for $\mu = 0.20$. An additional increment included in these data is the airframe drag caused by the change in angle of attack; this increment can be accounted for by using the data of figure 29(b) and calculating $\Delta(D/q)$ for the airframe due to the nose-down increment in α. The results of these calculations are presented in table III. One further interference drag component present in table II is the almost-uniform full-scale D/q increment of 0.158 on the airframe caused by the addition of the MMS, as shown in figure 8. When this increment and the increments of table III are subtracted from the $\Delta(D/q)$ data of table II, the full-scale values for $\Delta(D/q)$ due to the installation of the MMS (see table IV) are obtained. Clearly, there remains a substantial component of interference drag on the aircraft because of the installation of the MMS.

Both the preceding evaluation of the various measured total drag components and the airframe drag data of figure 31 indicate that the major portion of this interference is related not to the airframe but to an alteration in the rotor drag characteristics. Ideally, a third balance, or strain-gauge mounting, between the MMS and rotating hub would have permitted a direct measurement of the MMS drag and an evaluation of the MMS-induced rotor loads. Unfortu-

TABLE II. DRAG INCREMENT DUE TO THE MMS

| μ | α, deg, for $C_{D,T} = 0$ and $L = 4300$ lbf with— | | $\Delta\left(\dfrac{D}{q}\right)$, ft^2 (full scale) |
	MMS off	MMS on	
Rotor off			3.40
0.10	4.26	3.15	16.45
.15	2.50	.60	12.69
.20	.50	−1.65	8.50

TABLE III. CORRECTION TO DRAG DUE TO ANGLE OF ATTACK

μ	$\Delta\alpha$, deg, for $C_{D,T} = 0$	$\Delta\left(\dfrac{D}{q}\right)_{\text{airframe}}$, ft^2
Rotor off		
0.10	−1.11	1.10
.15	−1.90	.07
.20	−2.15	.16

TABLE IV. TOTAL DRAG DUE TO THE MMS

μ	$\Delta\left(\dfrac{D}{q}\right)$, ft^2
Rotor off	3.24
0.10	15.19
.15	12.46
.20	8.18

nately, it was not possible to provide that capability within the constraints imposed by this preliminary investigation. Some understanding of the MMS impact on rotor performance can be inferred however from the data shown in figure 32, in which the pitching moment of the rotor with and without the sight is plotted against angle of attack.

The data of figure 32 show that there was an increase in nose-up pitching moment on the rotor arising from the installation of the MMS. This result was to be expected, in view of the additional drag of the sight, but the increment in pitching moment cannot be accounted for wholly on the basis of sight drag alone. This can be seen by the dashed-line curve in figure 32, which represents the pitching moment due to MMS drag having been used to compute a moment increment that was then added to the sight-off data. The drag used for the dashed-line curve was obtained by multiplying the D/q values listed in table IV by the appropriate q at the advance ratio of

interest, and then by applying all the resulting drag at the center of the MMS. The resulting pitching-moment increment was then added uniformly along the sight-off data curve.

It is recognized that this procedure ignores the changes in interference drag due to angle-of-attack variations and the local increase in dynamic pressure at the sight location due to rotor-induced velocity, but the resulting curve is nevertheless of value in evaluating the gross effect of the sight on the performance of the rotor. The large additional increment in pitching moment at the lower advance ratios appears to be due to the sight wake being entrained in the rear portion of the rotor disk plane, resulting in an alteration in the fundamental lift distribution around the rotor disk. This hypothesis was confirmed qualitatively during the course of some informal smoke-flow studies conducted during the investigation, when the wake from the hub was observed to be entering the aft portion of the rotor disk for all advance ratios tested. Unfortunately, the smoke used for the observations was not sufficiently dense for photographic records to be made at advance ratios greater than about 0.08, but the following sketches illustrate the general nature of the flow that was observed during the tests:

$\mu = 0.10$

$\mu = 0.20$
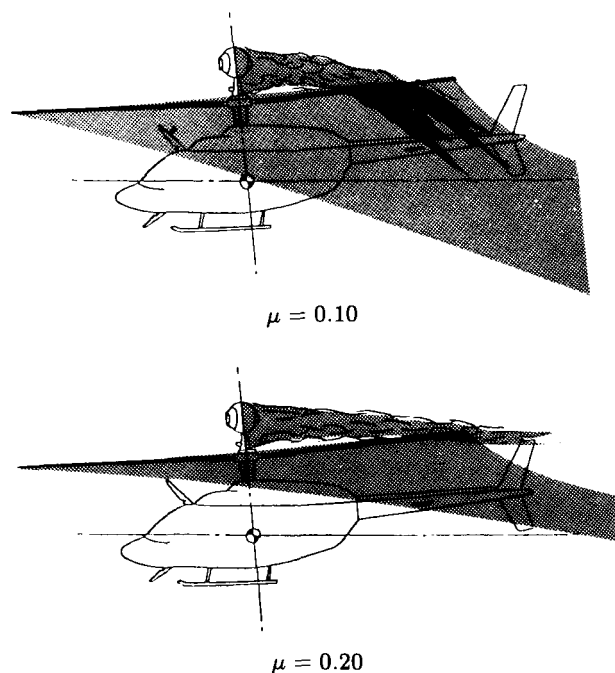
Note in figure 32(b) that the pitching-moment increment not accounted for by hub drag at $\mu = 0.20$ is much less than that at $\mu = 0.10$. This indicates that the sight wake was blown farther back on the rotor at the higher speeds so as to affect less of the rotor disk. These data suggest that considerable care must be exercised when attempting to estimate the net effect

on performance of any device—such as the MMS—which may reasonably be expected to alter the rotor inflow characteristics. As shown by the data in figures 29 to 32, interference effects can cause major changes in the fundamental aerodynamic characteristics of the rotor and airframe, and these effects are not readily subject to evaluation by analysis.

The overall effect of the MMS on the pitching-moment characteristics of the aircraft is summarized in figure 33 for both the complete configuration and the airframe alone. At $\mu = 0.04$, the data of figure 33(a) show that there was little effect of the MMS on the complete configuration. There was less nose-up airframe moment with the sight on, indicating that the dynamic pressure deficit at the tail, which was observed in the rotor-off tests (see fig. 8(a)), persisted when the rotor was installed. At $\mu = 0.10$, the aircraft was longitudinally unstable with the sight on, and the small region of neutral stability noted for the sight-off configuration was not present with the sight on. The airframe-alone data of figure 33(b) show that the airframe was stable for $\alpha > 3.5°$, but the presence of the sight wake caused the tail to stall earlier than with the sight off, with an attendant moment loss. The pitching-moment curve for the complete configuration showed a reduction in longitudinal instability for $\alpha > 3.5°$, as would be anticipated from the airframe-alone data. The same general trends were observed for the two higher advance ratios (0.15 and 0.20) as for the low-speed cases. That is, the installation of the sight resulted in somewhat more angle-of-attack instability and induced a nose-up moment on the complete configuration. The nose-up moment was caused by the combined effects of the drag of the sight acting above the aircraft center of gravity and the effect of the MMS wake altering the lift distribution over the rear portions of the rotor disk, as was noted previously. As an overall observation, it is worth noting that the aerodynamic characteristics of the rotor were sufficiently powerful to dominate almost completely the aircraft characteristics; and because of this, the pitching-moment trends measured for the model with the rotor off were not generally representative of the rotor-on characteristics. Interference effects of the rotor on the pitching-moment characteristics can be seen by noting the location of the rotor-off curves with respect to the rotor-on curves in the airframe-alone plots in figure 33.

Summary of Results

A wind-tunnel investigation was conducted on a 21-percent-scale powered model of the Army Helicopter Improvement Progam (AHIP) helicopter equipped with a mast-mounted sight (MMS). The model used a general-research rotor hub and blades

13

and was tested with and without the rotor. Rotor-off data were obtained with the hub rotating at normal rotor speed. Data were obtained over a range of thrust coefficients, advance ratios, angles of attack, and angles of sideslip. The major results of the investigation are summarized as follows:

Rotor-Off Characteristics

1. The basic aircraft had negative lift over an angle-of-attack range from $-15°$ to $15°$.

2. The airframe had positive longitudinal stability for an angle of attack greater than $5°$, but it was generally unstable for angles of attack between $-10°$ and $5°$. This instability was due to the tail being immersed in the wake of the pylon, hub, and mast-mounted sight (MMS).

3. The addition of the MMS reduced the horizontal-tail effectiveness.

4. The mast-mounted-sight drag was about 3.2 ft^2.

5. The airframe had high directional stability for angles of sideslip greater than $5°$, neutral or low directional stability for angles of sideslip from $-5°$ to $5°$, and high directional stability for angles of sideslip from $-5°$ to $-15°$. The vertical tail was stalled for sideslip angles beyond $-15°$, and the aircraft was directionally unstable for that condition.

6. The airframe had a modest positive dihedral effect for the entire range of sideslip angles tested.

7. The mast-mounted sight had a small detrimental effect on directional stability and a small favorable effect on dihedral effect.

Rotor-On Characteristics

1. The longitudinal aerodynamic lift and moment characteristics of the model were almost entirely dominated by the main rotor.

2. The model was unstable with angle of attack for all advance ratios tested. This was due to the natural instability of the rotor combined with the longitudinal instability of the airframe.

3. The mast-mounted sight caused both a small irregular effect on the longitudinal angle-of-attack instability and a nose-up pitching moment, which

was partly a result of the MMS drag acting above the aircraft moment reference center and partly a result of the wake from the sight altering the rotor inflow.

4. Interference effects due to MMS wake entrainment by the main rotor increased the effective MMS drag from a rotor-off value of 3.2 ft^2 to a rotor-on value of as much as 15.2 ft^2.

5. The strong rotor-body interactions observed in the present investigation suggest that rotor-off body data should be used with caution in attempting to predict stability and control characteristics of complete configurations.

References

1. Asselin, Leo J., Jr.; and Williamson, Donald R.: The Army's Improved Scout Helicopter. *Army R, D & A*, vol. 23, no. 1, Jan. Feb. 1982, pp. 33 35.

2. Heyson, Harry H.: *Rapid Estimation of Wind-Tunnel Corrections With Application to Wind-Tunnel and Model Design.* NASA TN D-6416, 1971.

3. Roesch, Philippe; and Vuillet, Alain: New Designs for Improved Aerodynamic Stability on Recent Aerospatiale Helicopters. *Vertica*, vol. 6, no. 3, 1982, pp. 145 164.

4. Pope, Alan; and Harper, John J.: *Low-Speed Wind Tunnel Testing.* John Wiley & Sons, Inc., c.1966., p. 446.

5. Betzina, Mark D.; Smith, Charles A.; and Shinoda, Patrick: *Rotor/Body Aerodynamic Interactions.* NASA TM-85844, USAAVRADCOM TR-83-A-12, 1983.

6. Smith, Charles A.; and Betzina, Mark D.: A Study of the Aerodynamic Interaction Between a Main Rotor and a Fuselage. *Proceedings of the 39th Annual Forum*, American Helicopter Soc., Inc., 1984, pp. 690 702.

7. Fradenburgh, Evan A.: Aerodynamic Design of the Sikorsky S-76 Helicopter. Preprint No. 78-06, *34th Annual National Forum*, American Helicopter Soc., Inc., May 1978.
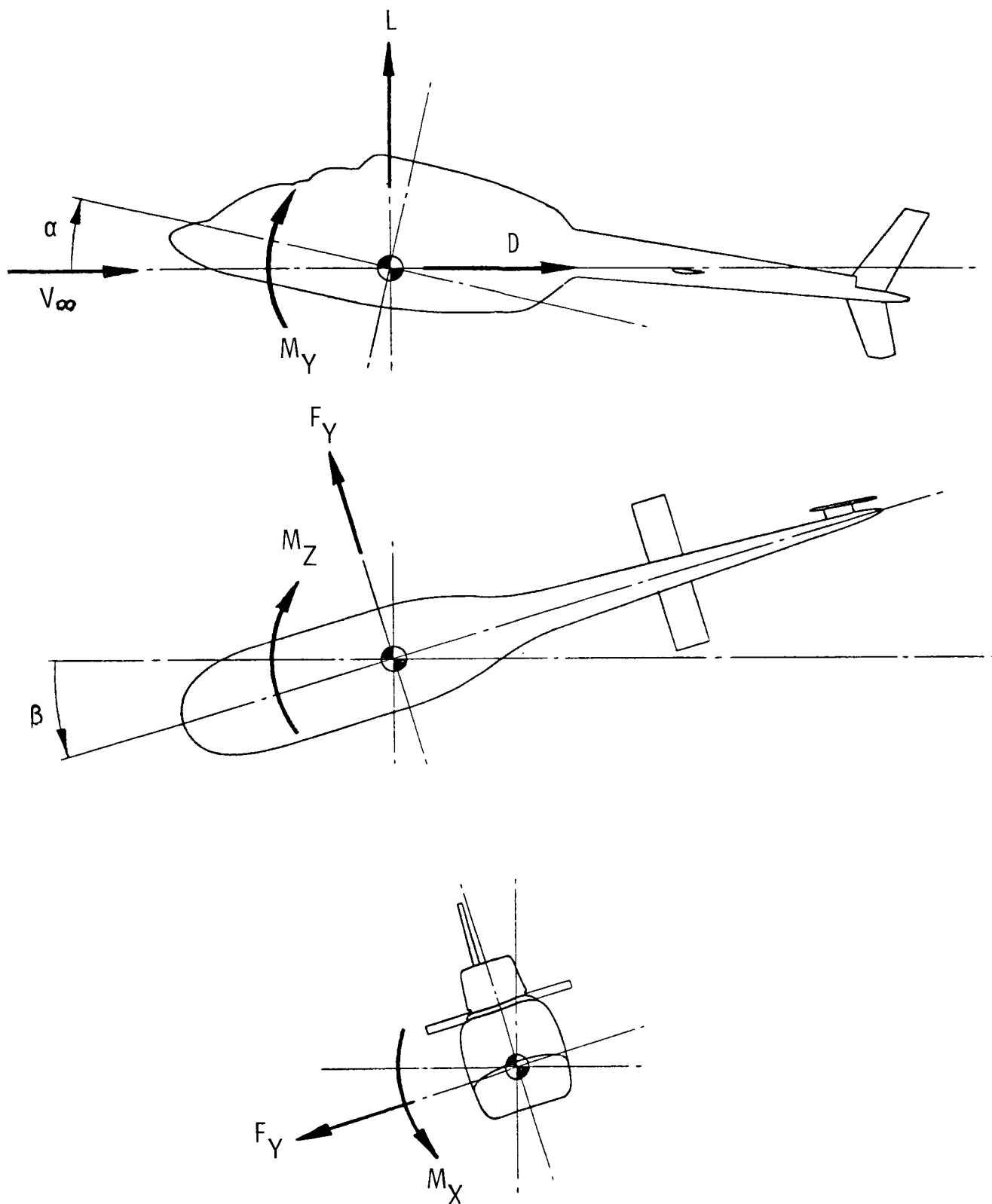
Figure 1. Axis system used in presentation of data. Arrows denote positive directions of forces, moments, and angular displacements.

16.45

3.85

80.00

5°

Moment reference center

78.19

23.80

16.25

5.50

10.95

21.45
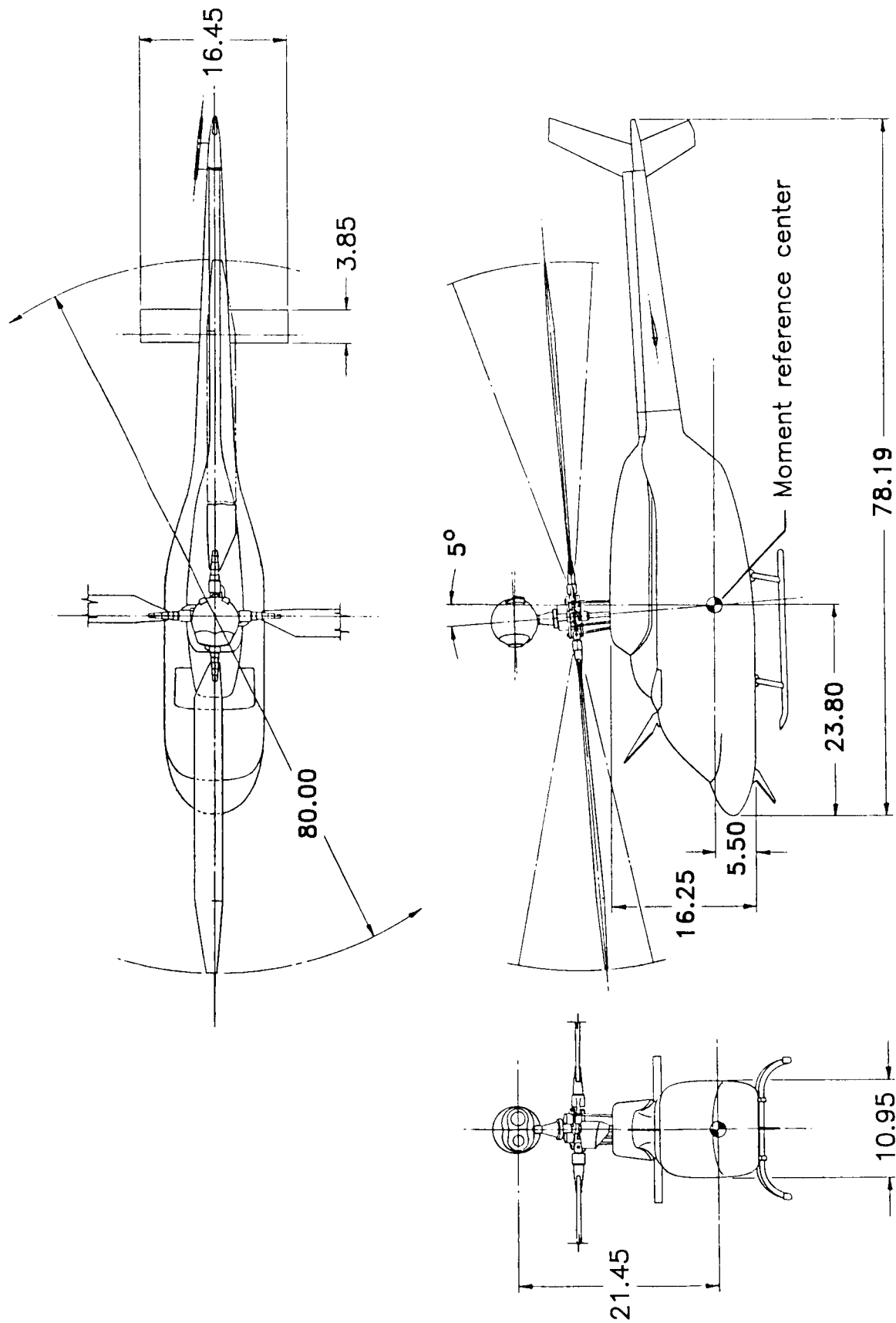
Figure 2. General arrangement of model used in investigation. Dimensions are given in inches unless otherwise specified.
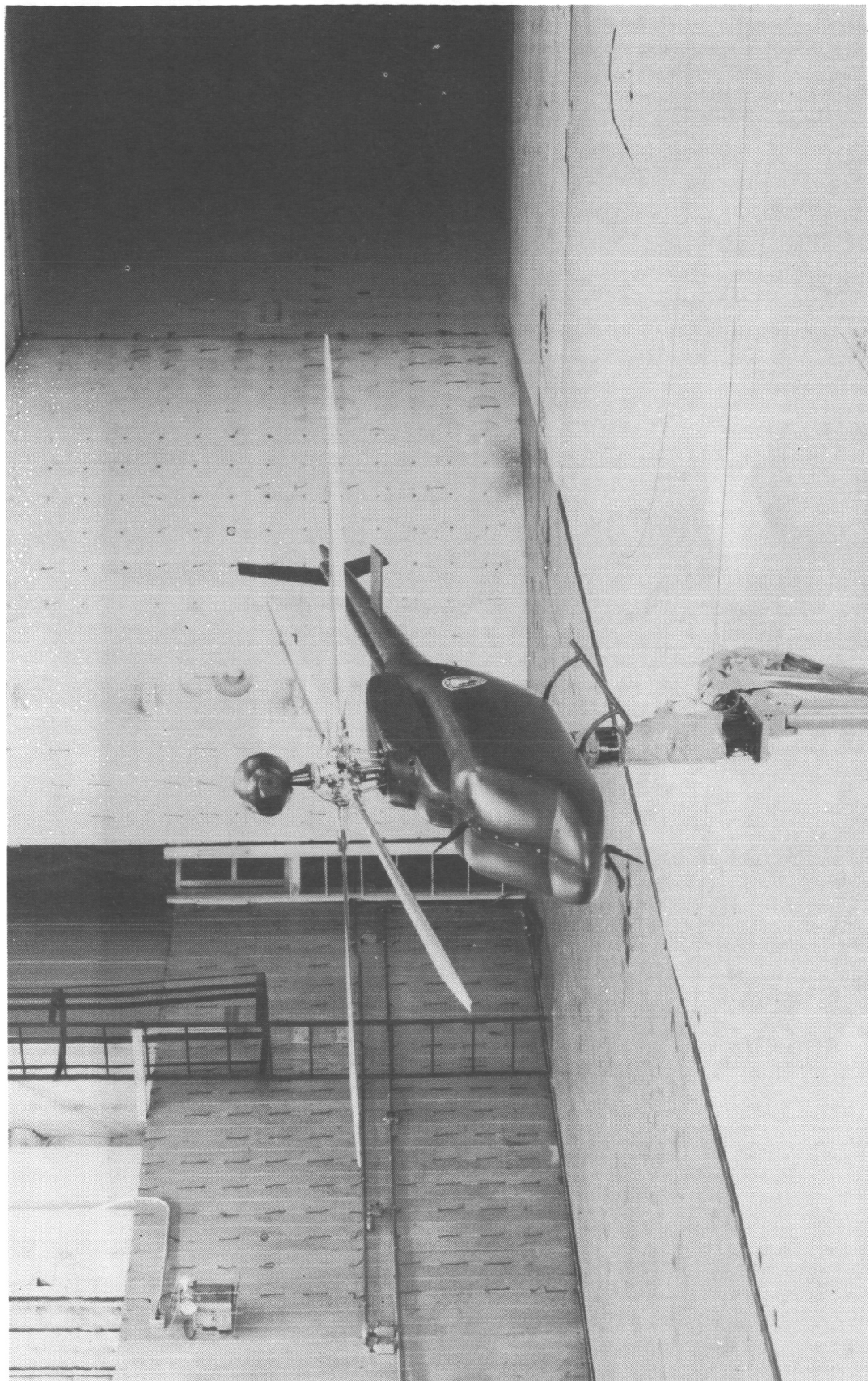
Figure 3. Photograph of model mounted for testing in the open-jet test section of the Langley 4- by 7-Meter Tunnel.

17

Control system

29-hp electric motor

Fuselage balance

Transmission

Rotor balance
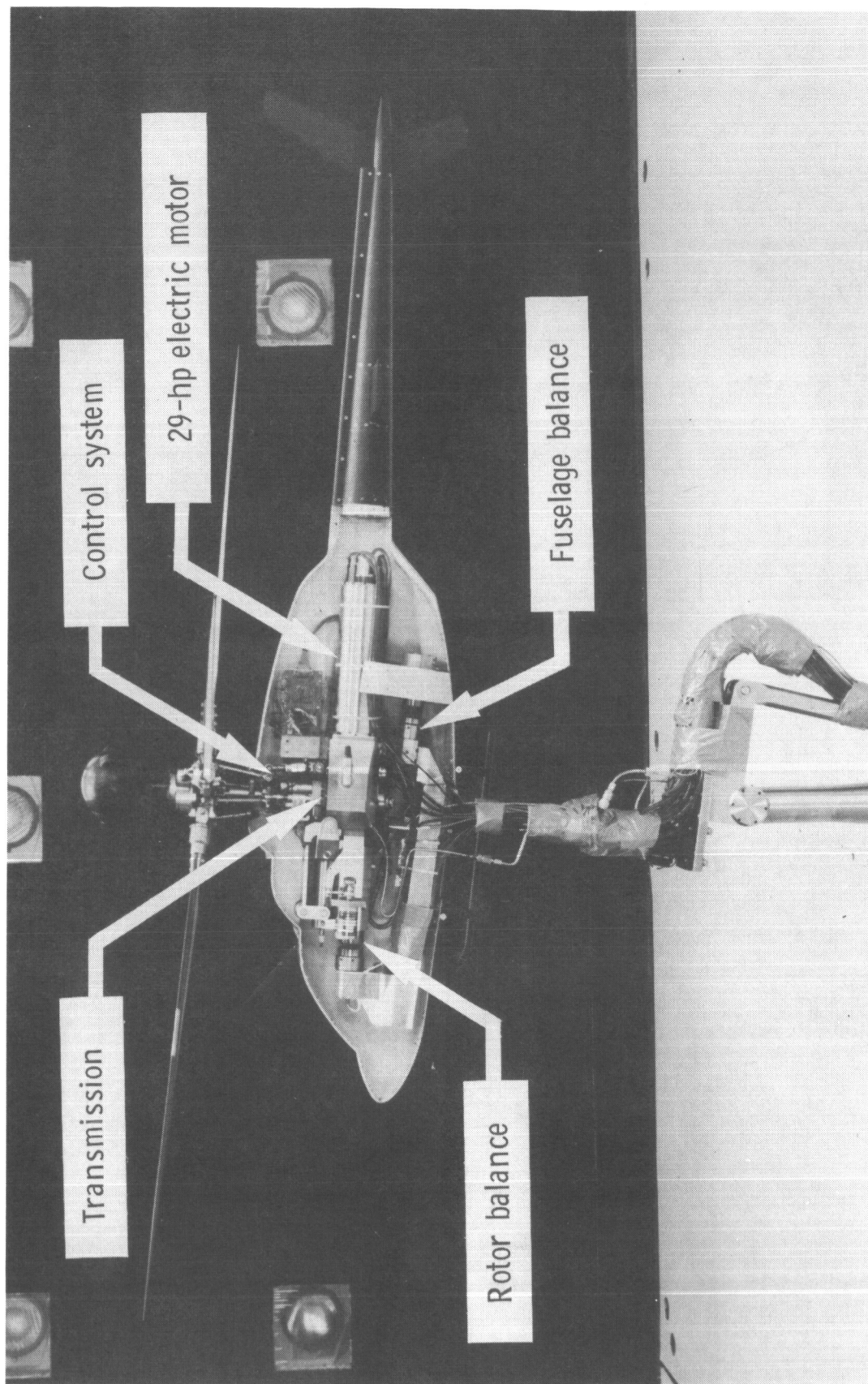
L-84-306

Figure 4. Left-fuselage half removed to show internal arrangement of rotor drive system.

18

Graphite/epoxy spar

Polyurethane foam cores

Fiberglass/epoxy external skin

Tungsten leading-edge balance weight

3.14
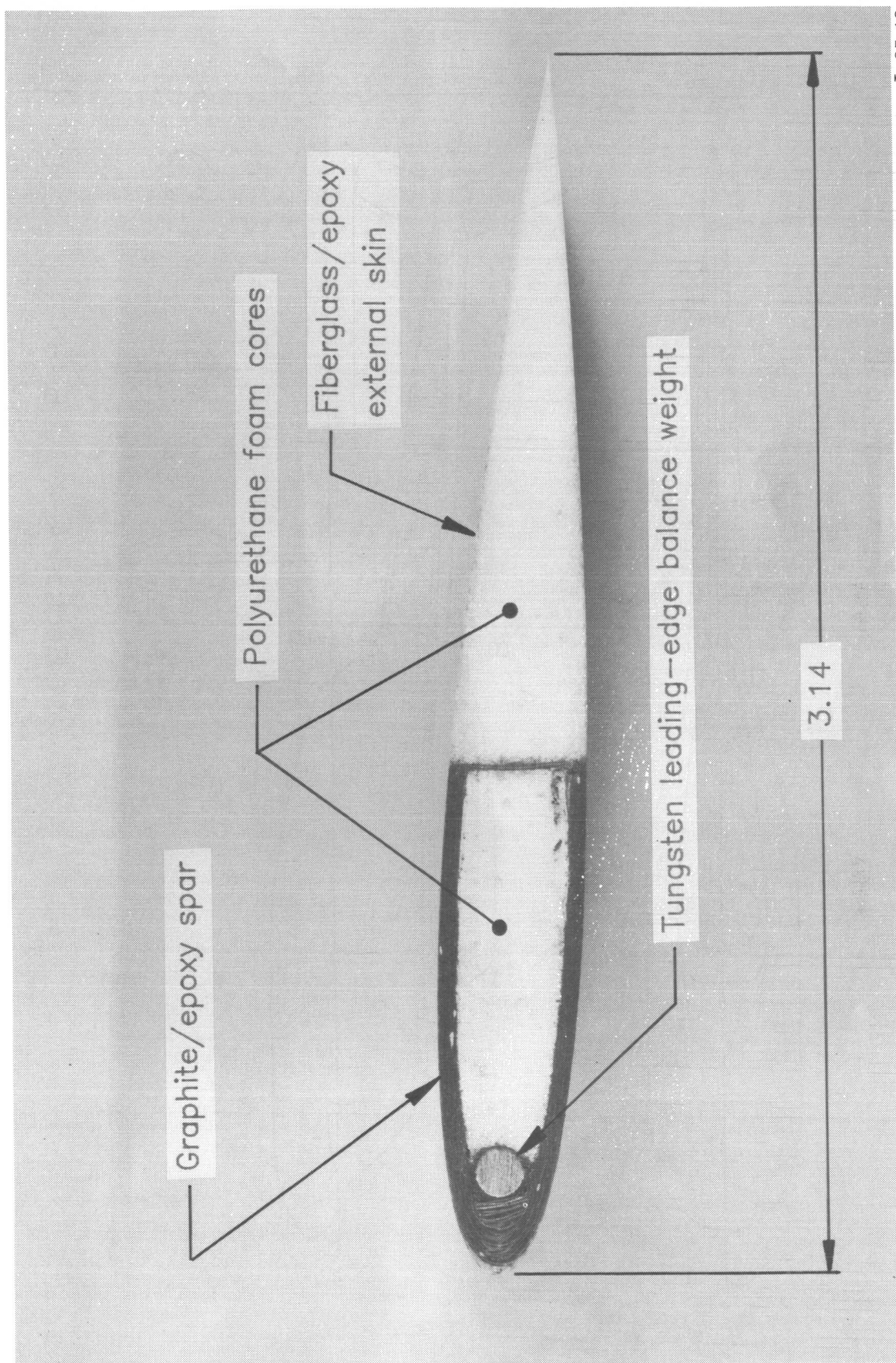
Figure 5. Details of model rotor blade construction. Dimensions are given in inches.

L-85-10

19

Model as tested

0.21–scale AHIP contour

Section A–A   B–B   C–C
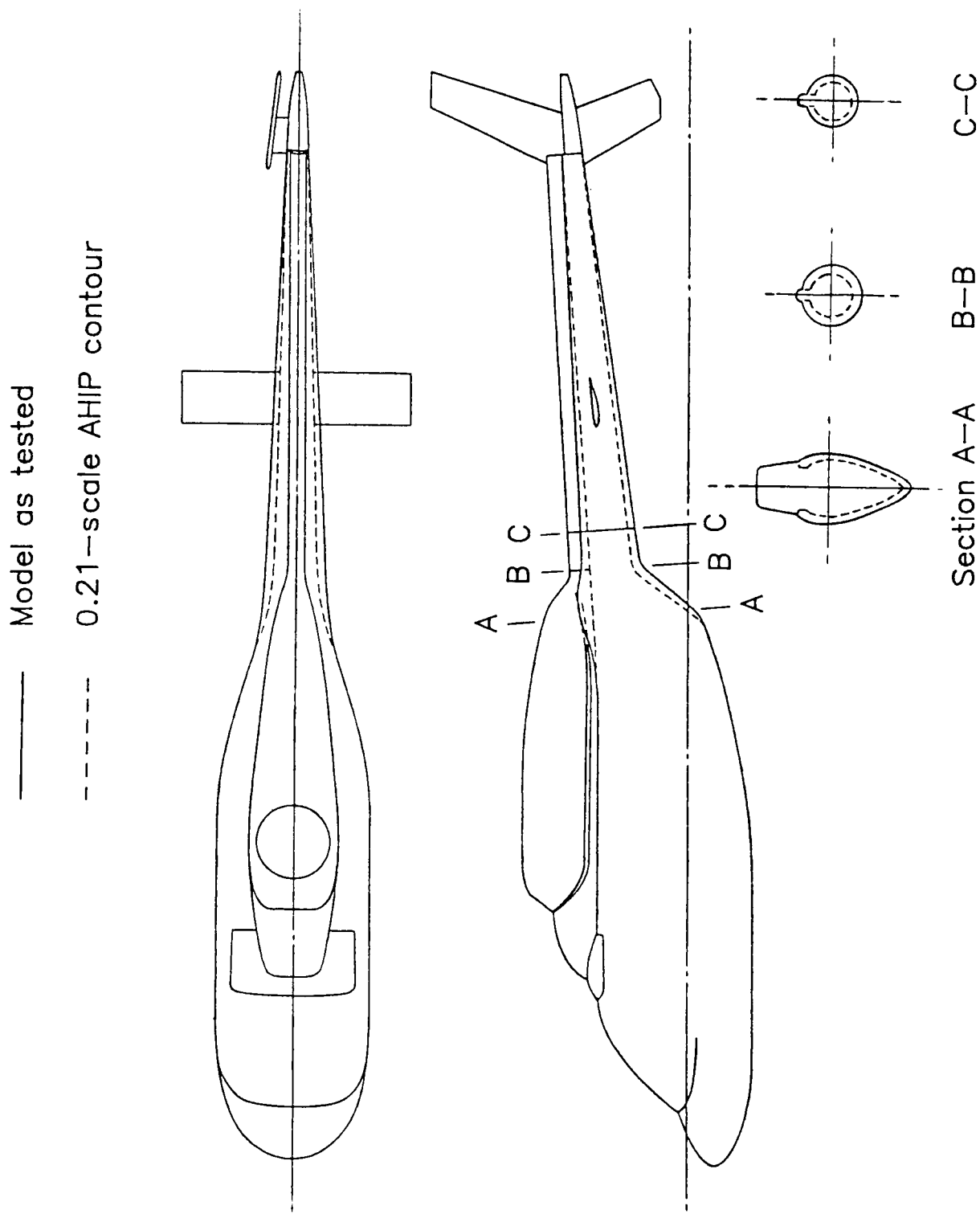
(a) Fuselage contours.

Figure 6. Comparison of geometries of full-scale helicopter and model.

Model blade used in tests

0.21—scale AHIP blade

Ω

Distance along blade, in.
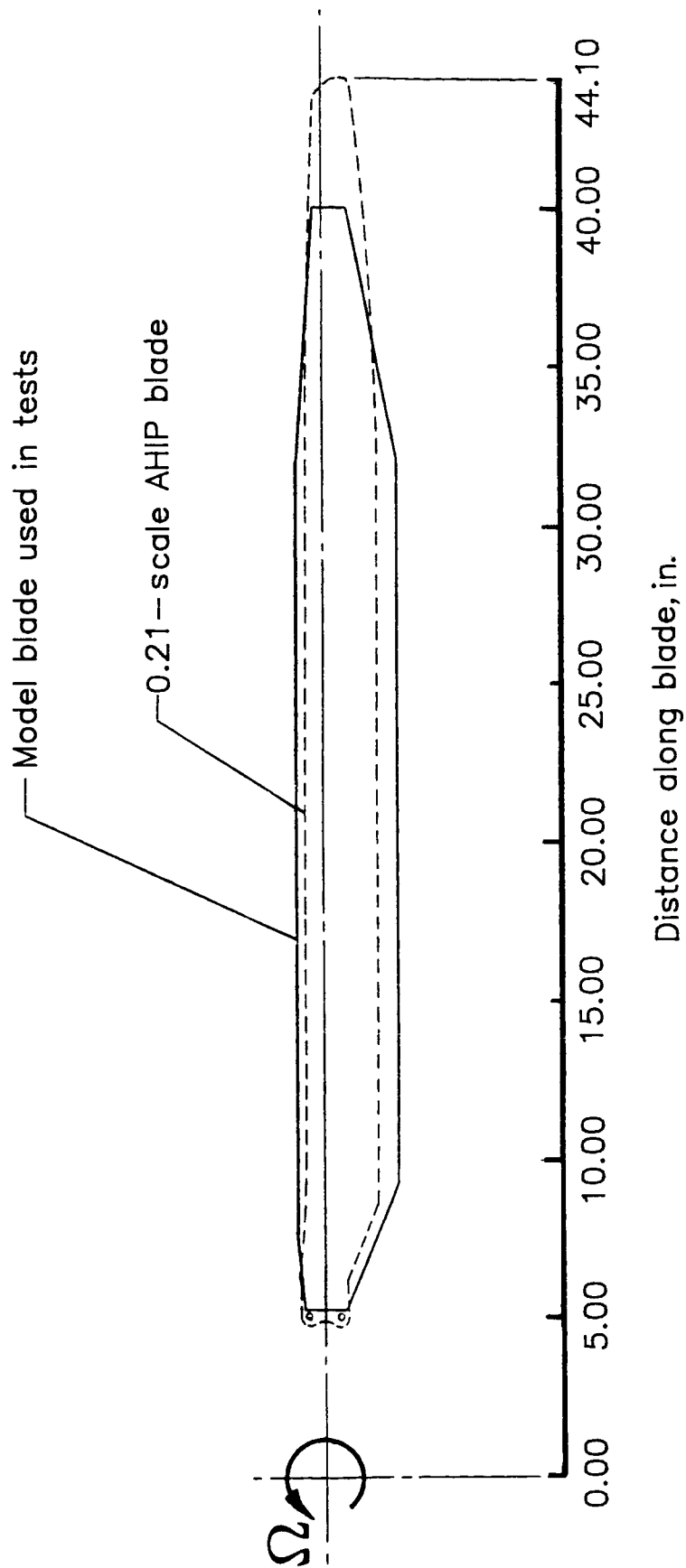
(b) Comparison of blade planforms.

Figure 6. Concluded.

21
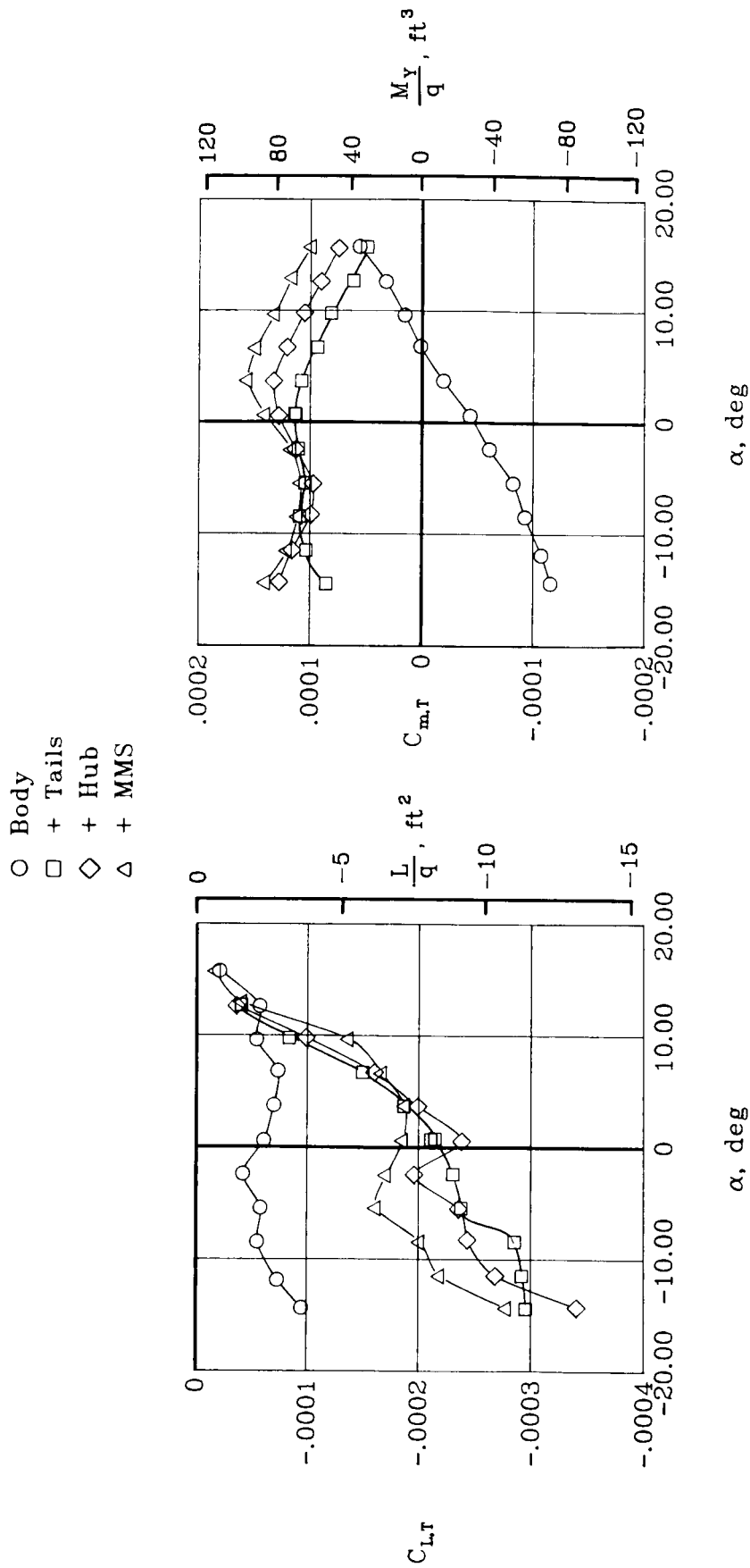
(a) Lift and pitching-moment characteristics.

Figure 7. Total longitudinal aerodynamic characteristics of model with rotor off.
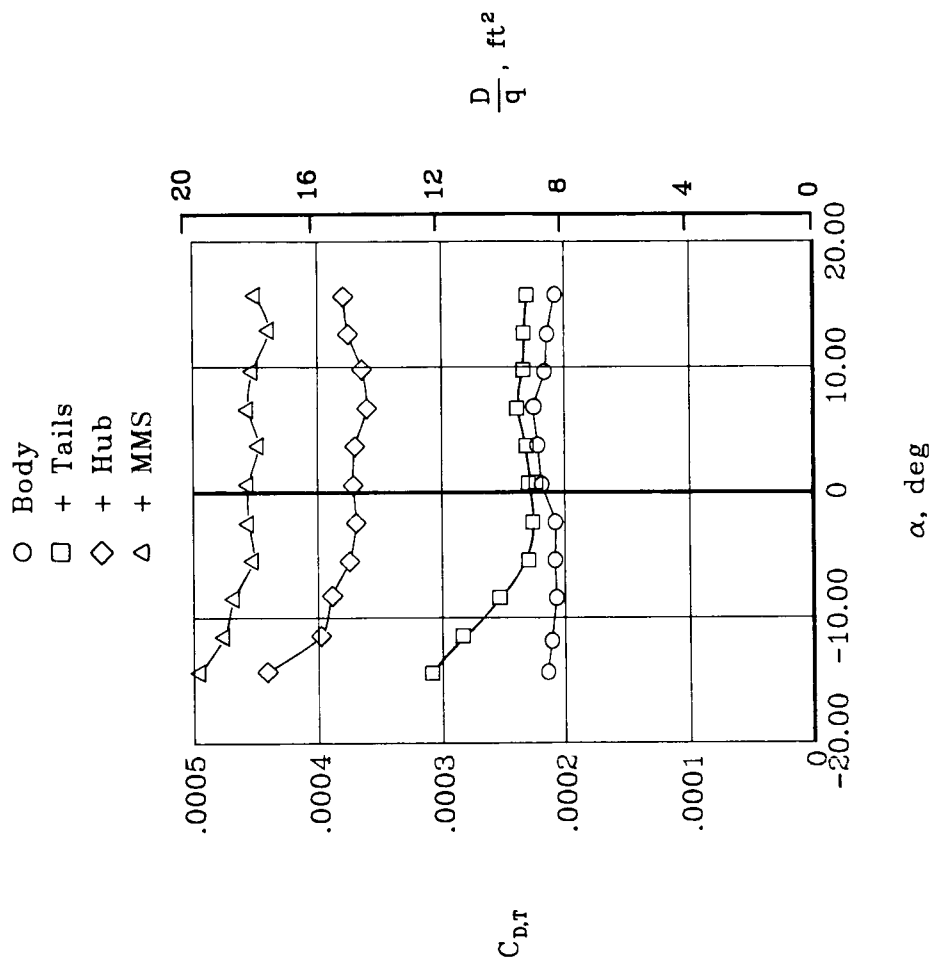
(b) Drag characteristics.

Figure 7. Concluded.
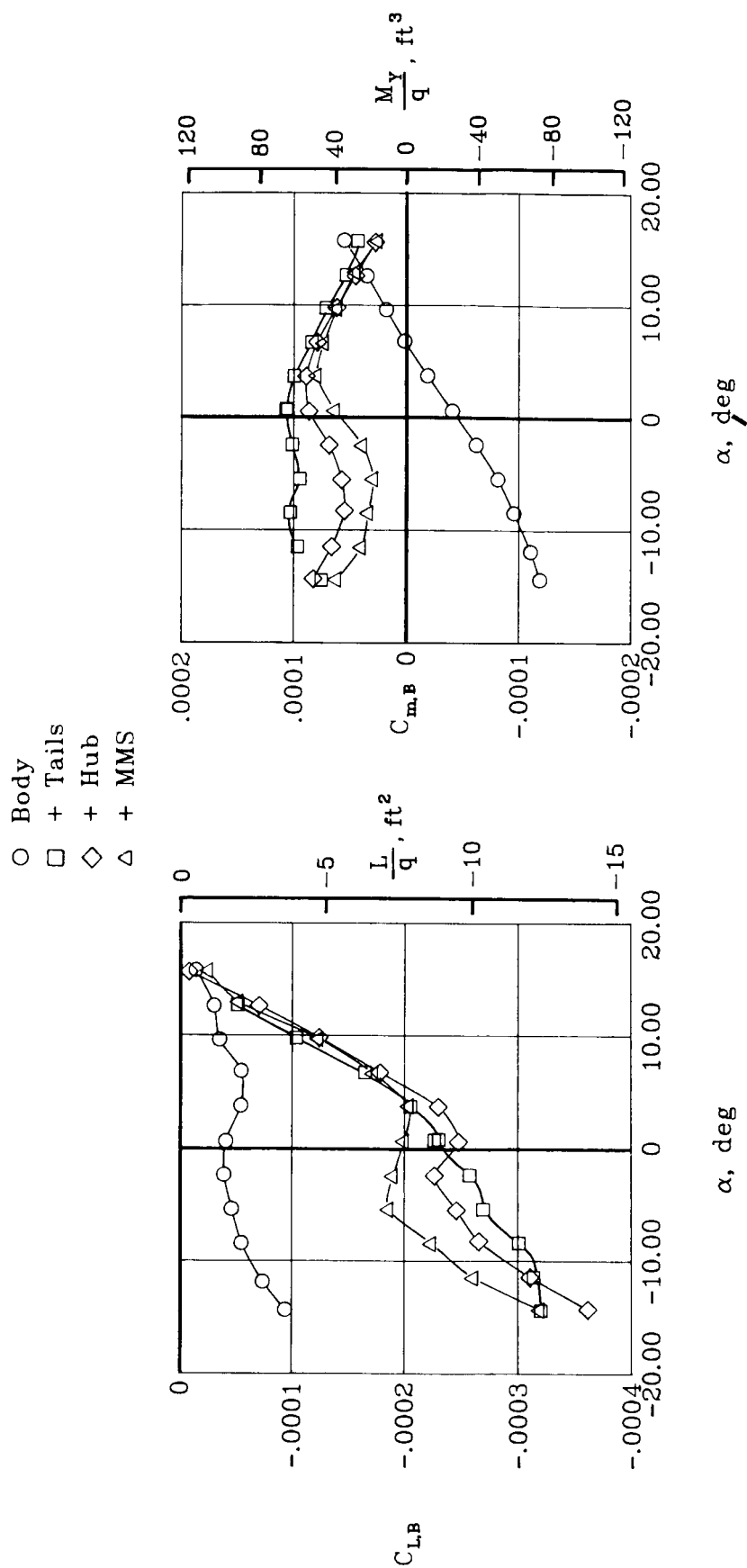
(a) Lift and pitching-moment characteristics.

Figure 8. Airframe longitudinal aerodynamic characteristics of model with rotor off.
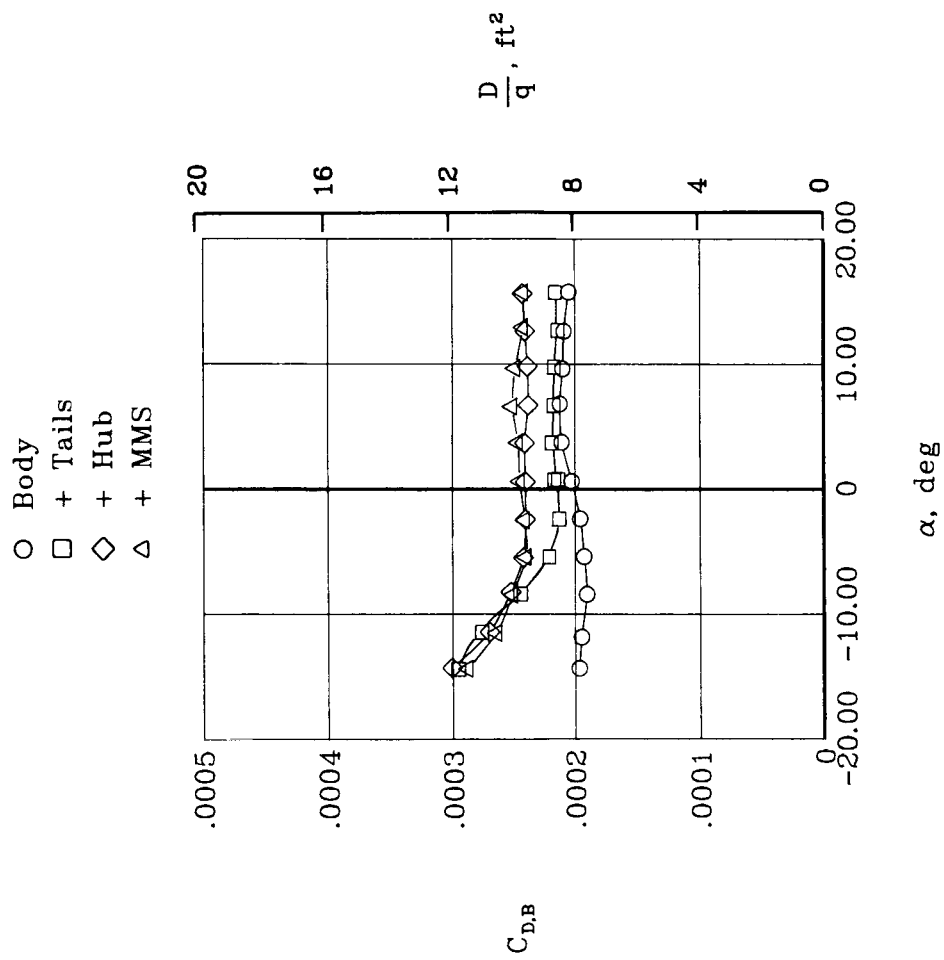
(b) Drag characteristics.

Figure 8. Concluded.
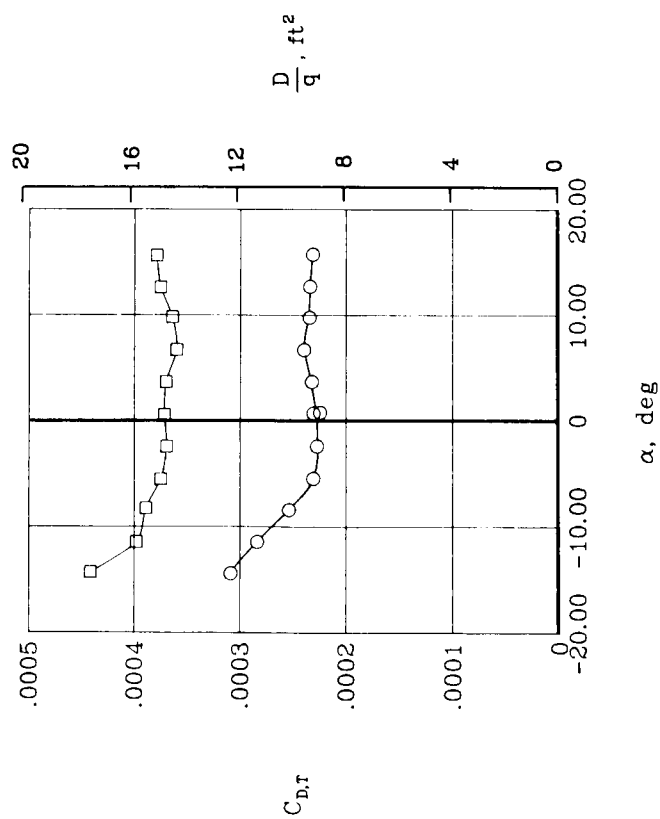
(a) Total drag characteristics.
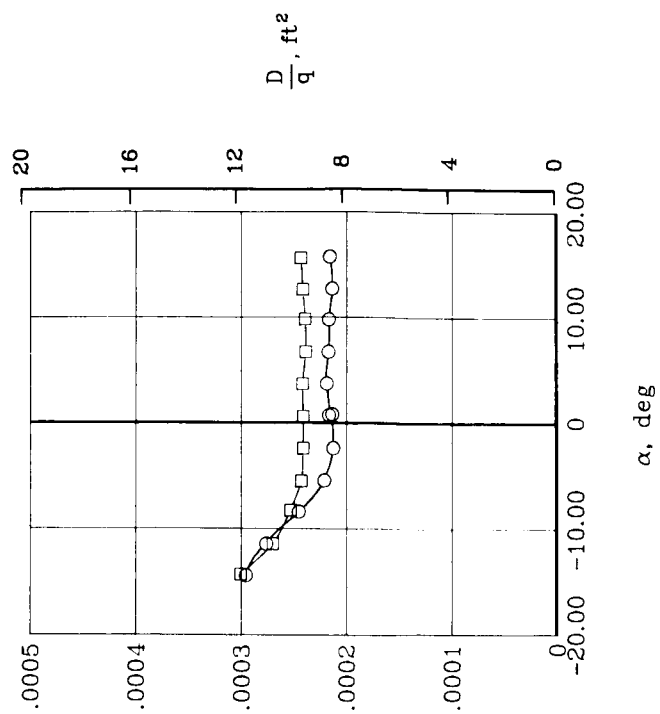
(b) Airframe drag characteristics.

Figure 9. Interference effect of hub on airframe drag characteristics with rotor off.

O Body + tails
□ + Hub + MMS

(b) Airframe drag characteristics.

(a) Total drag characteristics.

Figure 10. Interference effect of MMS on drag characteristics with rotor off.
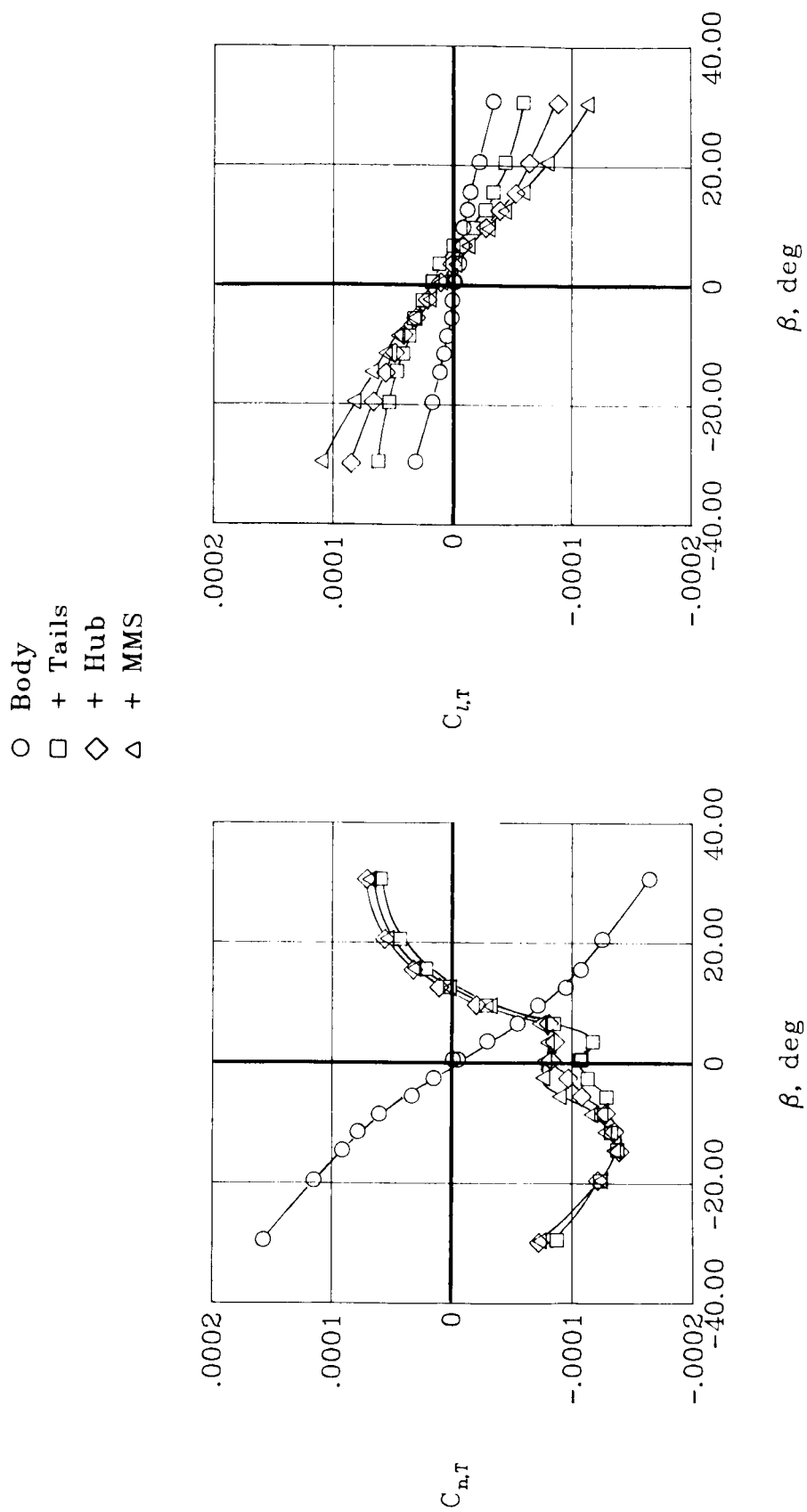
(a) Total yawing-moment and rolling-moment characteristics.

Figure 11. Total lateral-directional aerodynamic characteristics of model with rotor off. $\alpha = 0°$.
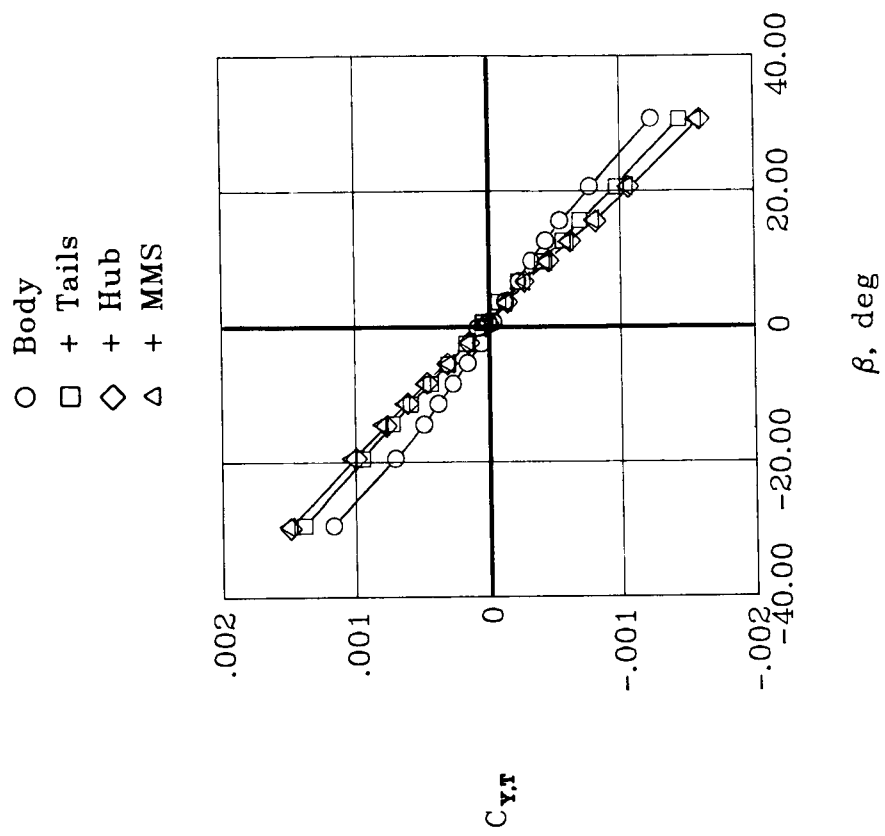
(b) Total side-force characteristics.

Figure 11. Concluded.

Legend:
○ Body
□ + Tails
◇ + Hub
△ + MMS

$C_{l,B}$

$C_{n,B}$

β, deg

β, deg
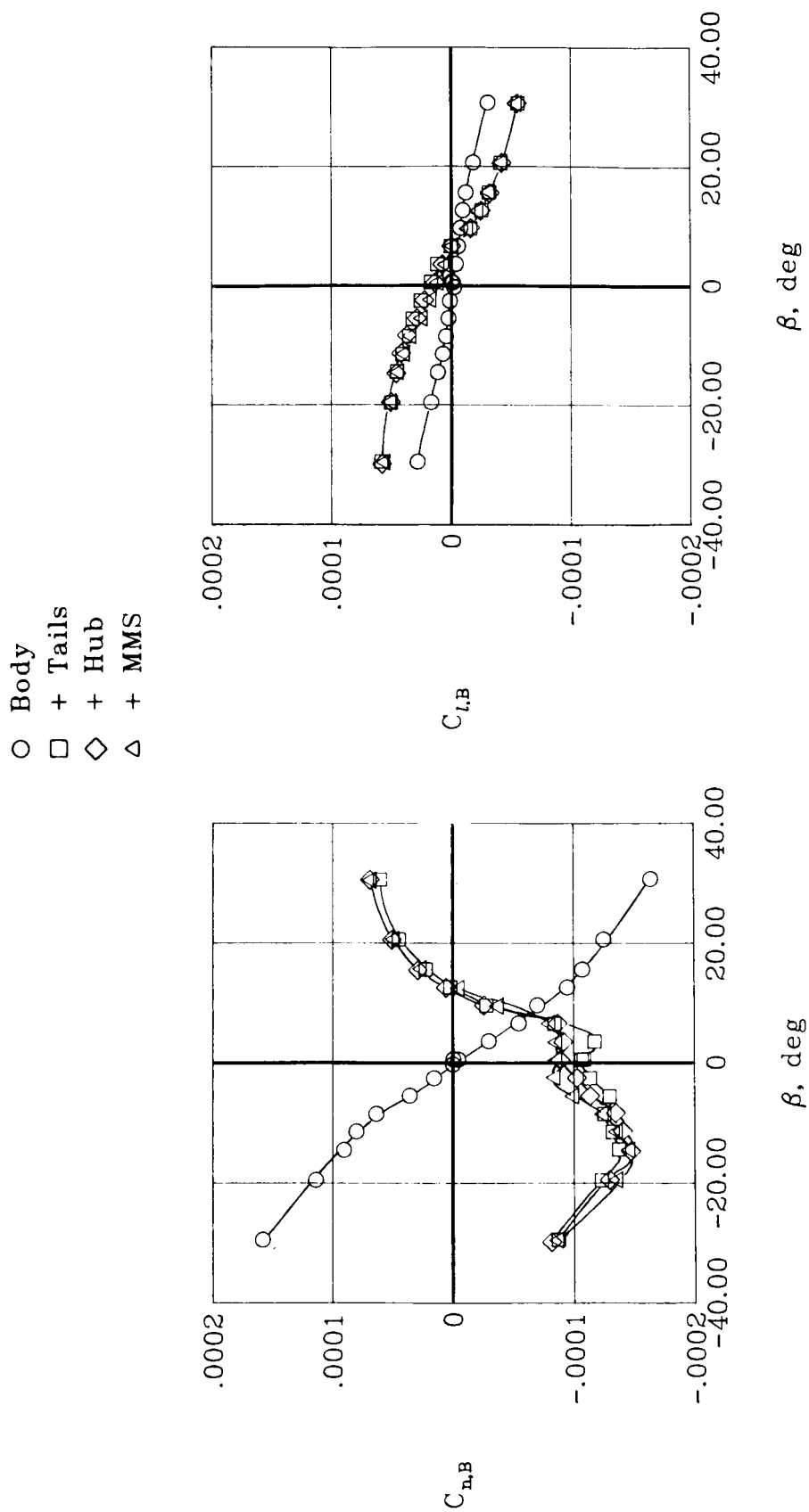
(a) Airframe lateral-directional aerodynamic characteristics.

Figure 12. Airframe yawing-moment and rolling-moment characteristics of model with rotor off. $\alpha = 0°$.
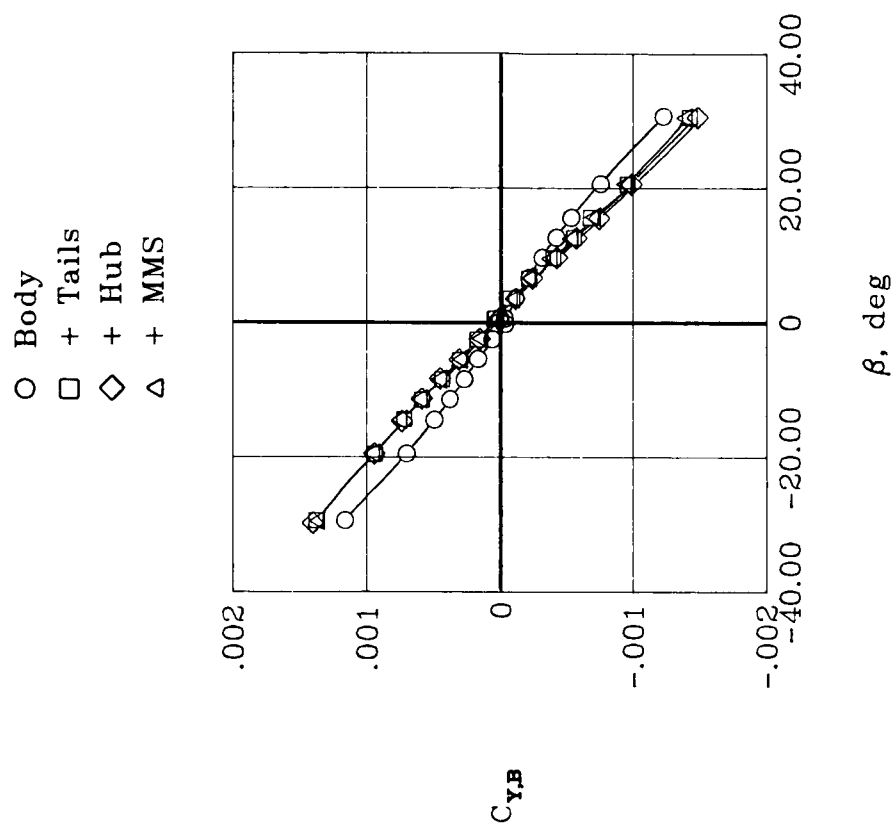
(b) Airframe side-force characteristics.

Figure 12. Concluded.

31
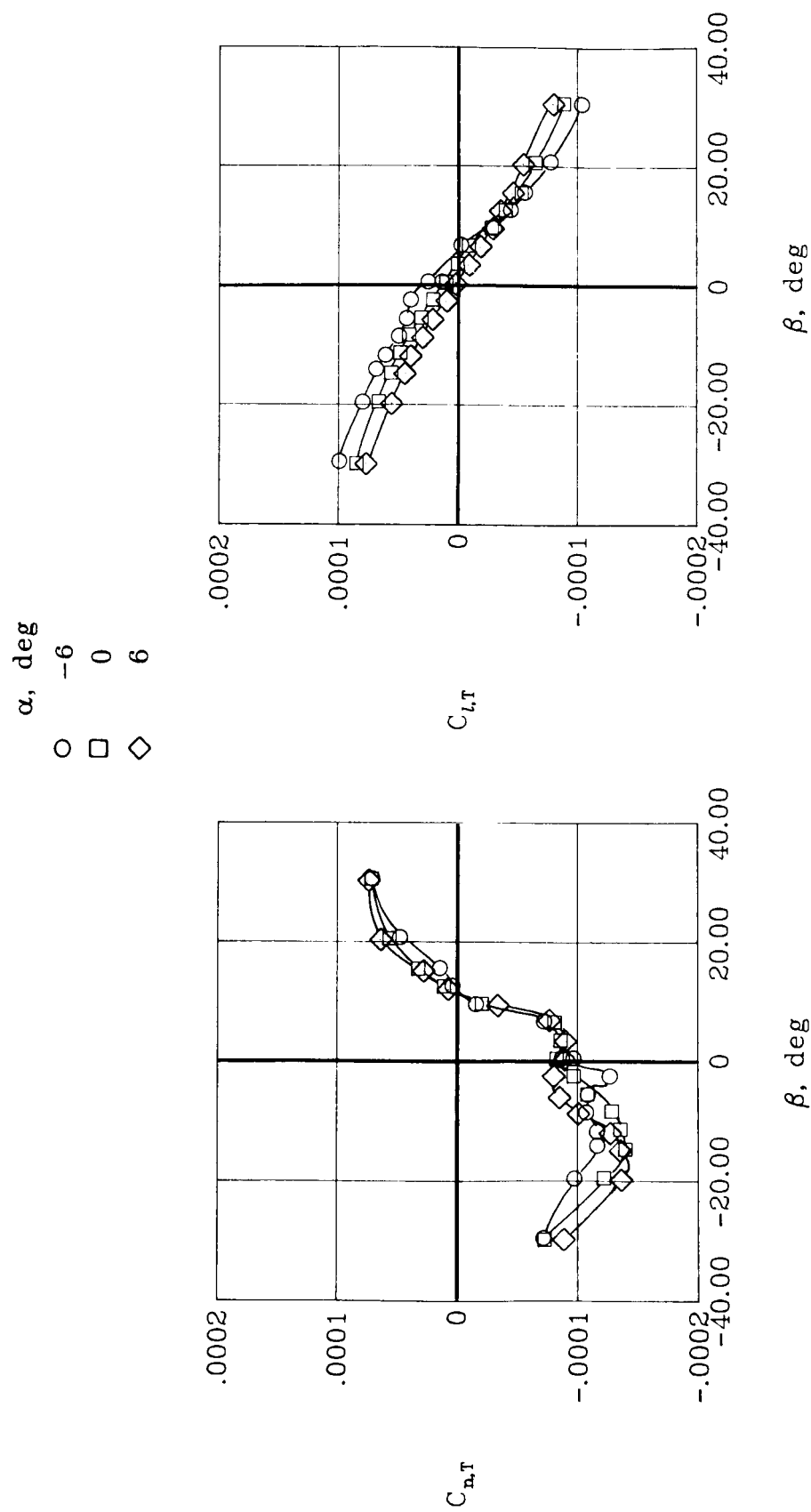
(a) Total yawing-moment and rolling-moment characteristics.

Figure 13. Effect of angle of attack on lateral-directional aerodynamic characteristics of model with rotor off. MMS off.
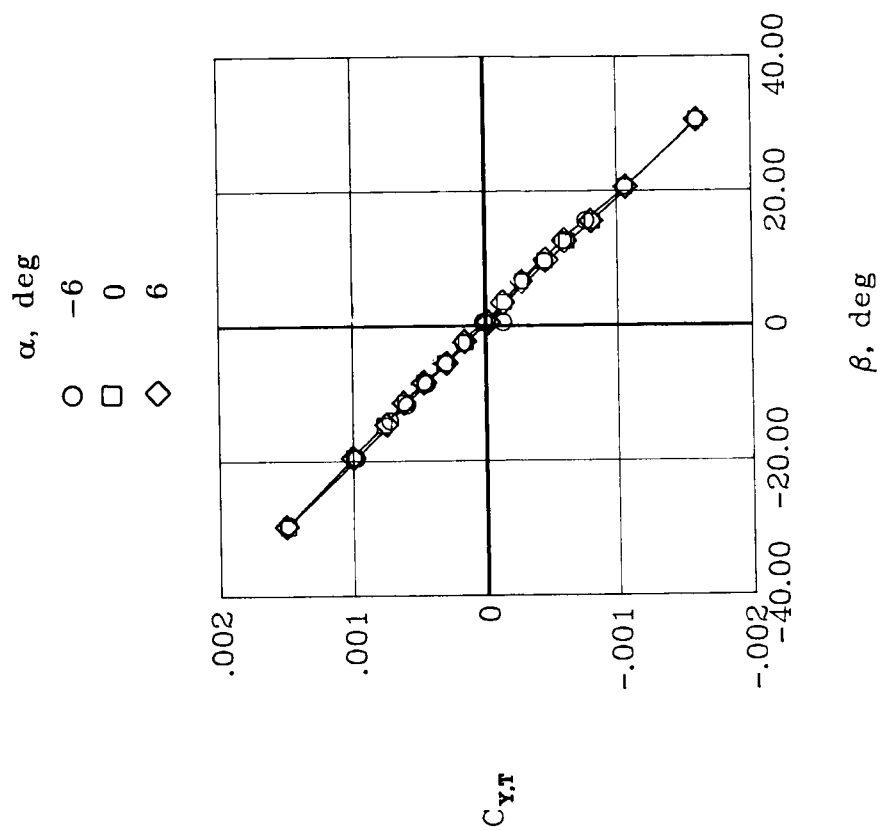
(b) Total side-force characteristics.

Figure 13. Continued.
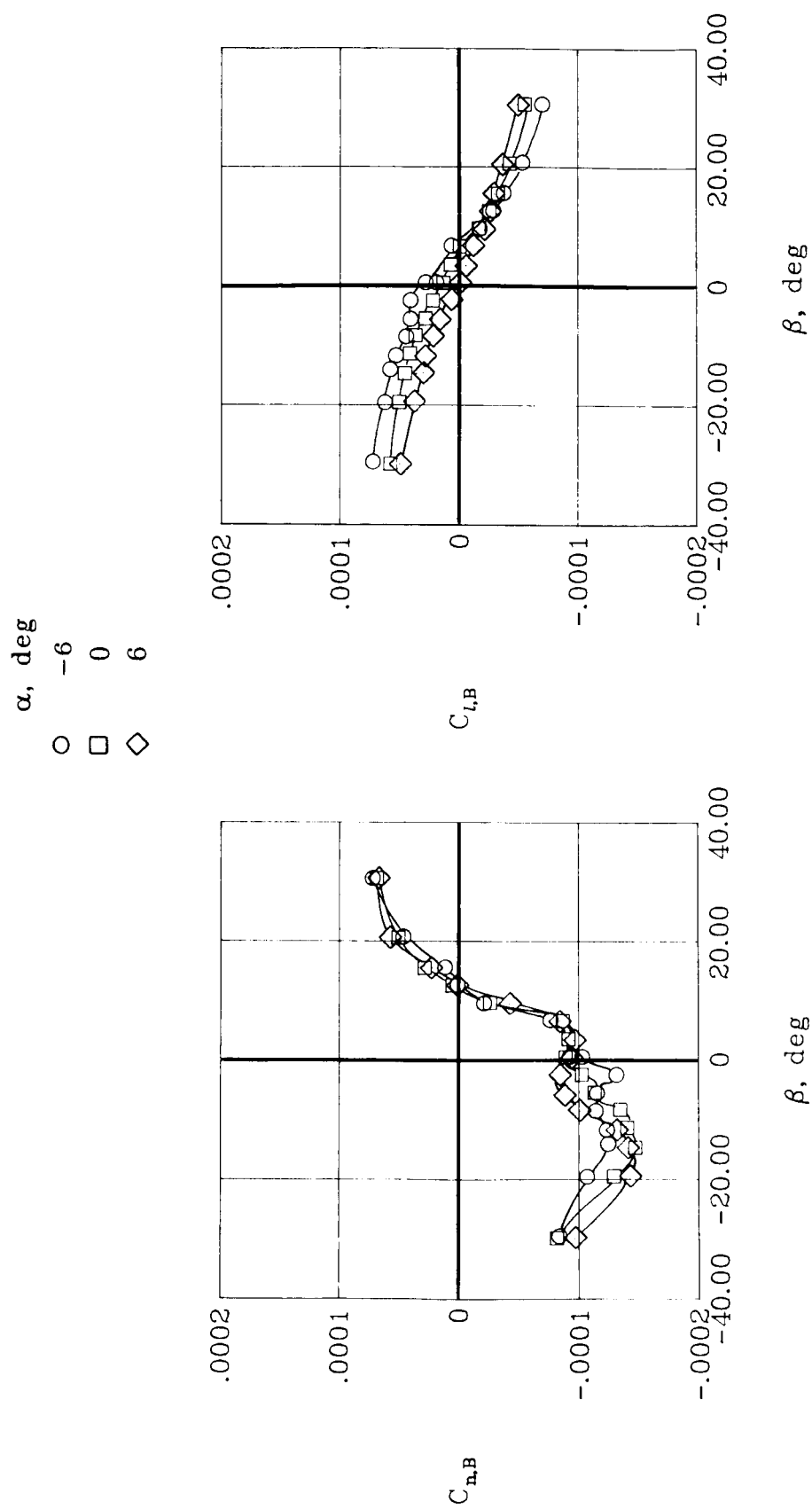
(c) Airframe yawing-moment and rolling-moment characteristics.

Figure 13. Continued.
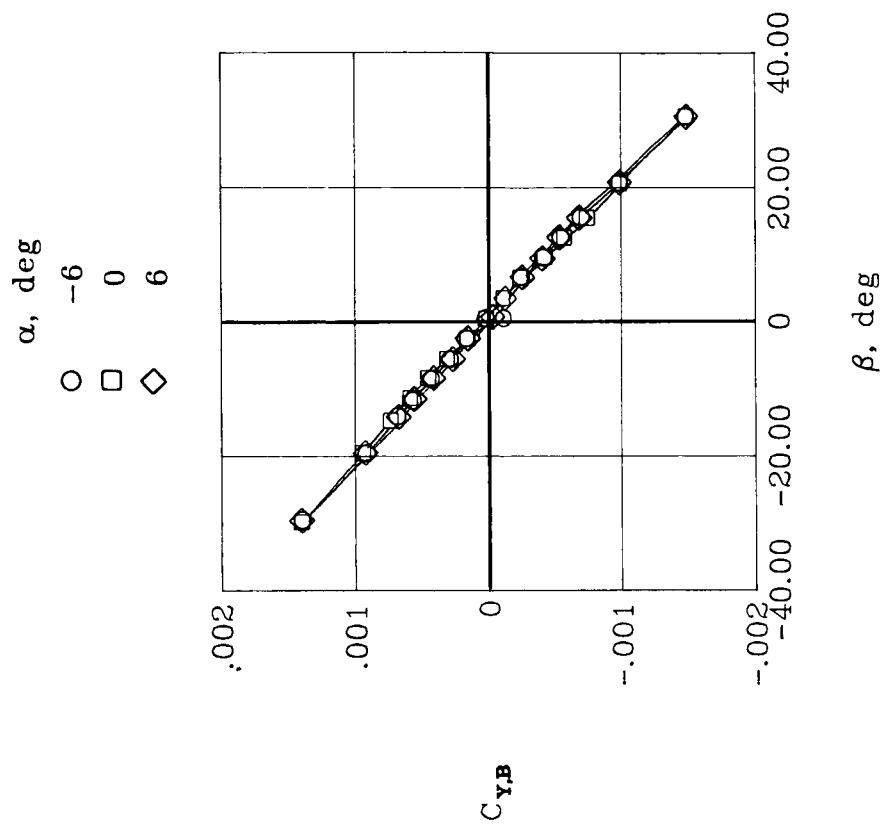
(d) Airframe side-force characteristics.

Figure 13. Concluded.

α, deg
○ -6
□ 0
◇ 6

$C_{l,T}$

β, deg

(a) Total yawing-moment and rolling-moment characteristics.

$C_{n,T}$

β, deg
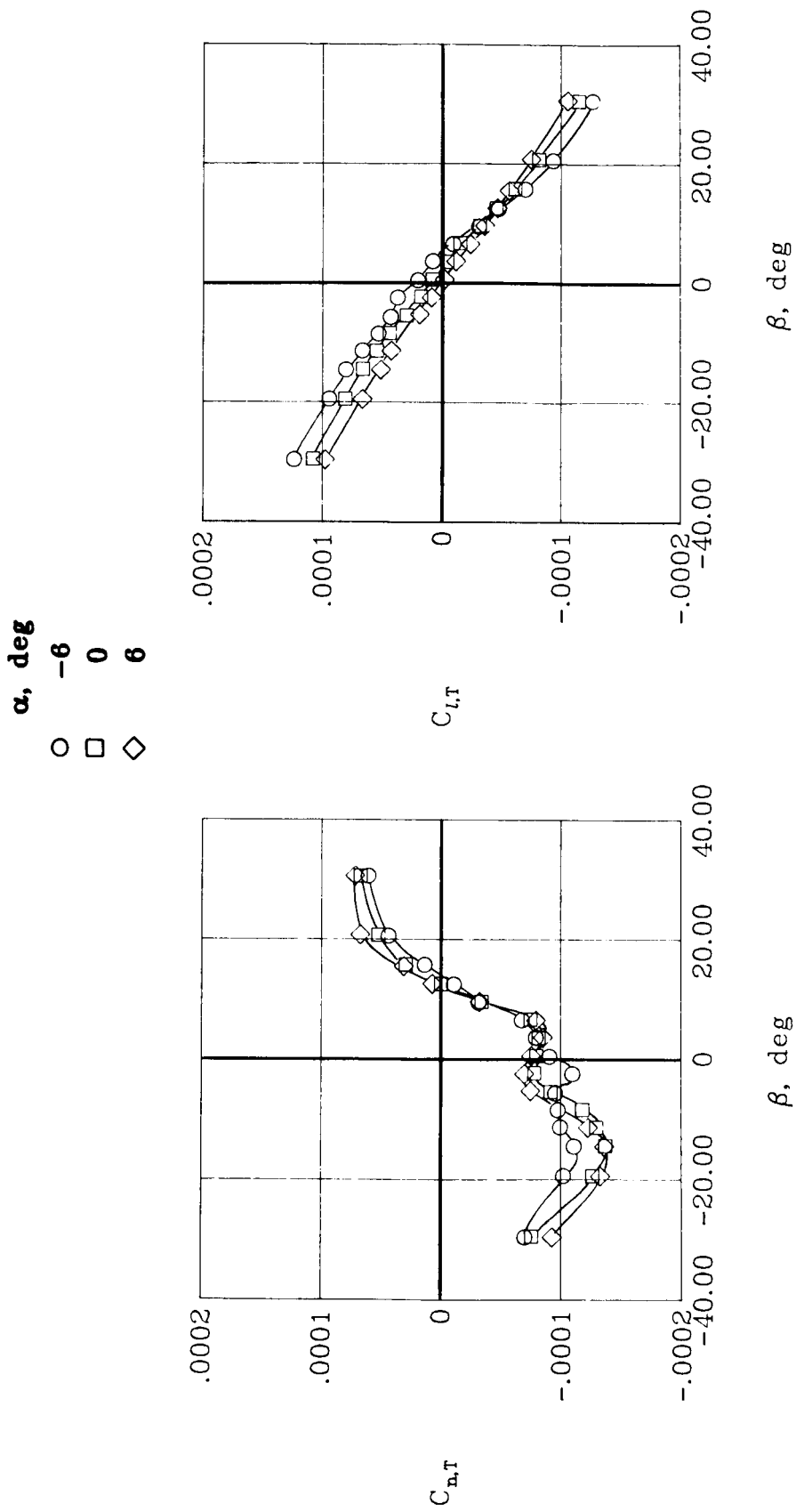
Figure 14. Effect of angle of attack on lateral-directional aerodynamic characteristics of model with rotor off. MMS on.
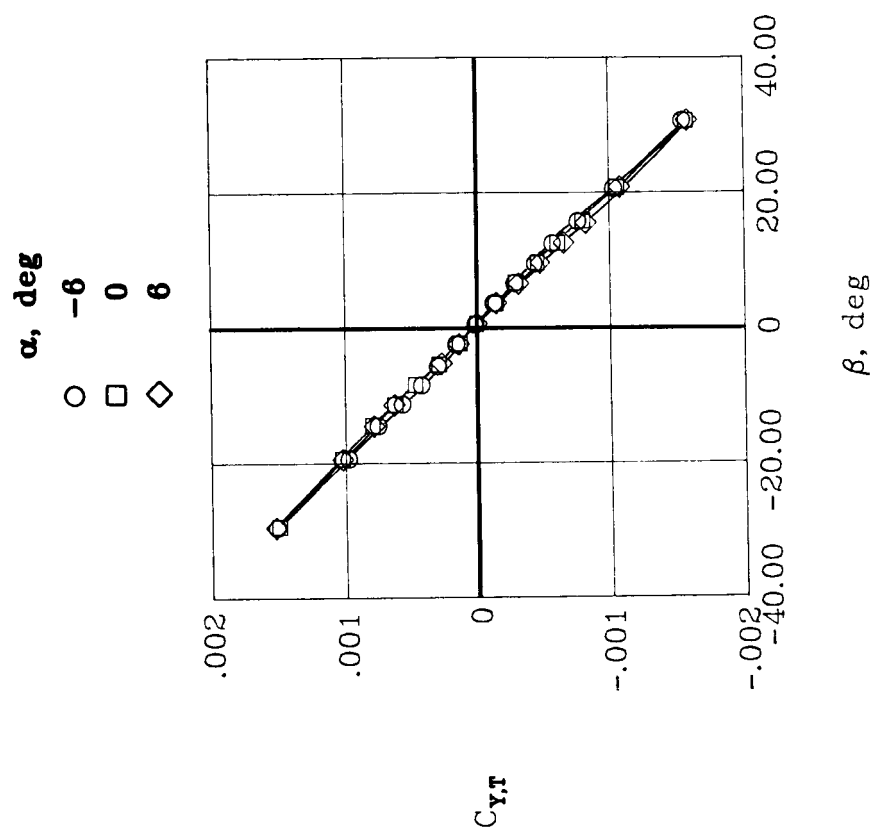
(b) Total side-force characteristics.

Figure 14. Continued.
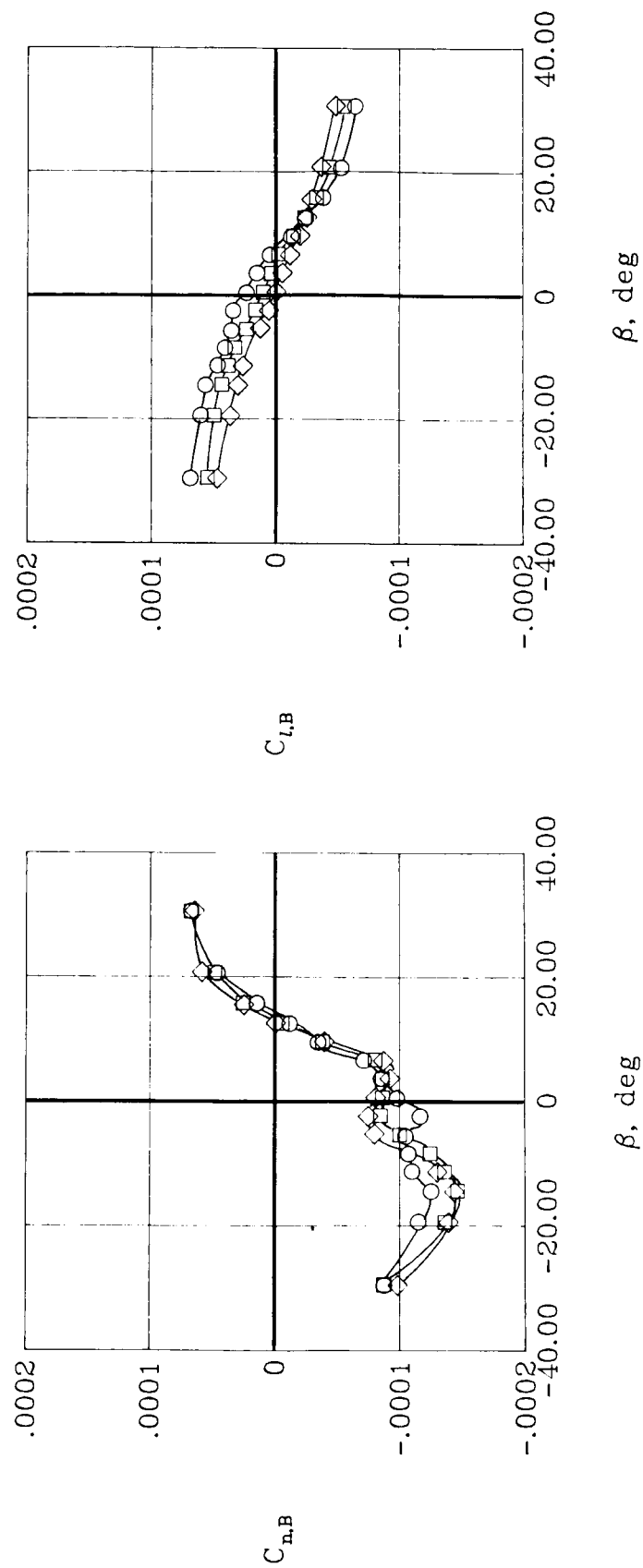
(c) Airframe yawing-moment and rolling-moment characteristics.

Figure 14. Continued.
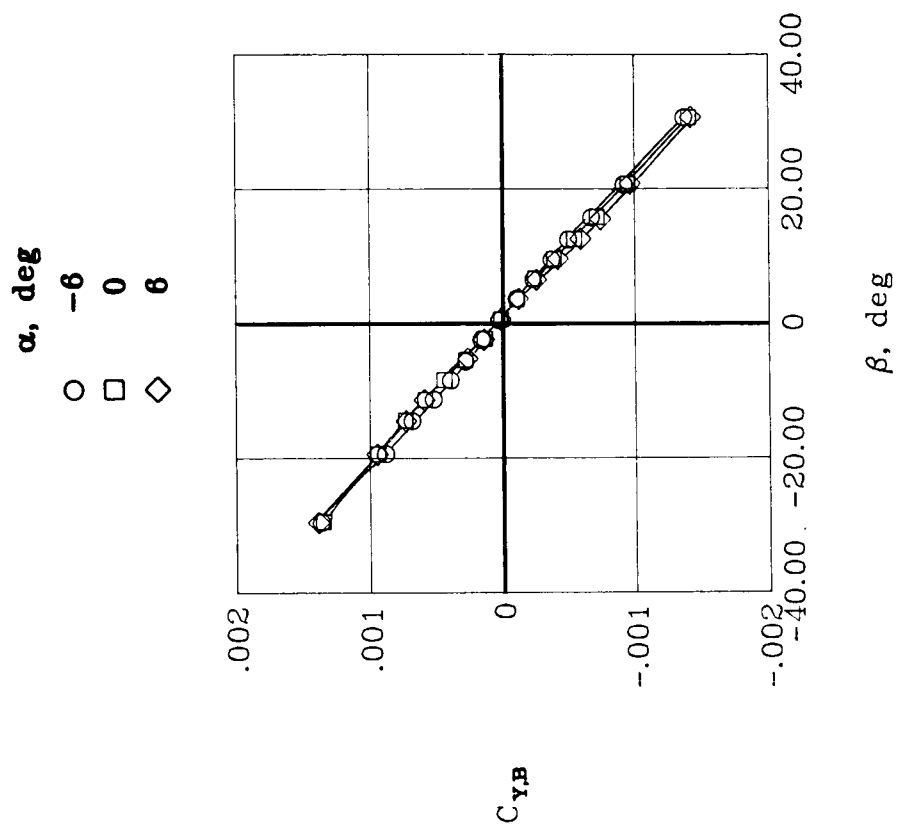
(d) Airframe side-force characteristics.

Figure 14. Concluded.

(a) Lift and pitching-moment characteristics.
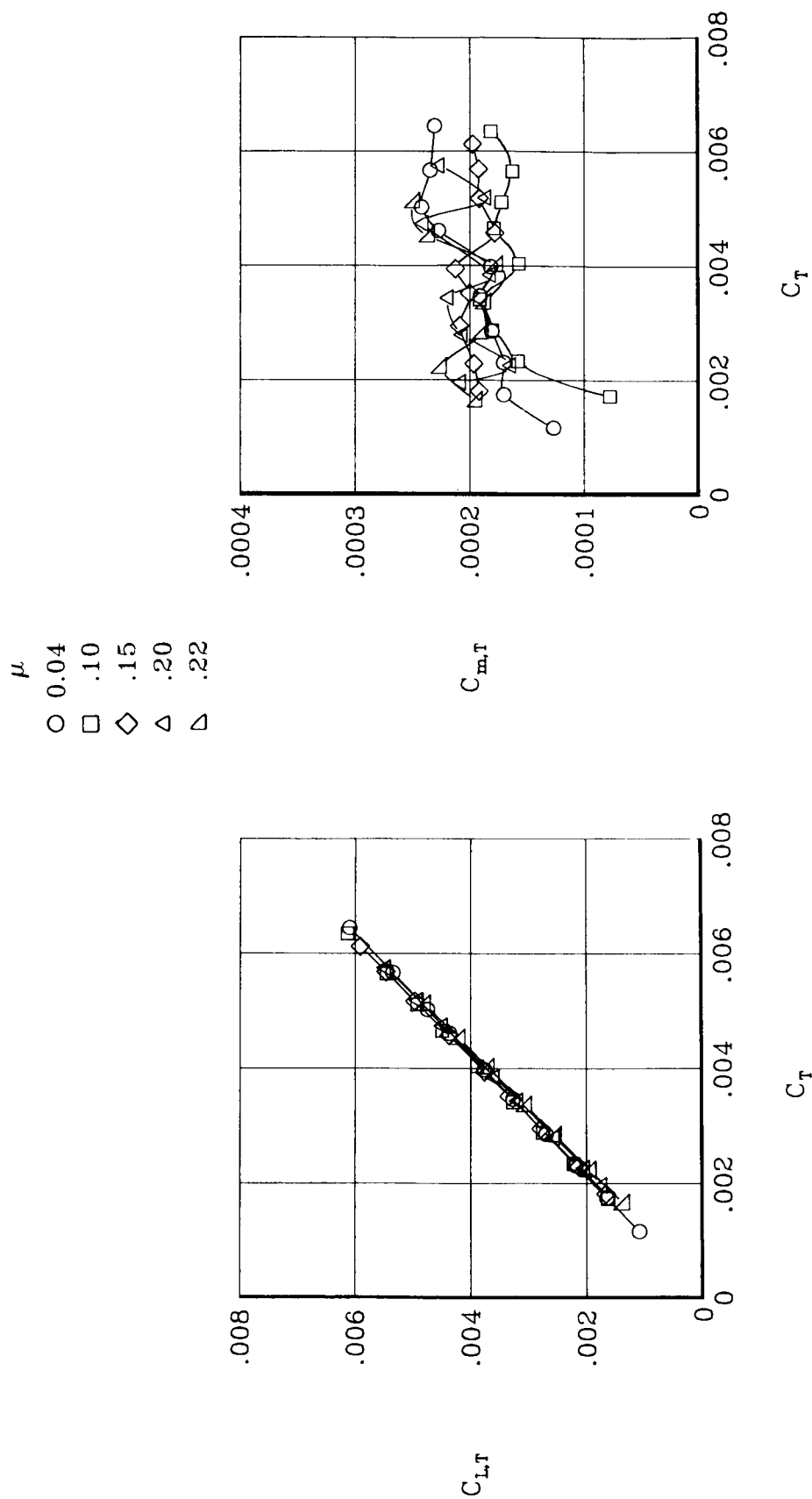
Figure 15. Effect of thrust coefficient on total longitudinal aerodynamic characteristics of model with rotor on. $\alpha = -1.2°$.
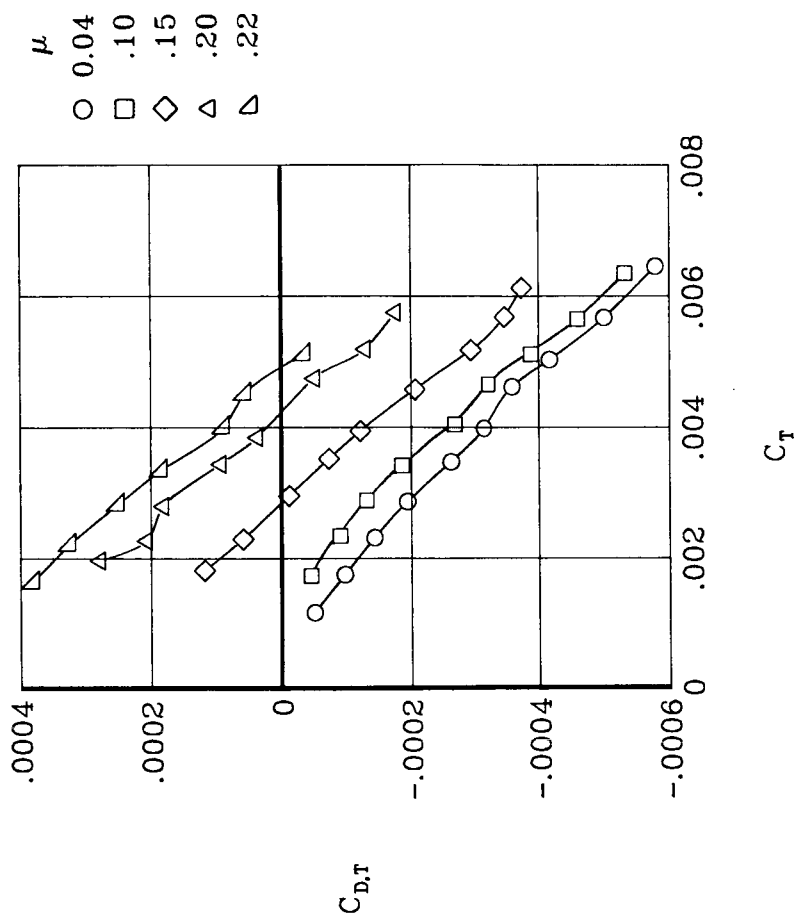
(b) Drag characteristics.

Figure 15. Concluded.
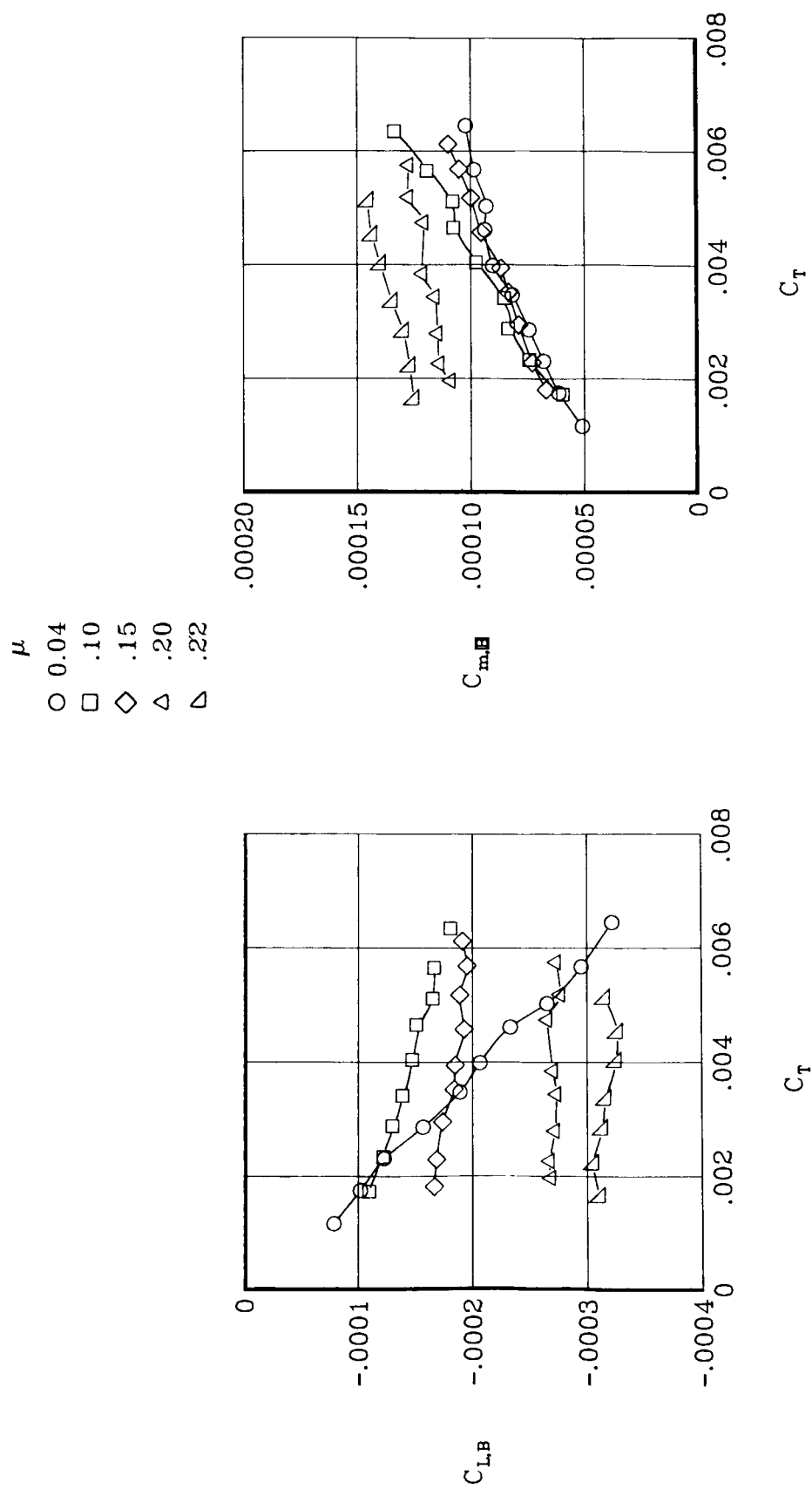
(a) Lift and pitching-moment characteristics.

Figure 16. Effect of thrust coefficient on airframe longitudinal aerodynamic characteristics of model with rotor on. $\alpha = -1.2°$.
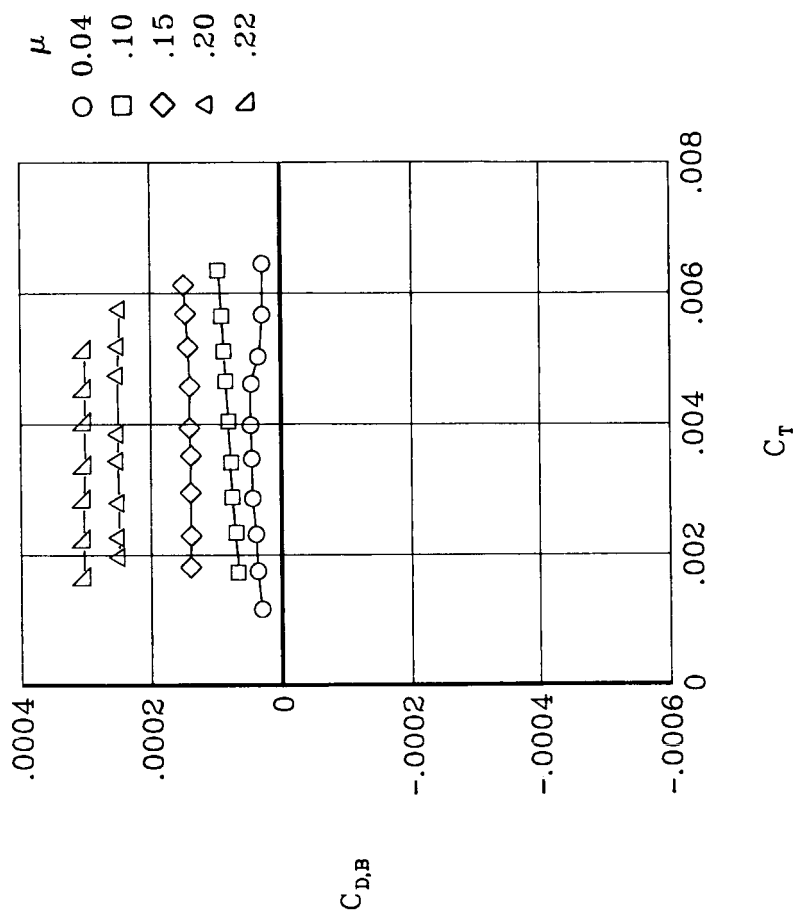
(b) Drag characteristics.

Figure 16. Concluded.
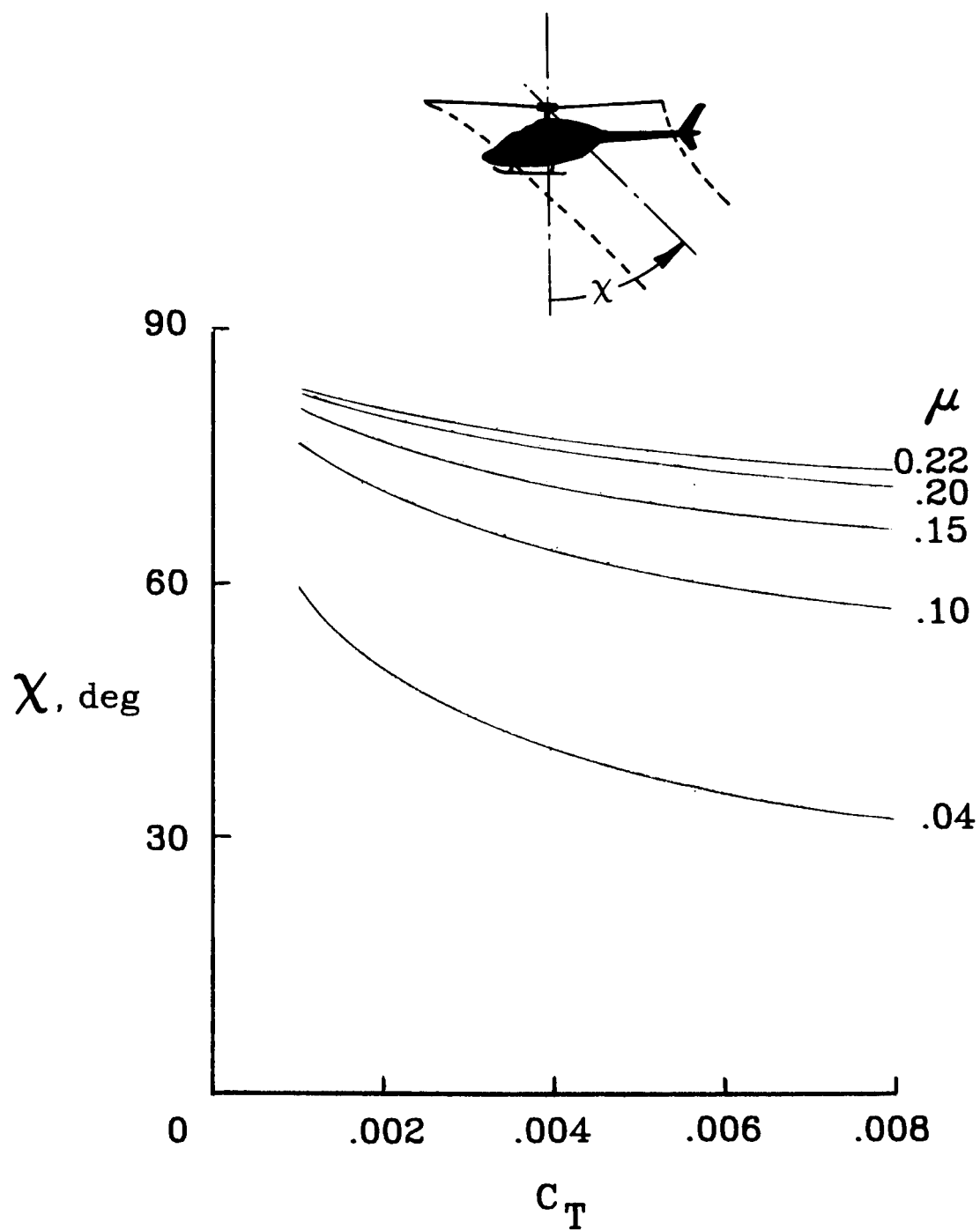
Figure 17. Effect of thrust coefficient on wake skew angle.

(b) Drag characteristics.
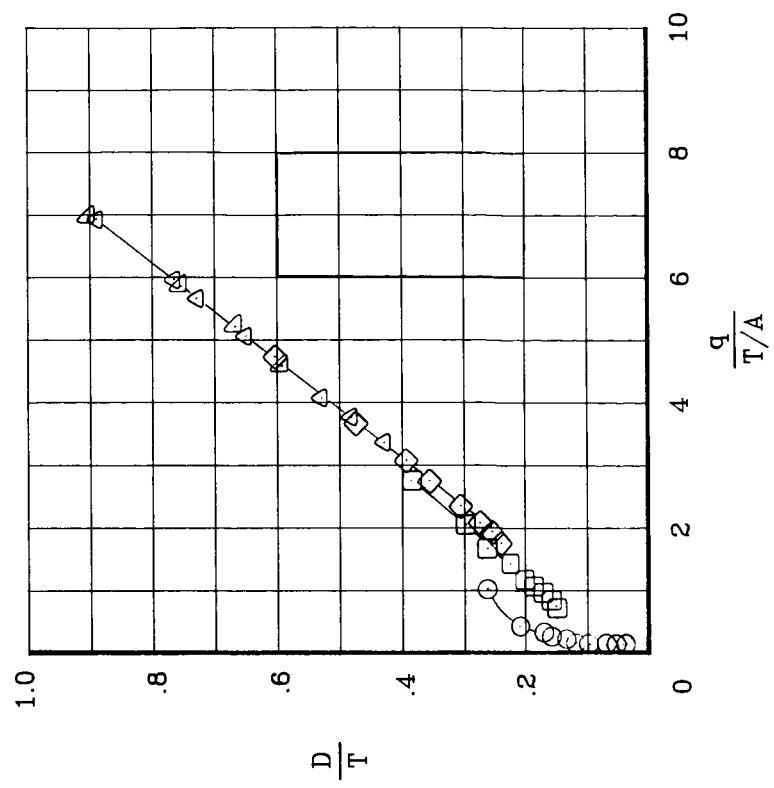
(a) Lift characteristics.

Figure 18. Normalized airframe lift and drag as function of thrust parameter. MMS off; $\alpha = -1.2°$.

45
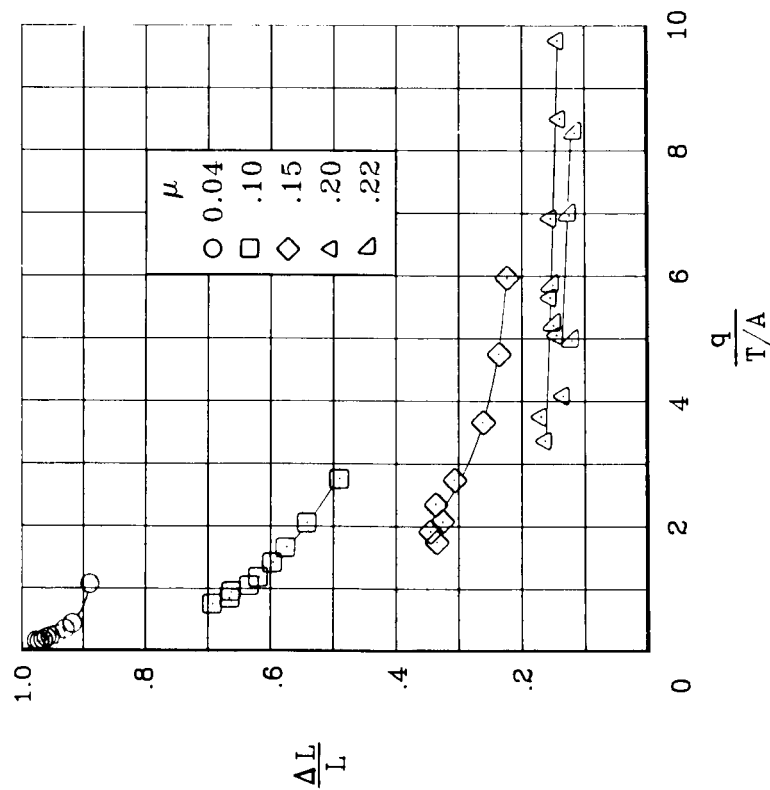
(a) Lift characteristics.
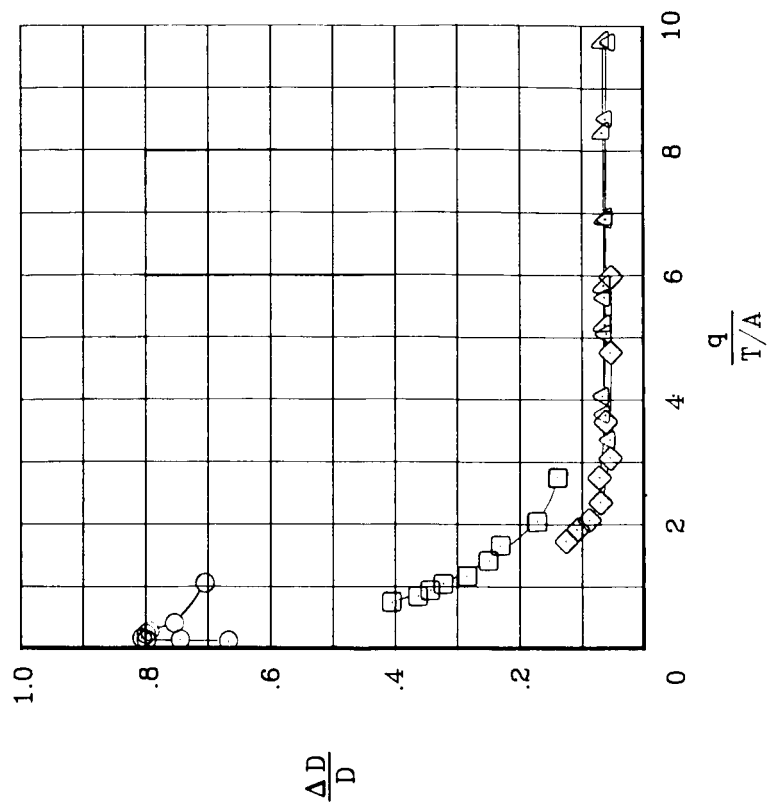
(b) Drag characteristics.

Figure 19. Airframe interference lift and drag as function of thrust parameter. MMS off; $\alpha = -1.2°$.
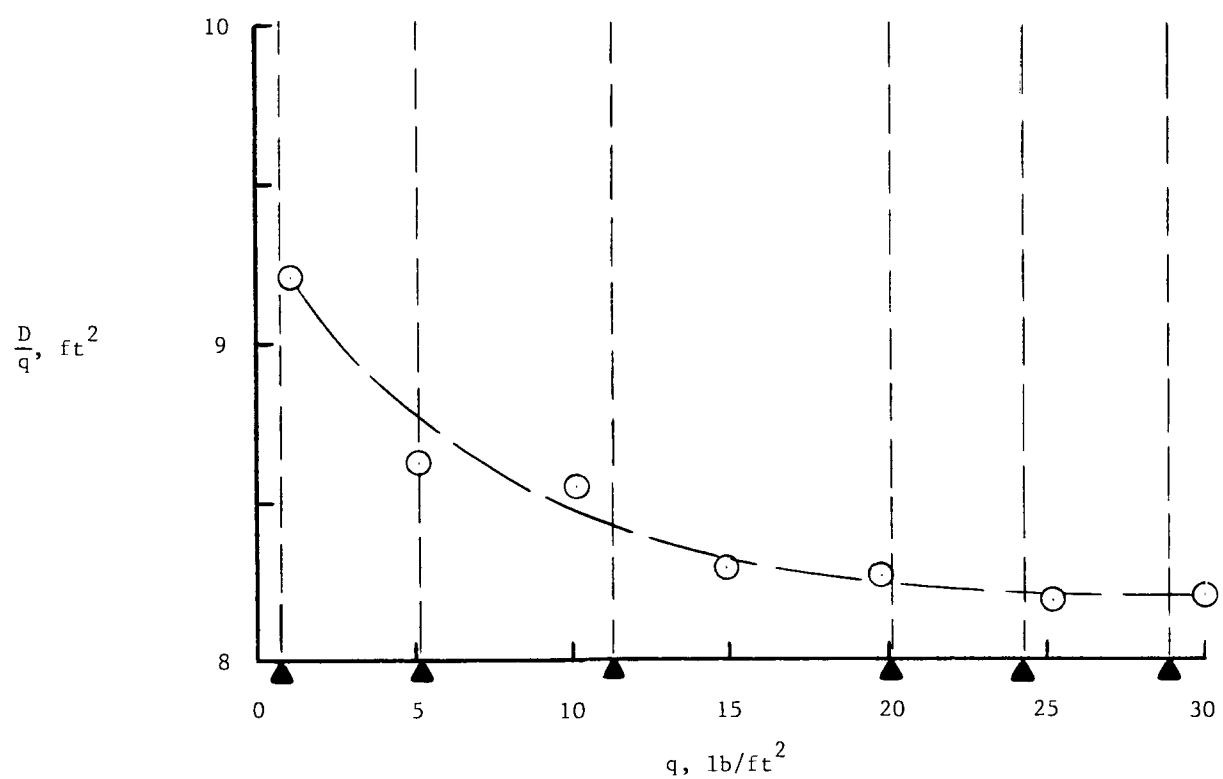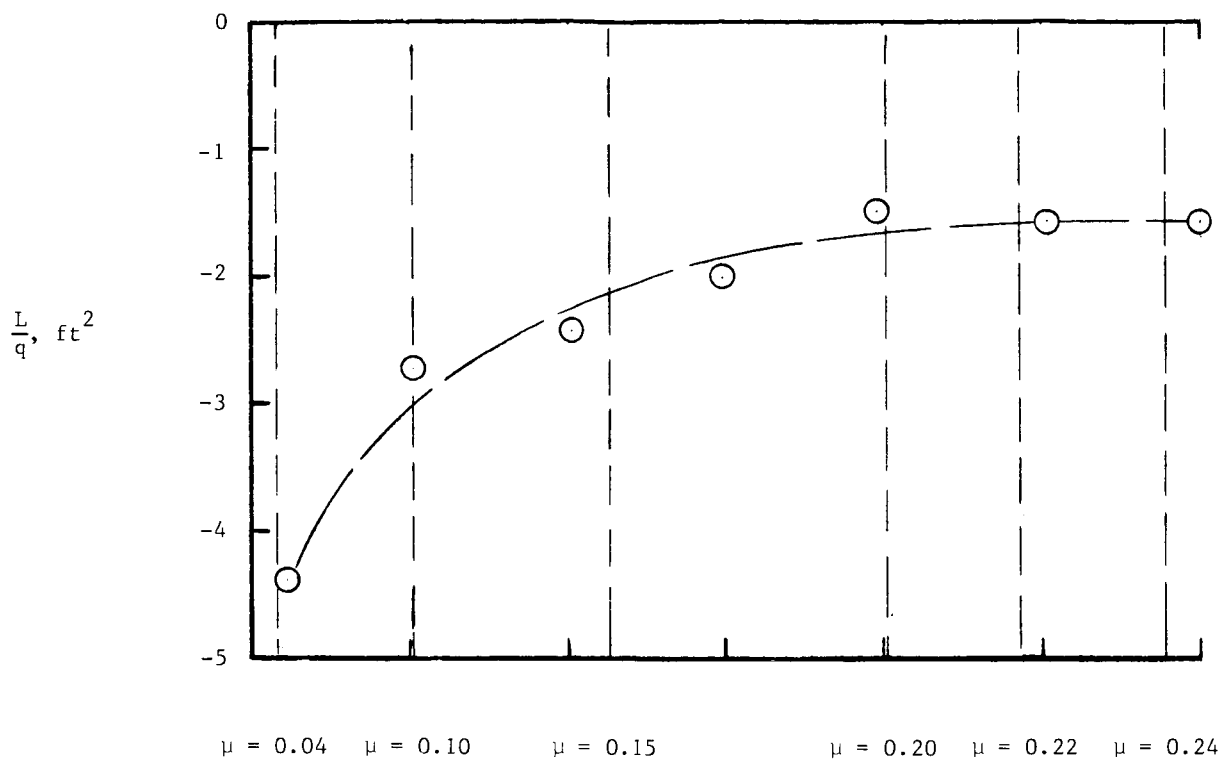
Figure 20. Effect of free-stream dynamic pressure on lift and drag characteristics of model with rotor off. MMS off; $\alpha = -1.2°$.
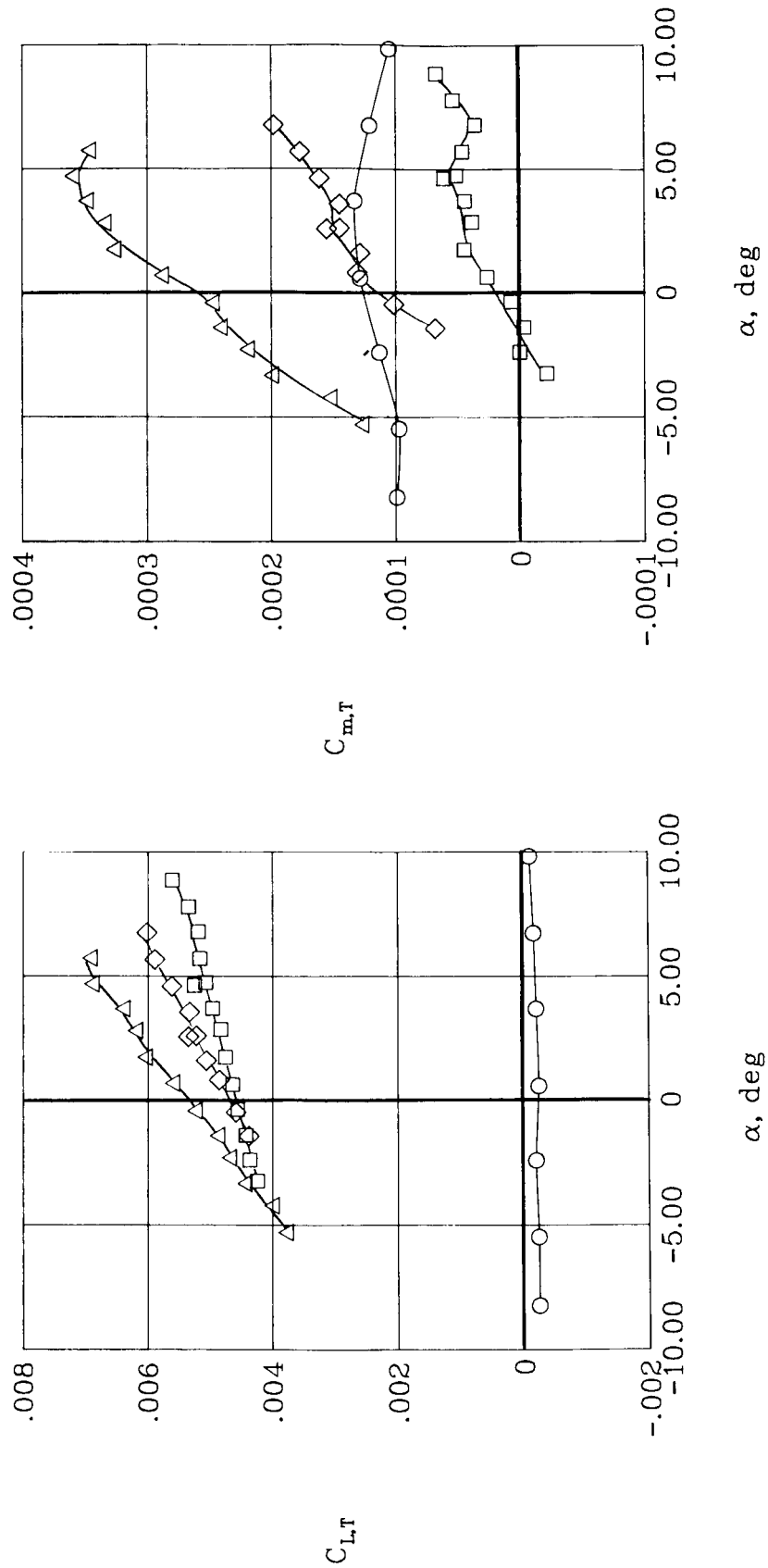
Figure 21. Total lift and pitching-moment characteristics of model. MMS off.
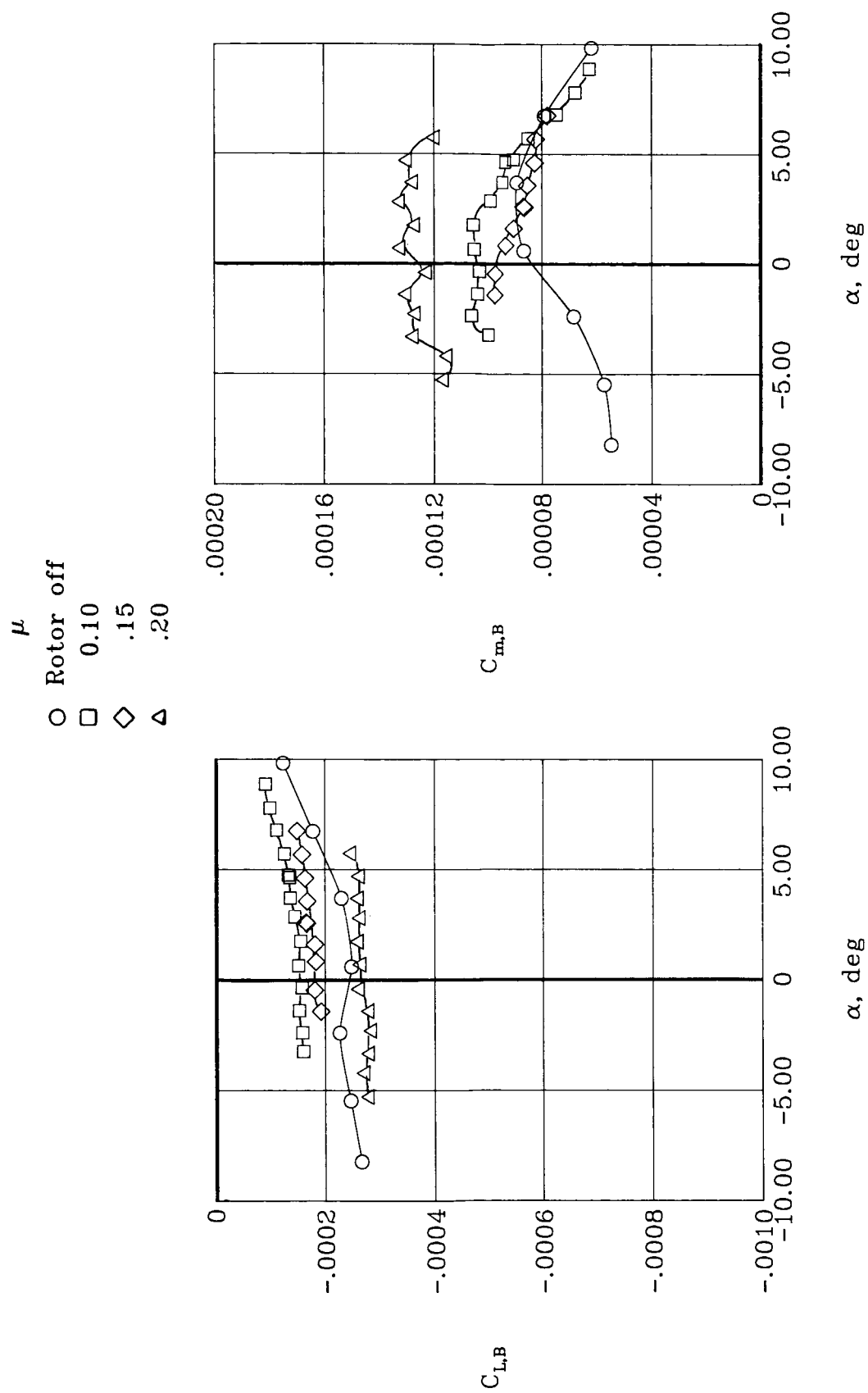
Figure 22. Airframe lift and pitching-moment characteristics. MMS off.

$C_{L,T}$

α, deg

$C_{m,T}$

α, deg
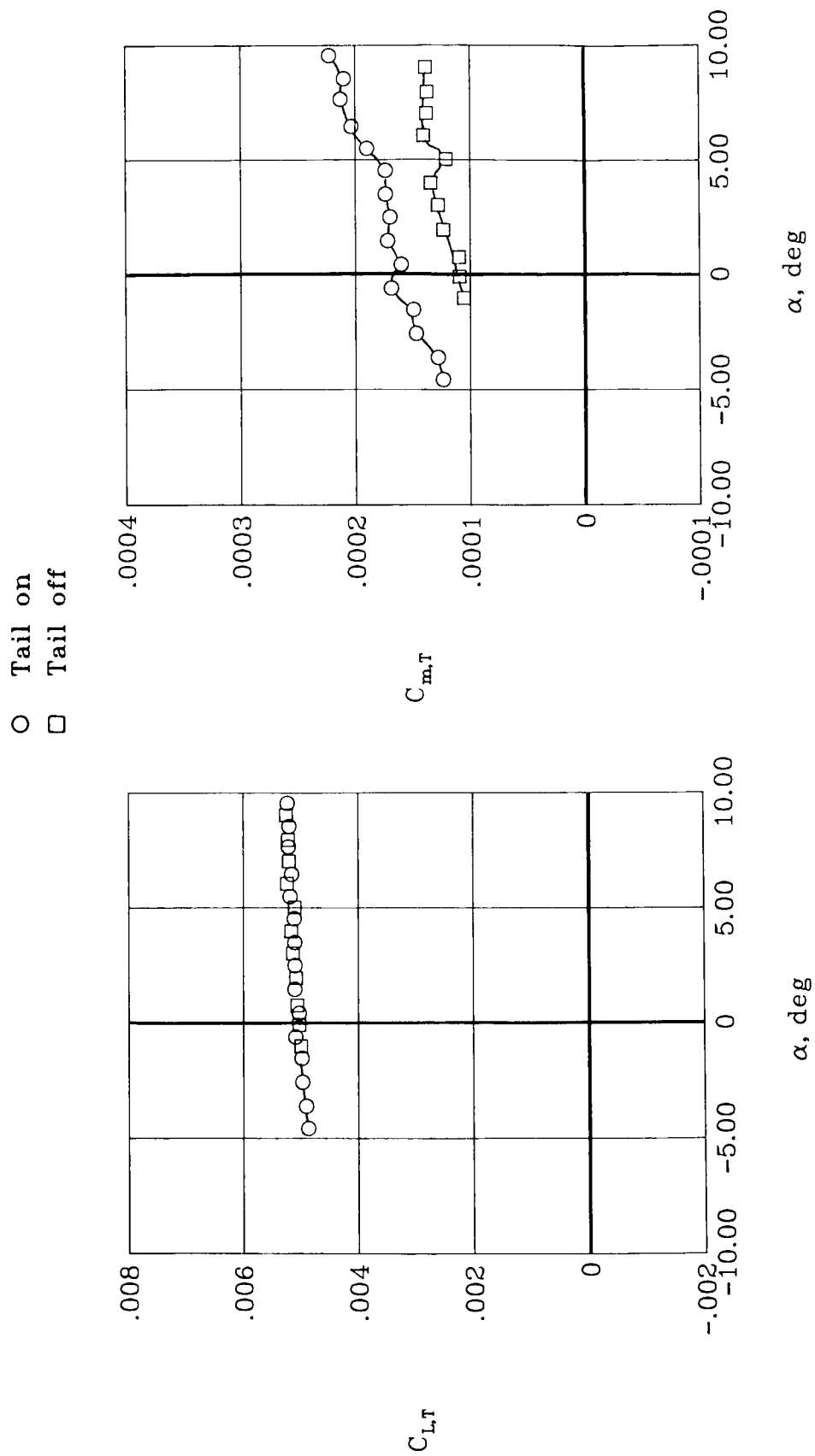
O Tail on
□ Tail off

(a) $\mu = 0.04$.

Figure 23. Effect of horizontal tail on airframe longitudinal aerodynamic characteristics. MMS off.
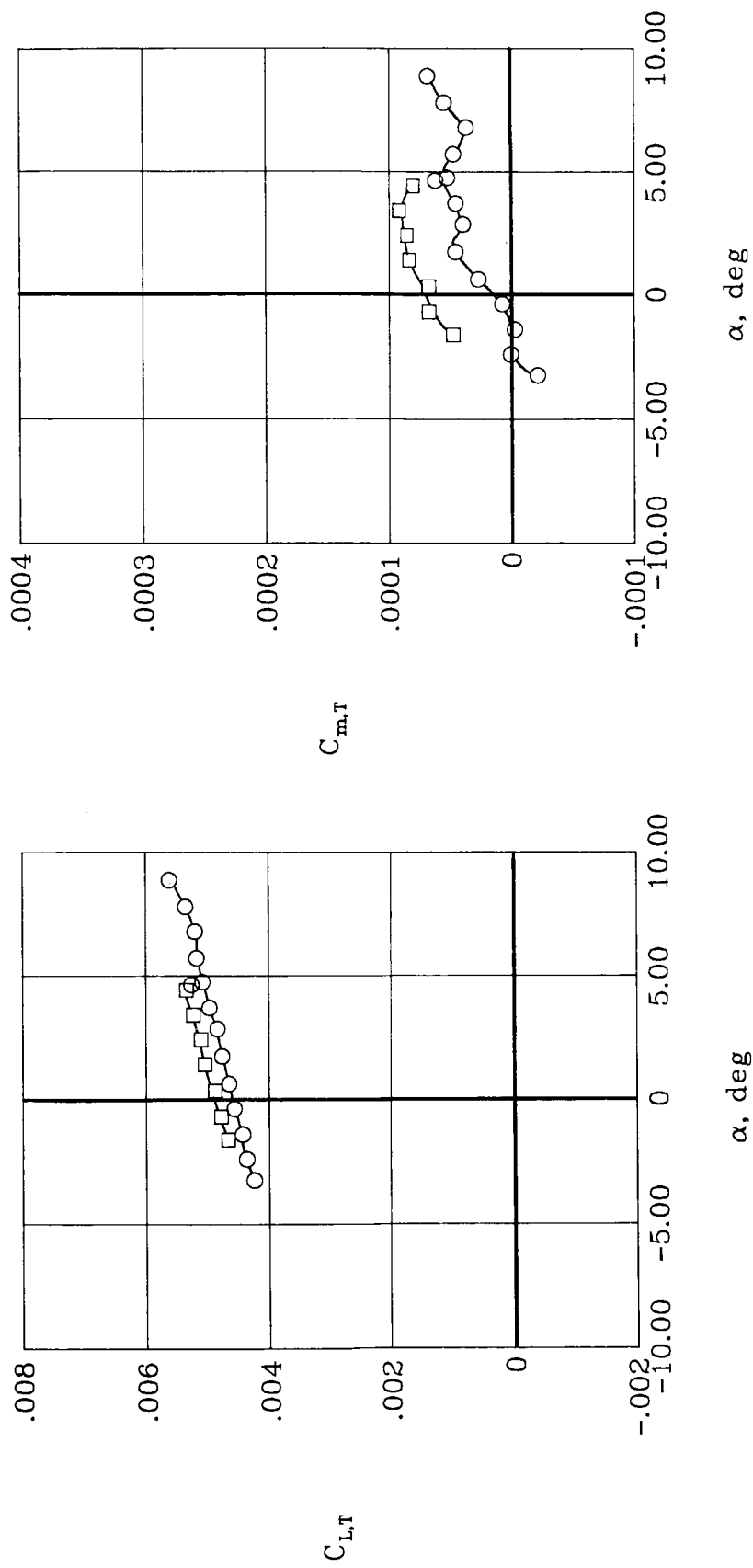
O Tail on
□ Tail off

(b) $\mu = 0.10$.

Figure 23. Continued.

(c) $\mu = 0.15$. Continued.

Figure 23. Continued.

O   Tail on
□   Tail off

$C_{m,T}$

$C_{L,T}$

α, deg

α, deg
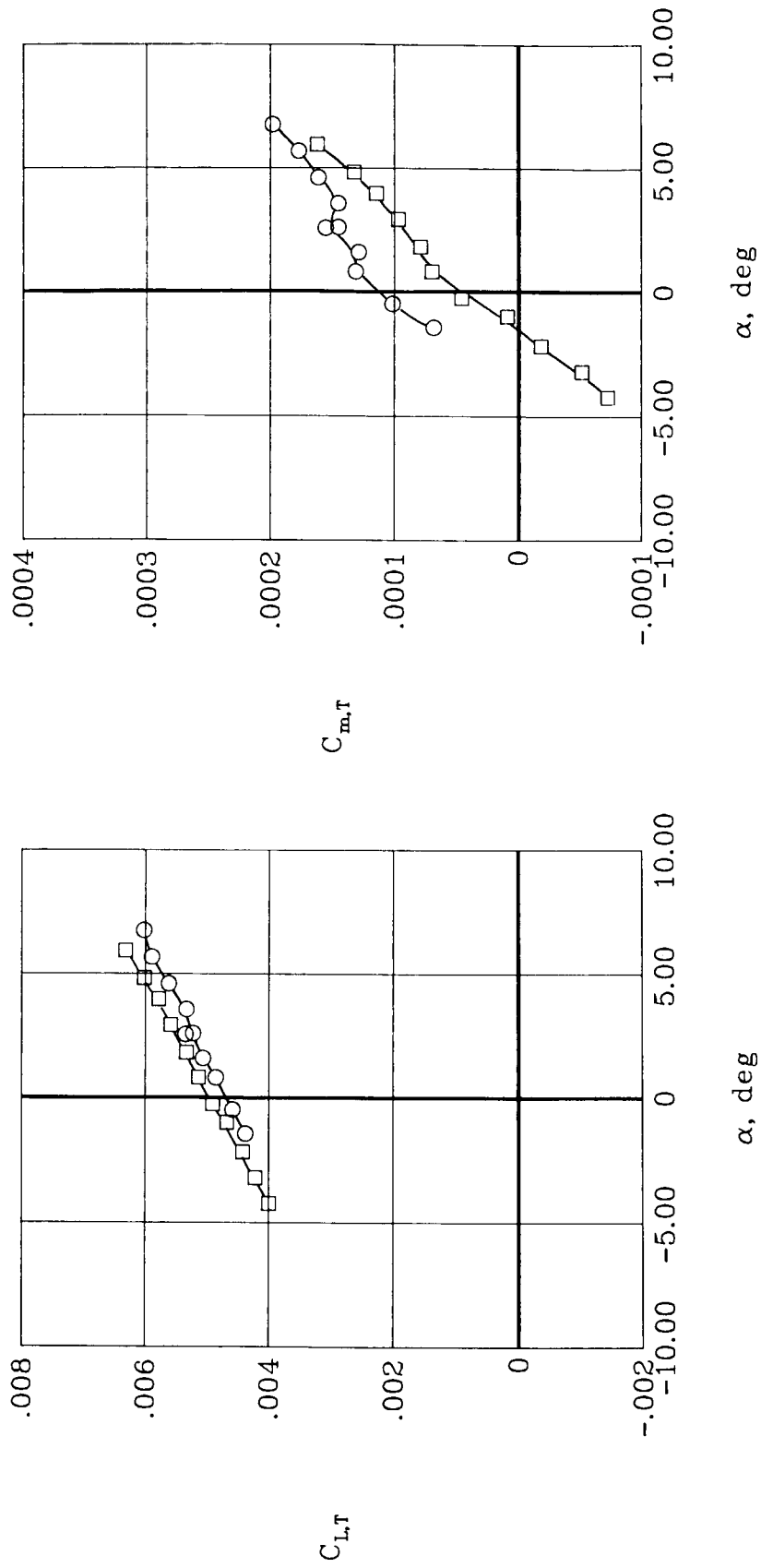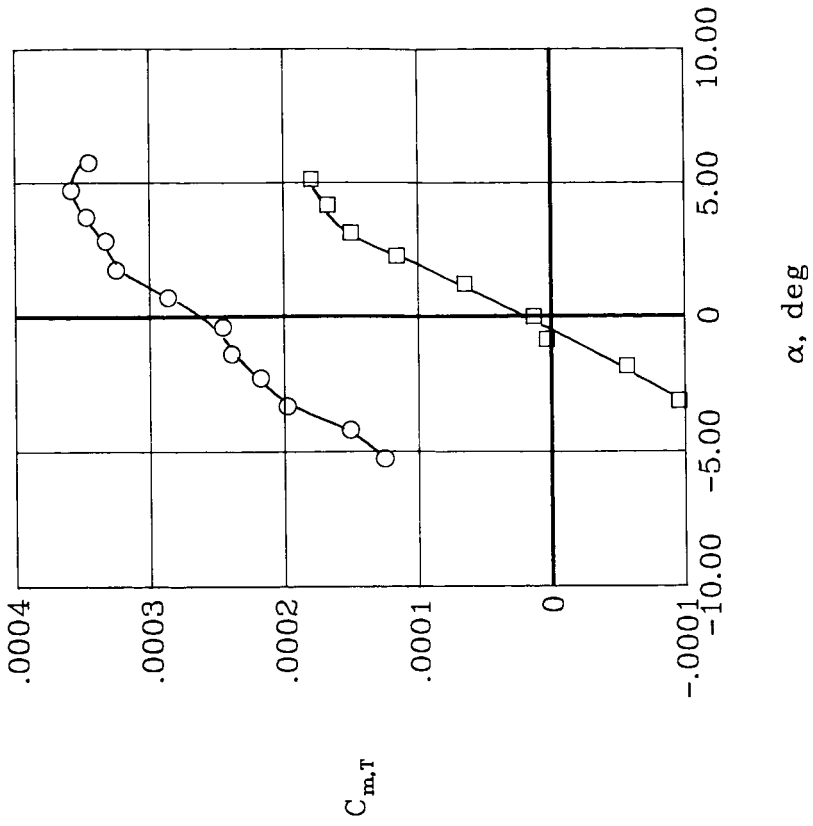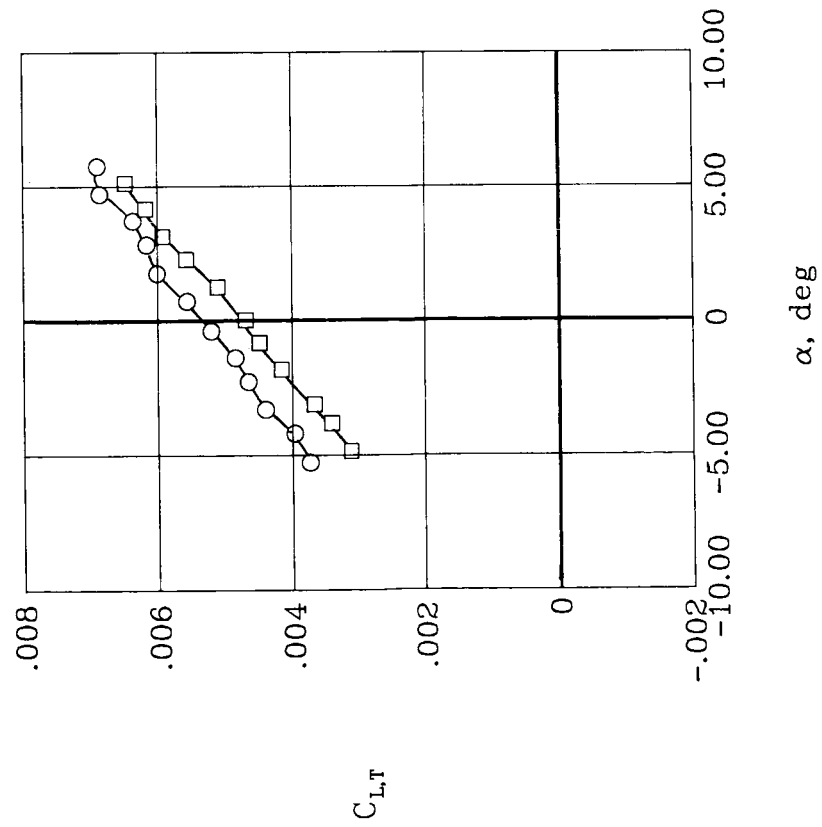
(d) $\mu = 0.20$.

Figure 23. Concluded.
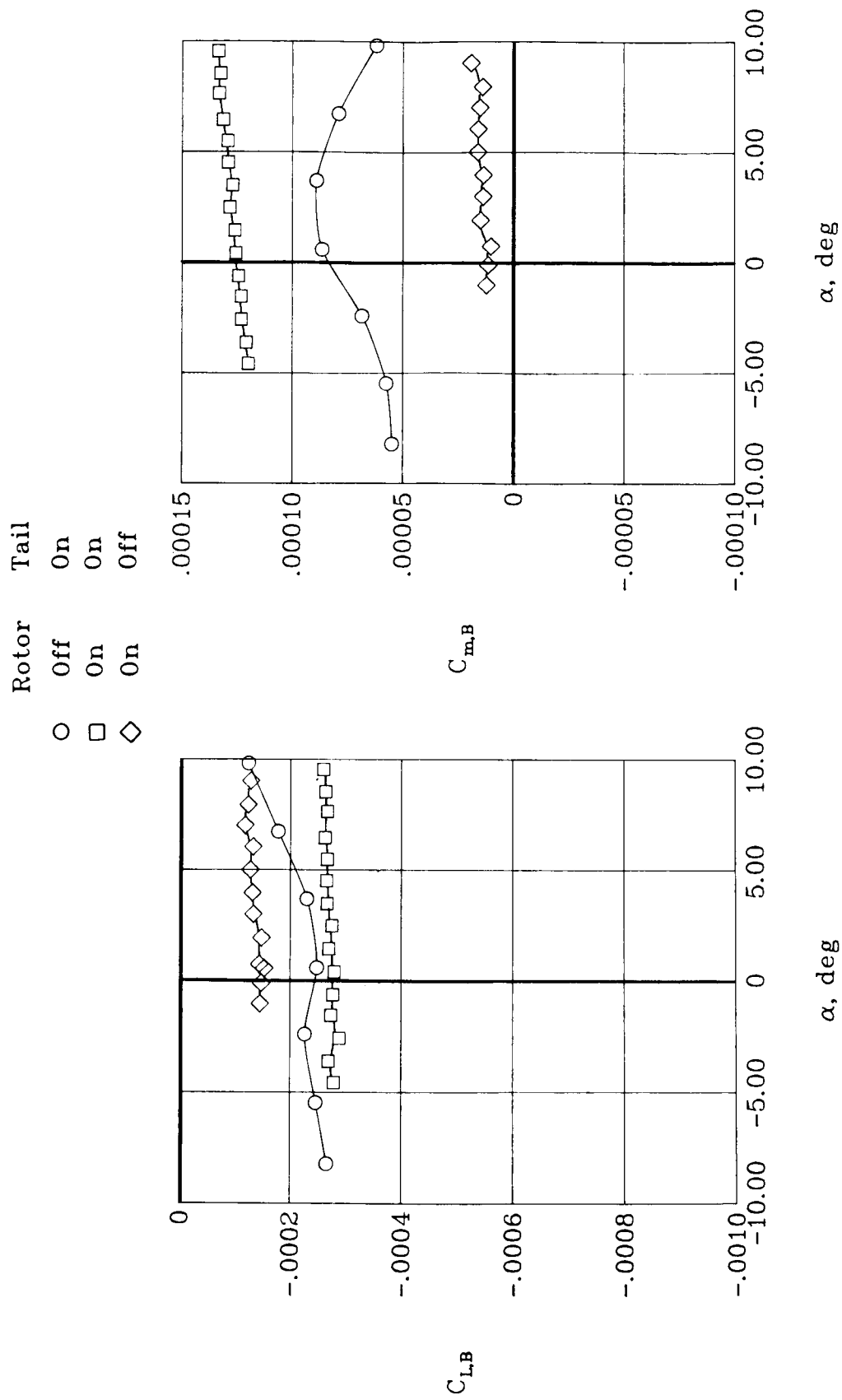
Figure 24. Effect of horizontal tail on airframe longitudinal aerodynamic characteristics. MMS off.
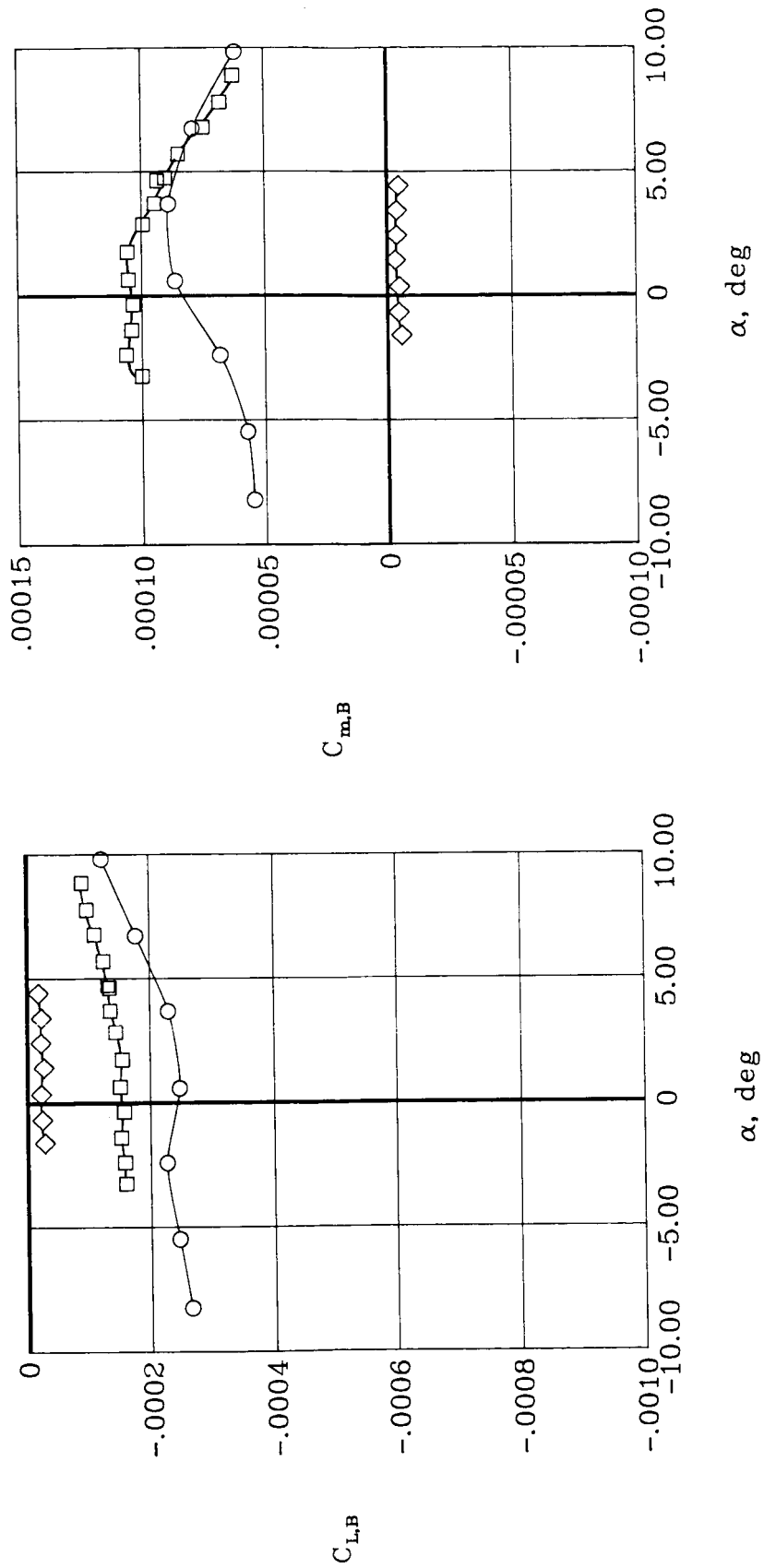
(a) $\mu = 0.04$.

(b) $\mu = 0.10$.

Figure 24. Continued.
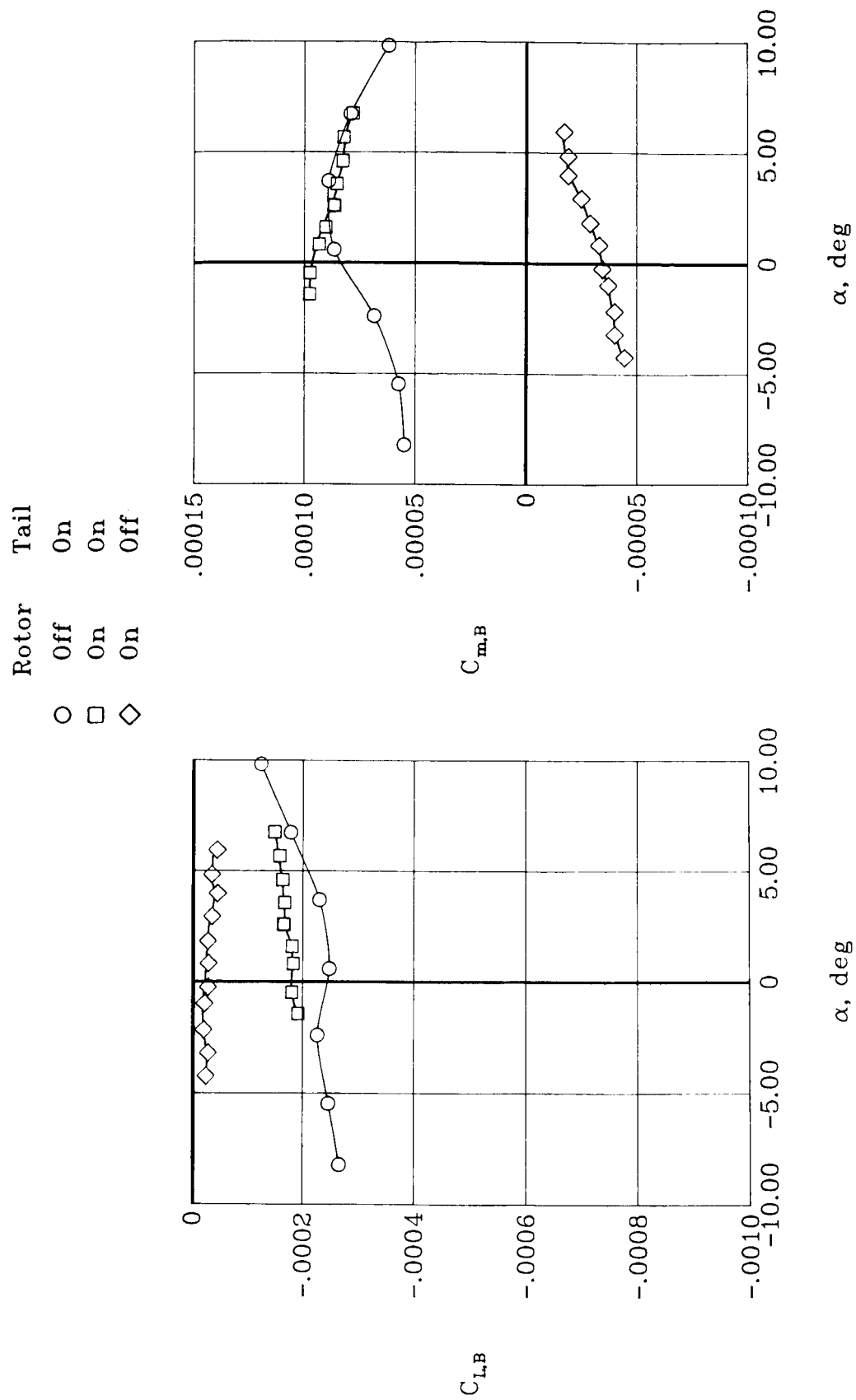
(c) $\mu = 0.15$.

Figure 24. Continued.
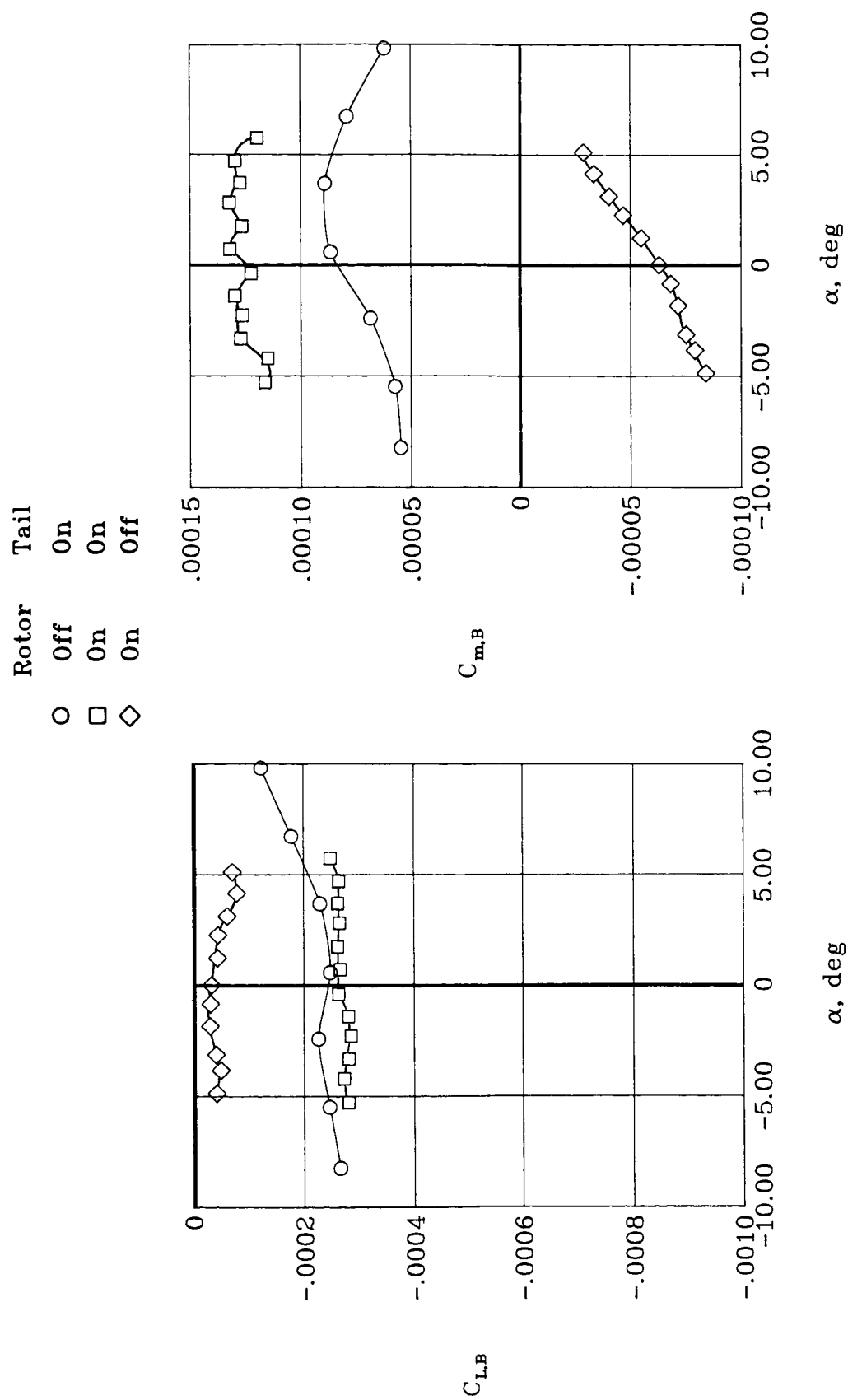
(d) $\mu = 0.20$.

Figure 24. Concluded.
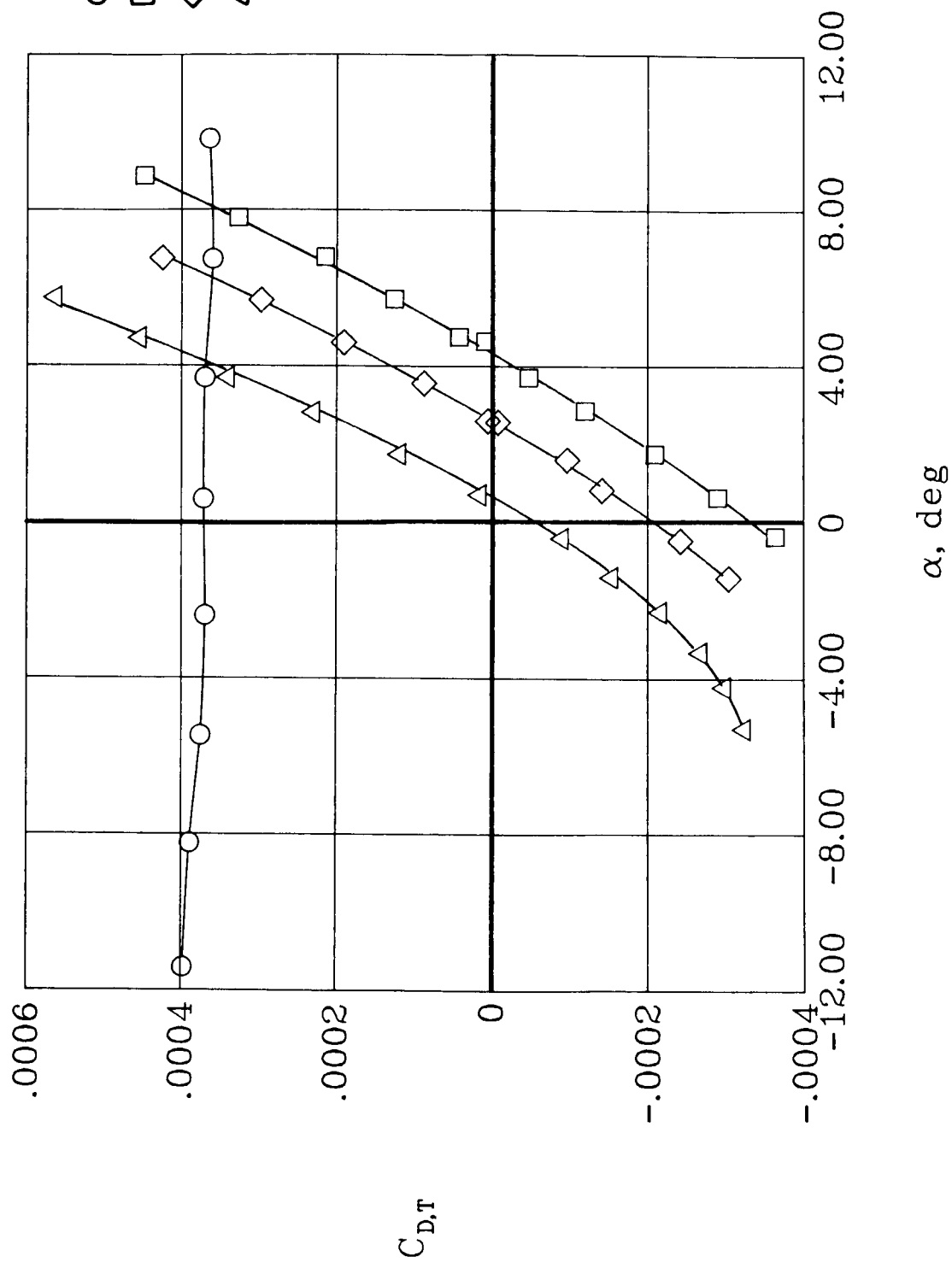
Figure 25. Total drag characteristics of model. MMS off.
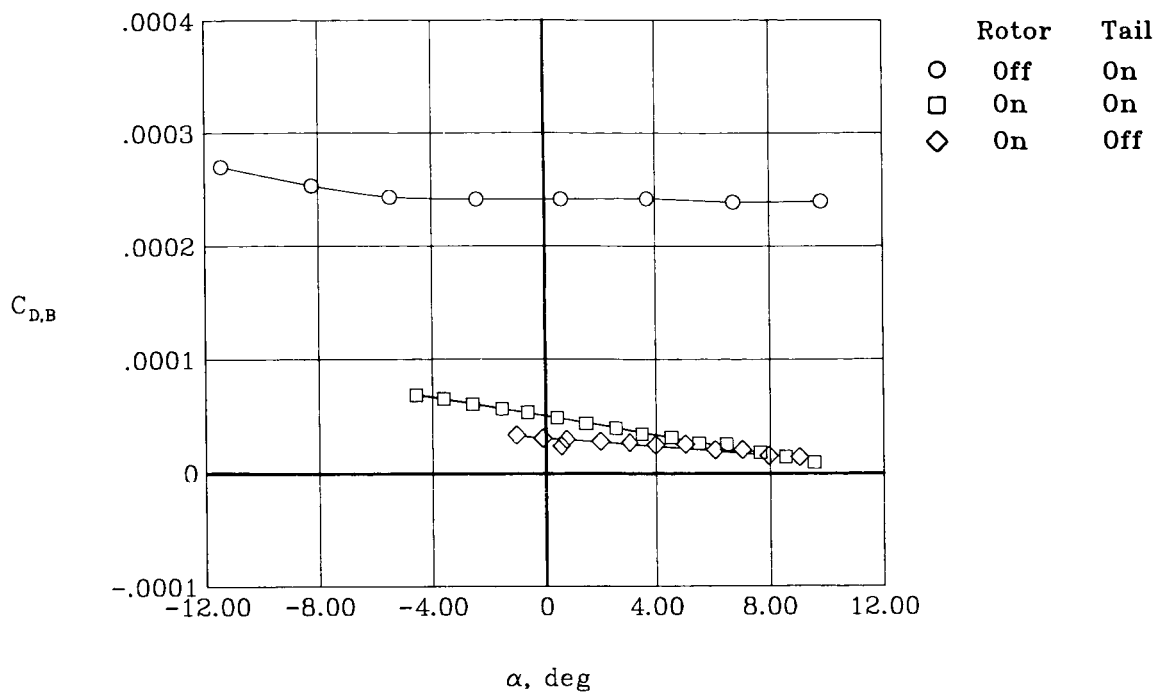
(a) $\mu = 0.04$.
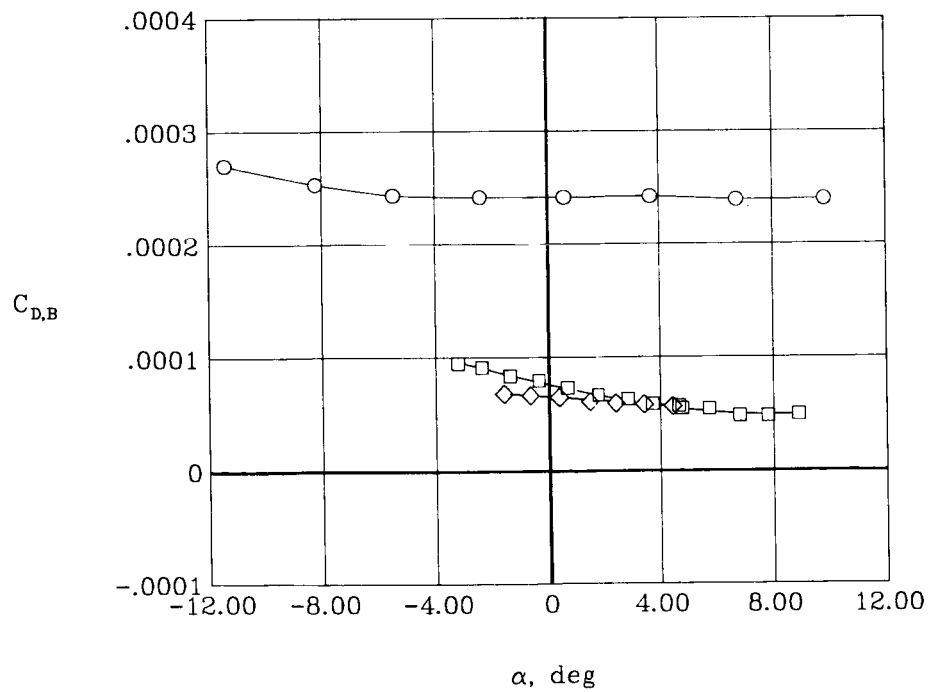
(b) $\mu = 0.10$.

Figure 26. Effect of horizontal tail on airframe drag characteristics. MMS off.
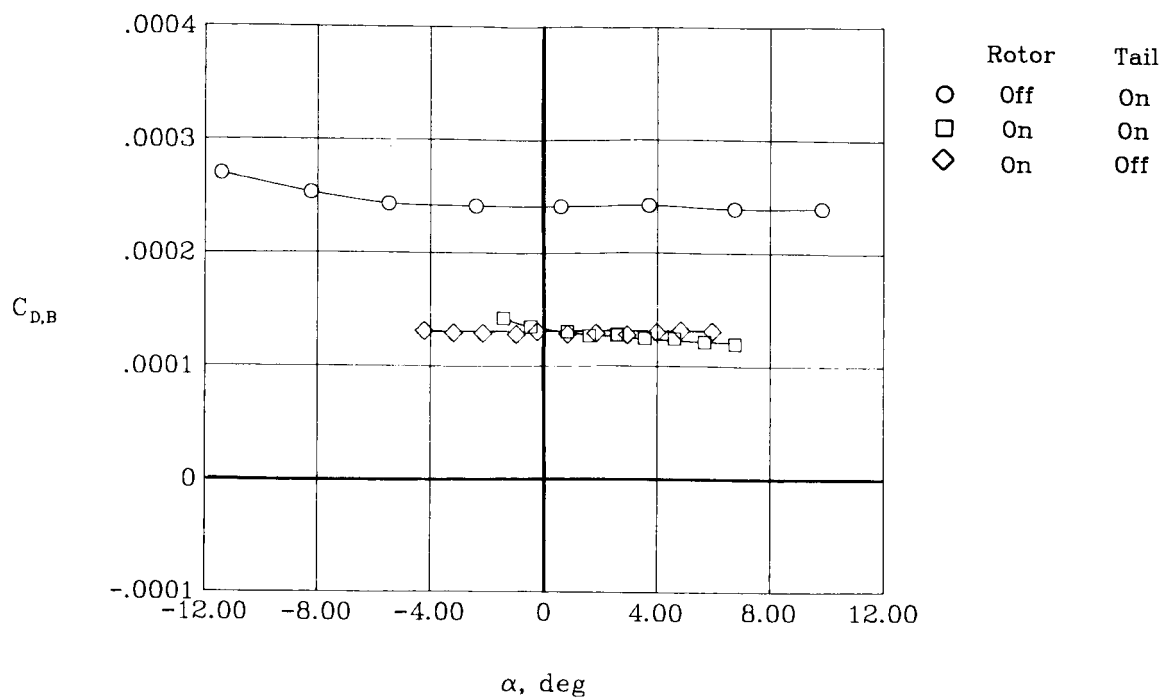
(c) $\mu = 0.15$.
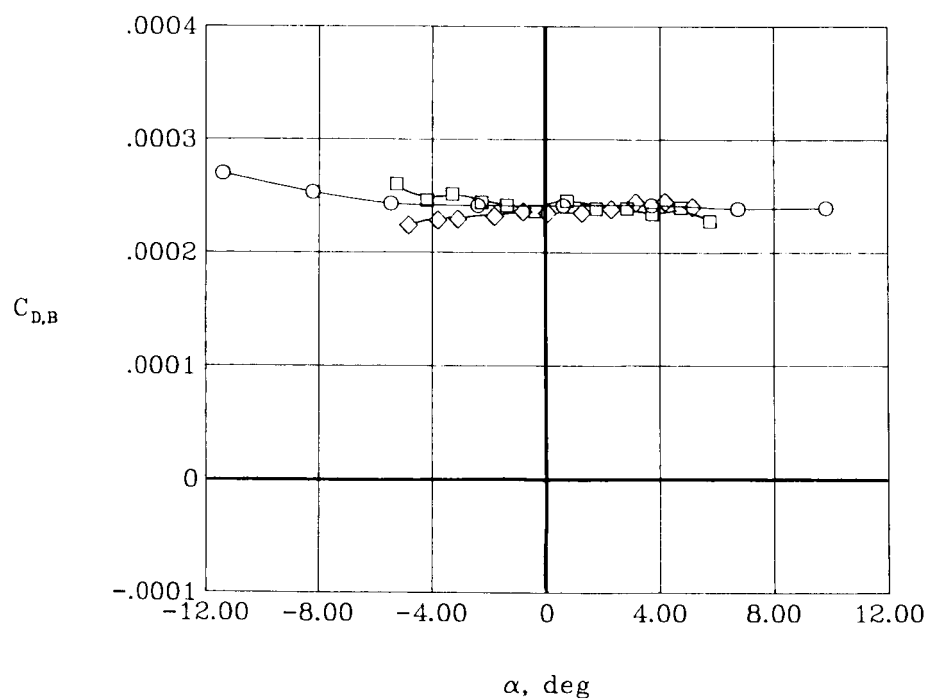
(d) $\mu = 0.20$.

Figure 26. Concluded.
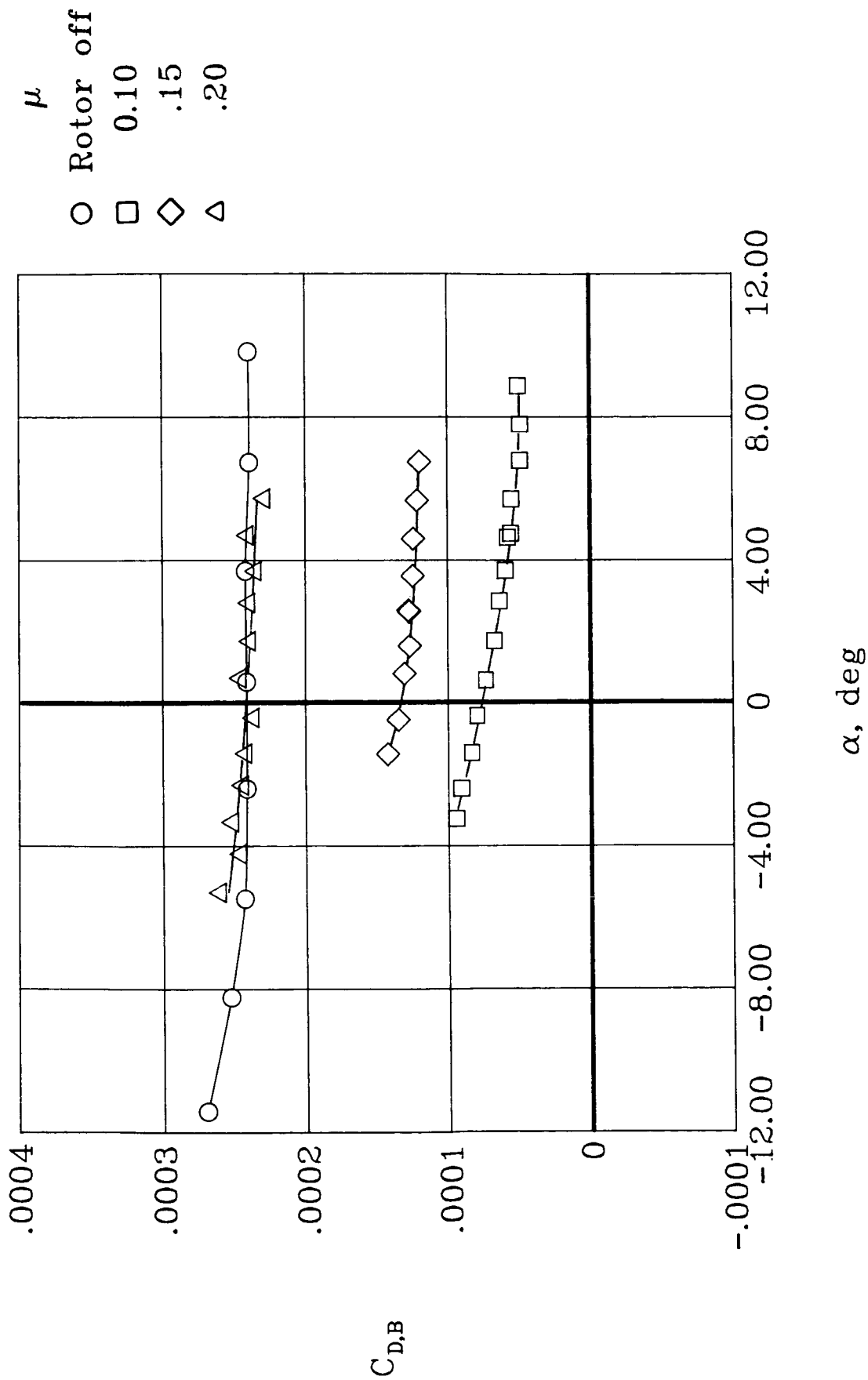
Figure 27. Summary of airframe drag characteristics. Tail on.

μ

○ Rotor off
□ 0.10
◇ .15
◁ .20
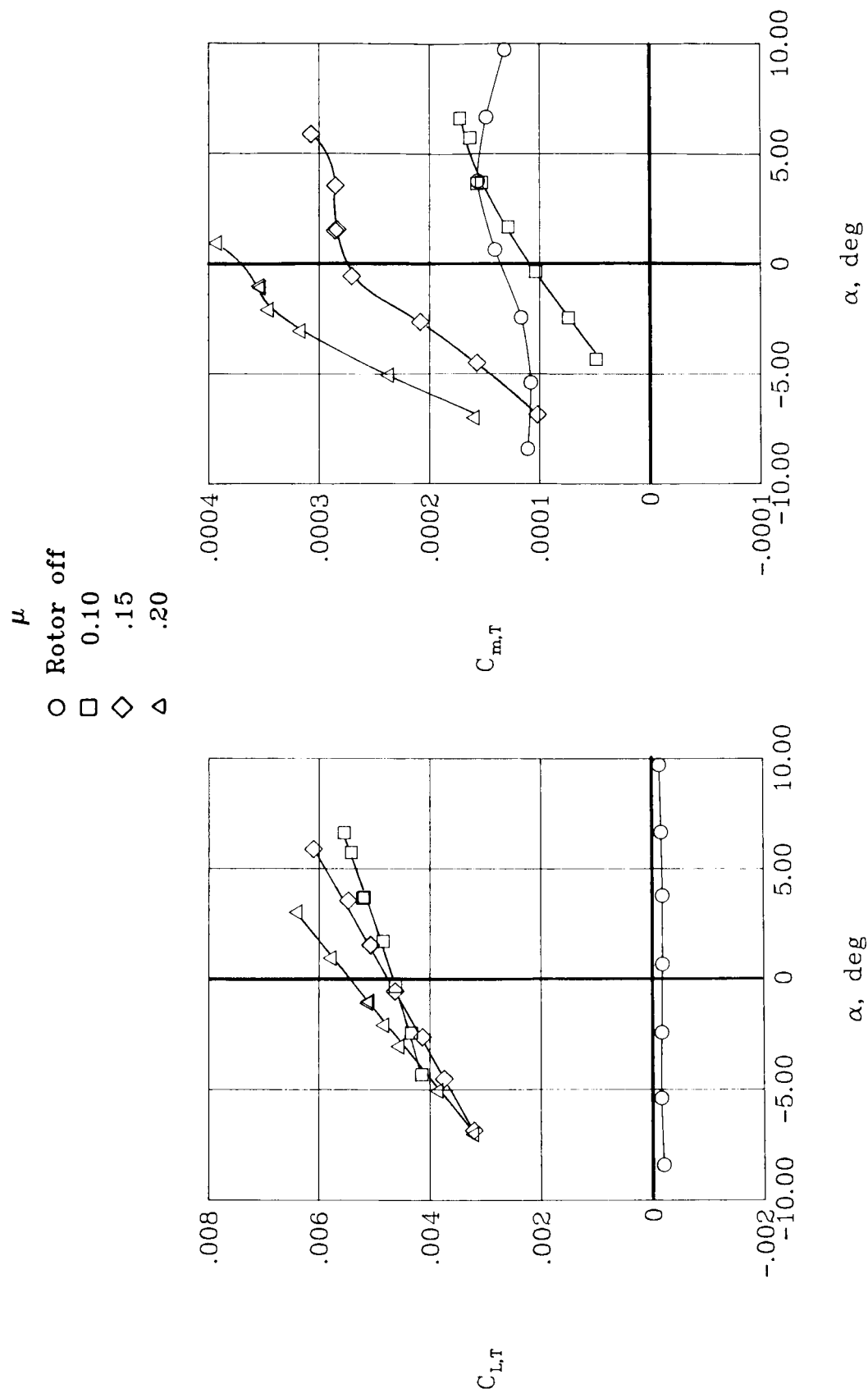
(a) Lift and pitching-moment characteristics.

Figure 28. Total longitudinal aerodynamic characteristics of model. MMS on.
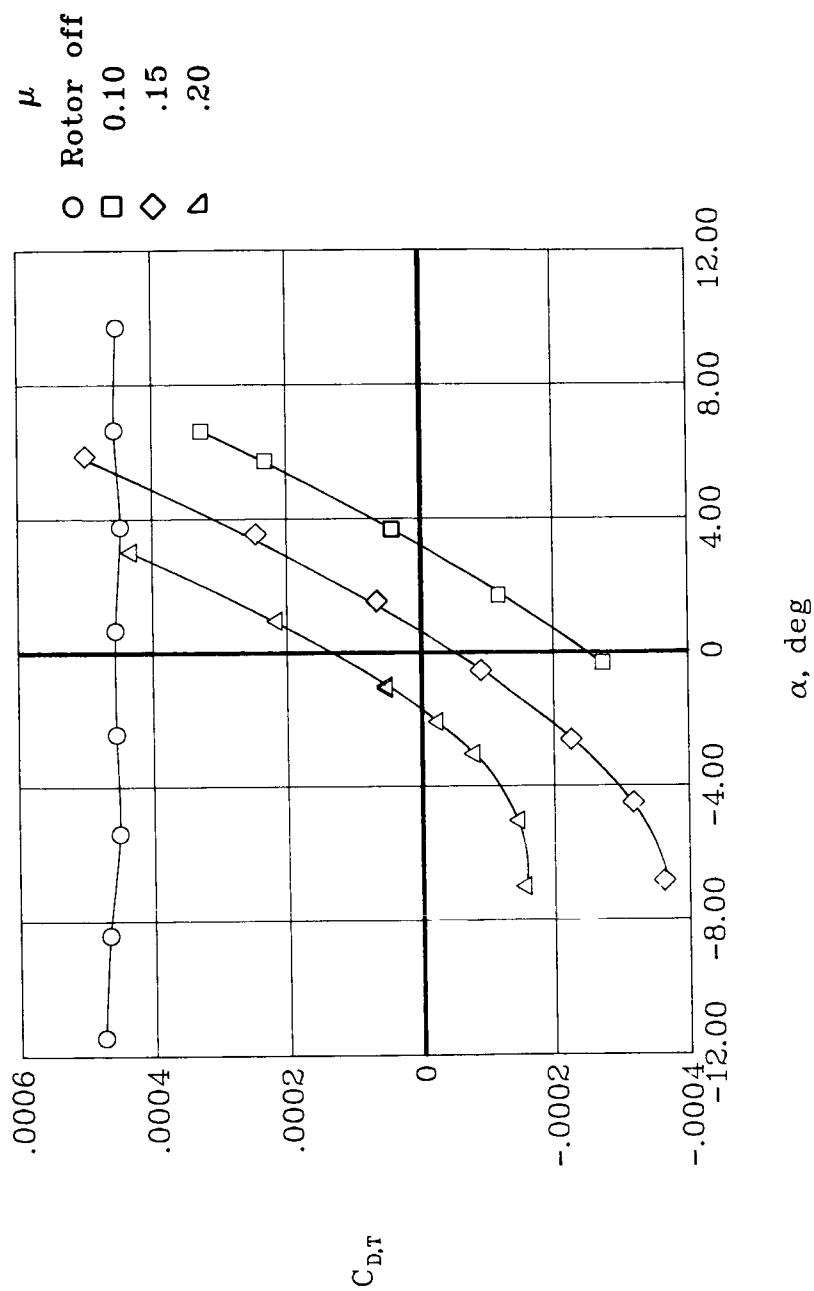
(b) Drag characteristics.

Figure 28. Concluded.
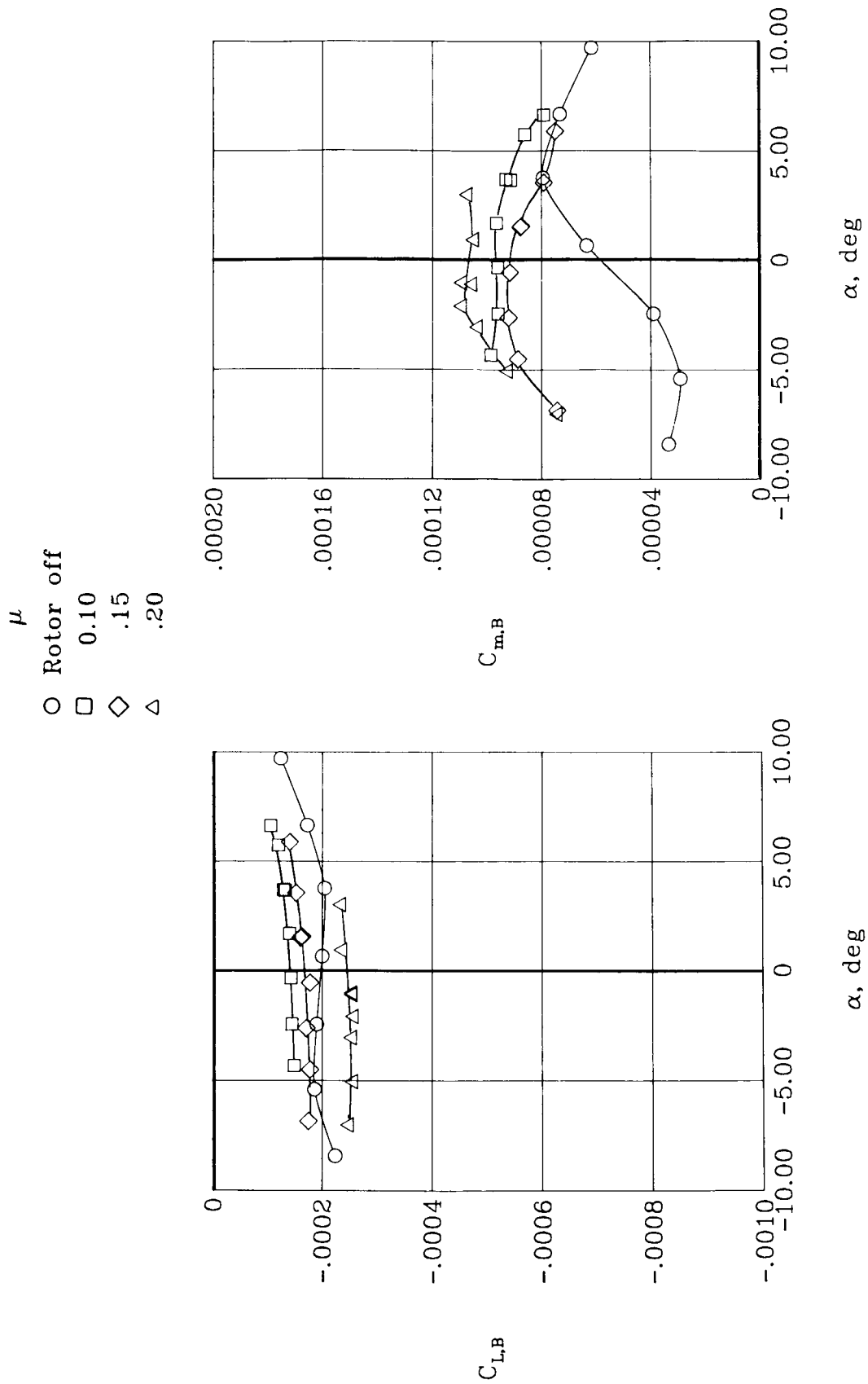
(a) Lift and pitching-moment characteristics.

Figure 29. Airframe longitudinal aerodynamic characteristics of model. MMS on.
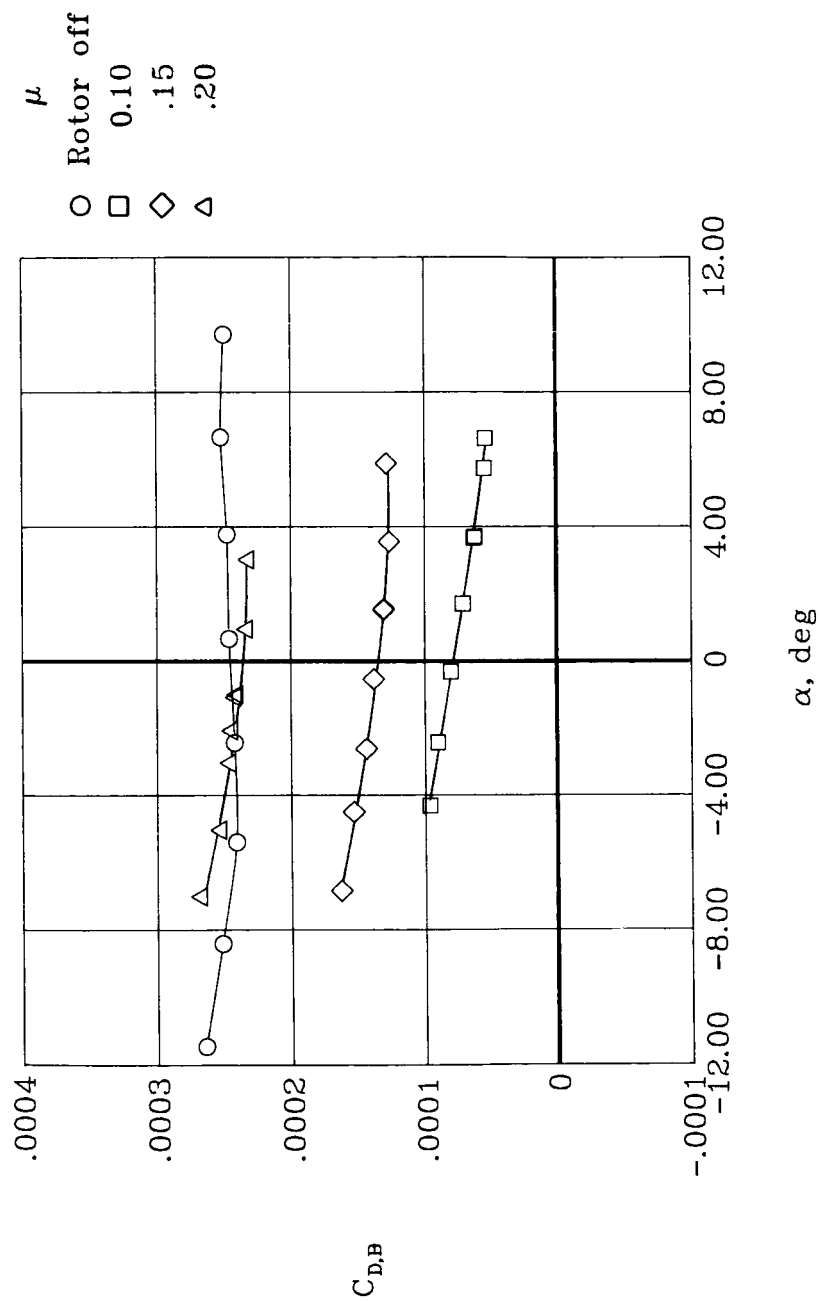
(b) Drag characteristics.

Figure 29. Concluded.
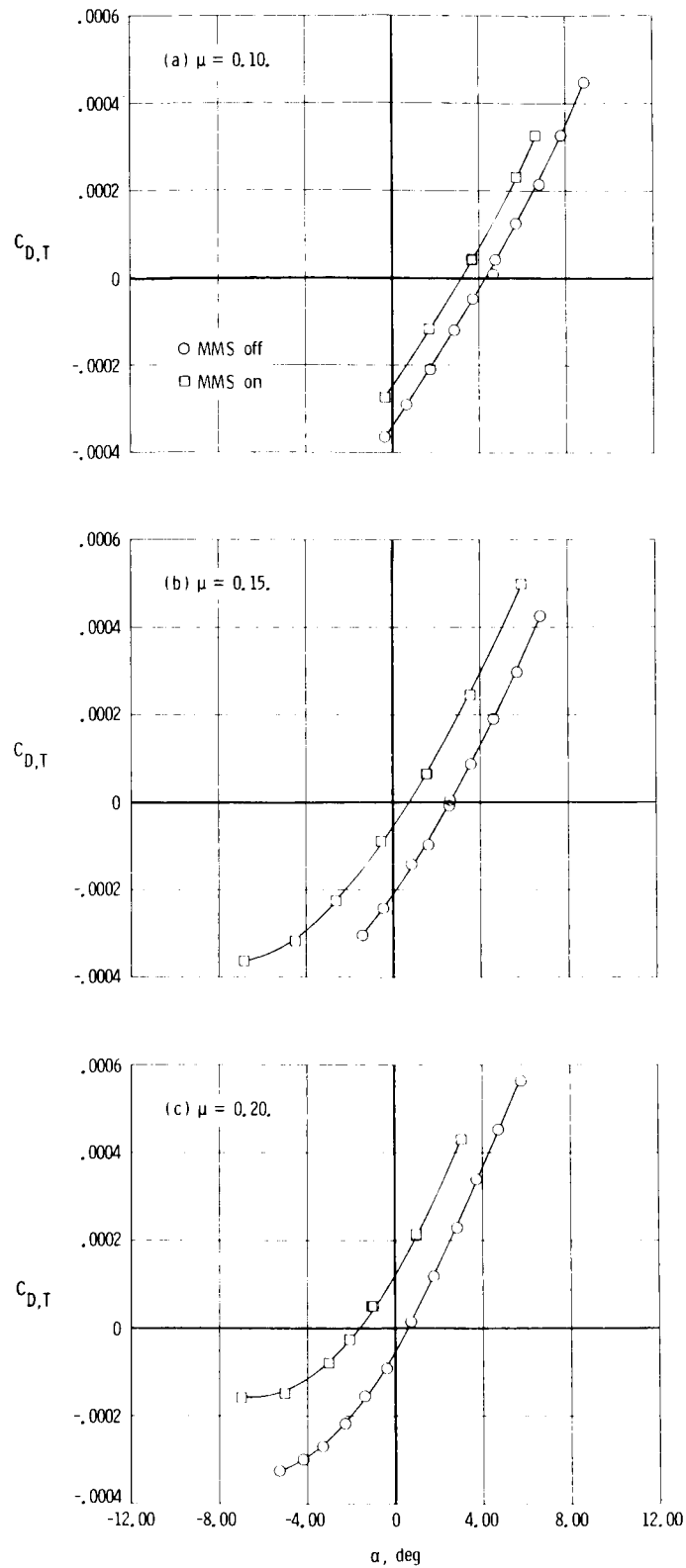
Figure 30. Effect of MMS on total drag of model with rotor on.
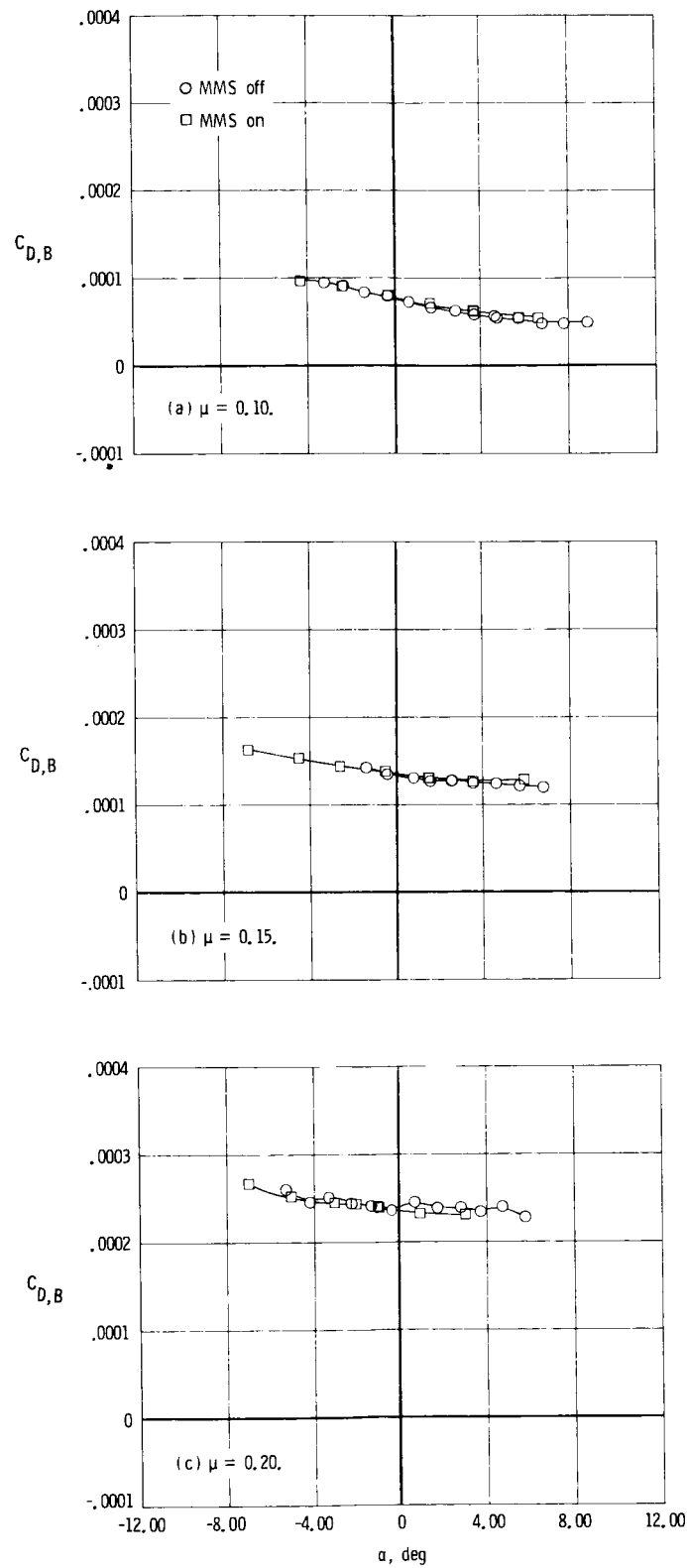
Figure 31. Effect of MMS on airframe drag with rotor on.
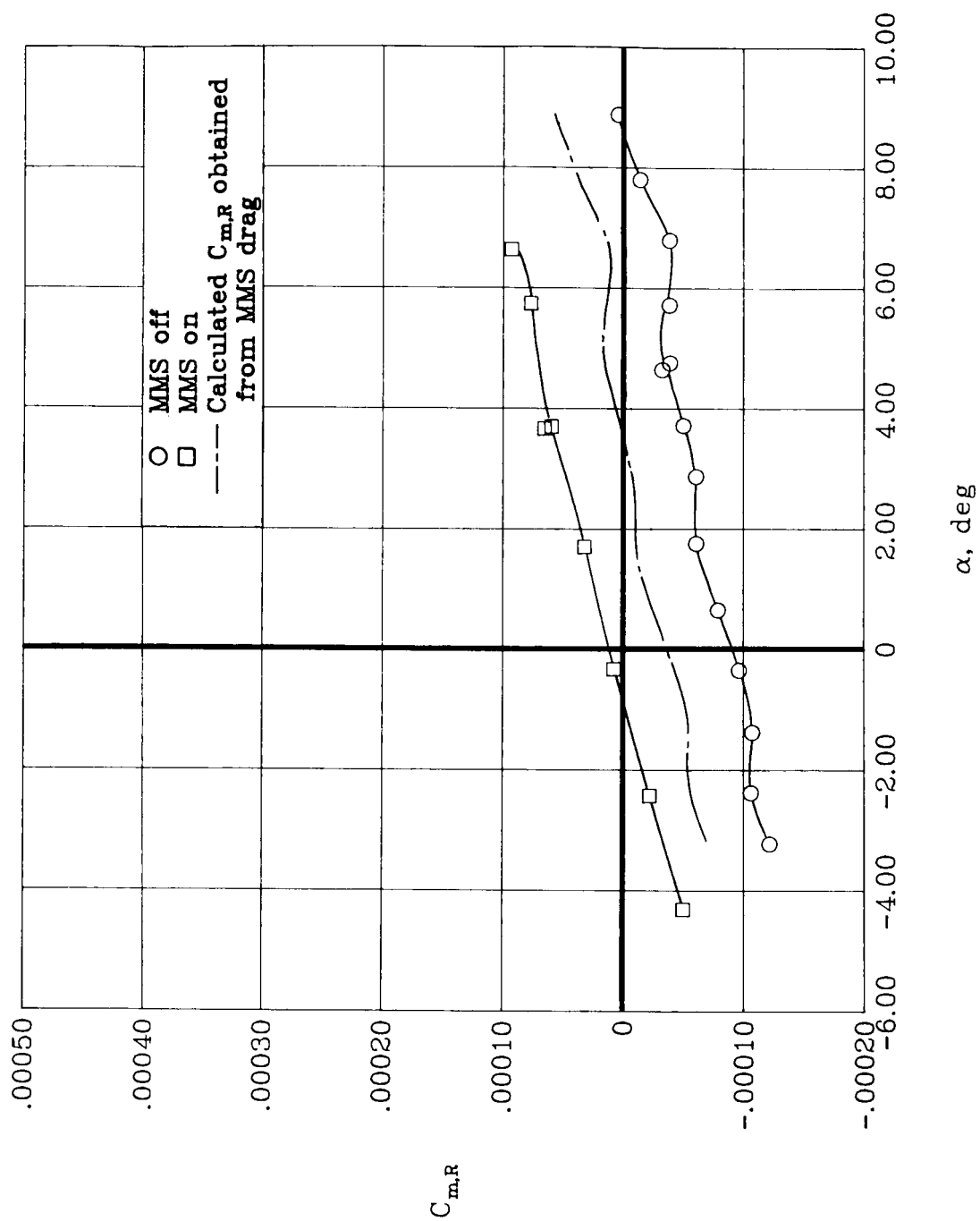
Figure 32. Effect of MMS on rotor pitching moment.

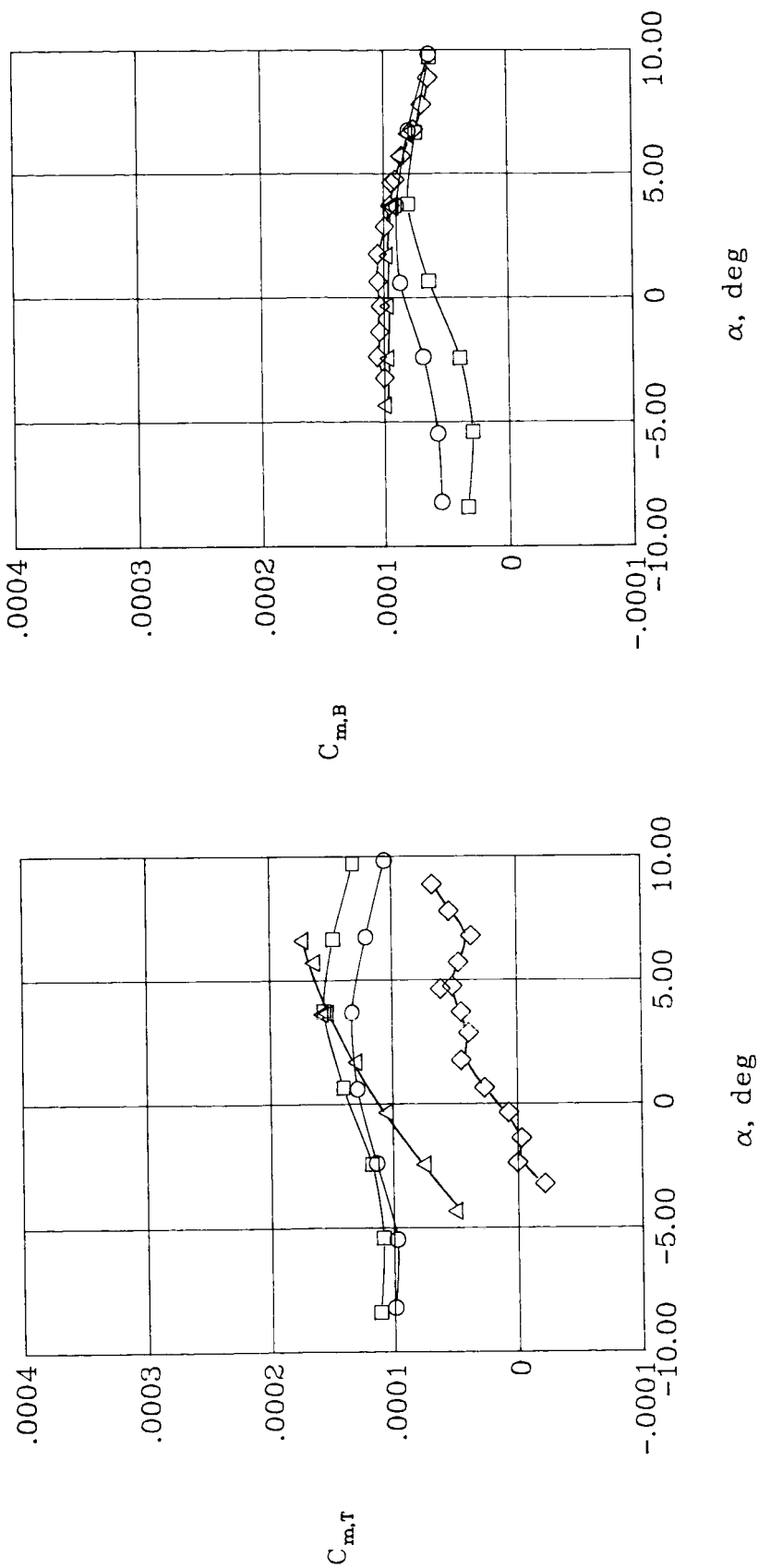(a) $\mu = 0.10$.
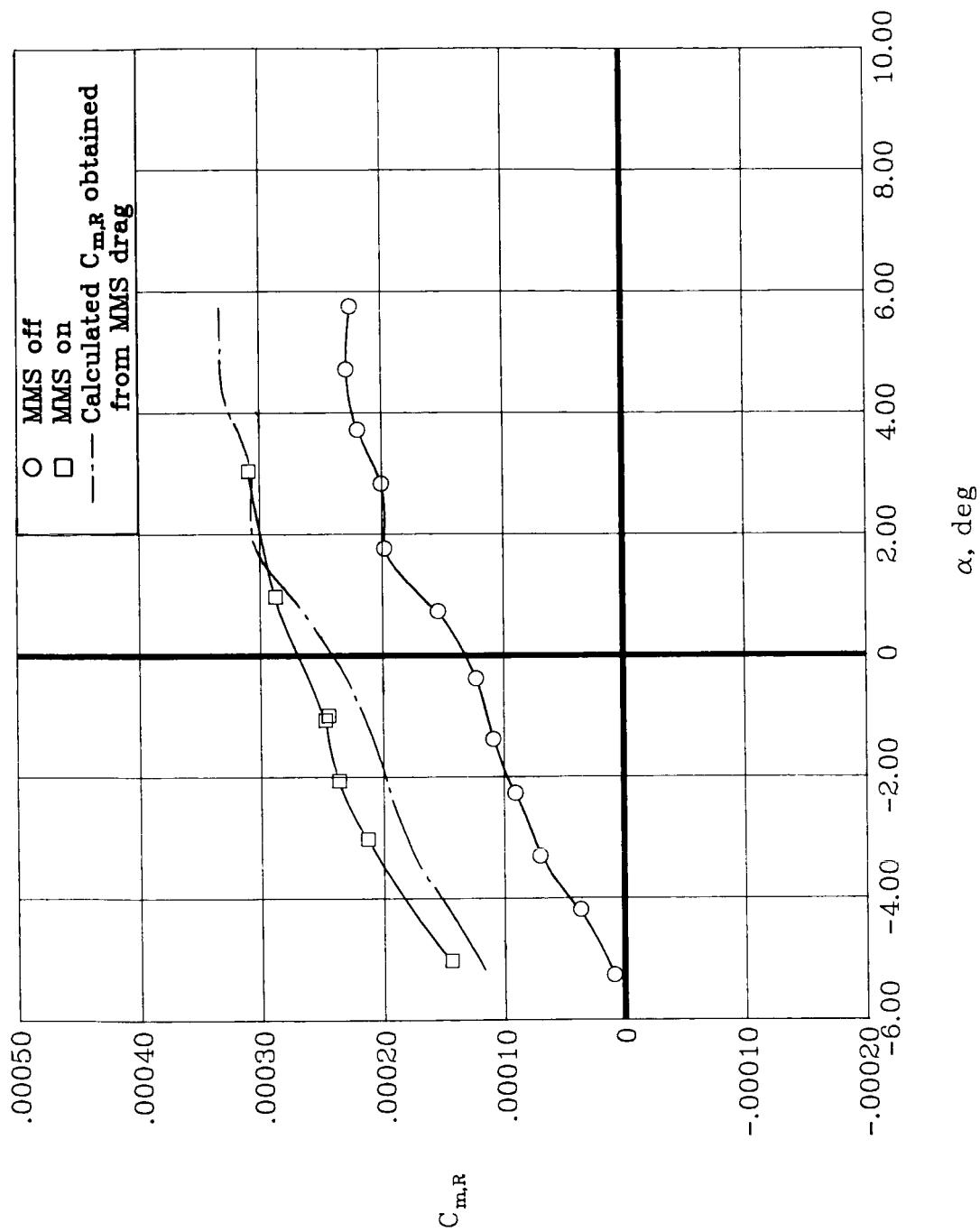
(b) $\mu = 0.20$.

Figure 32. Concluded.
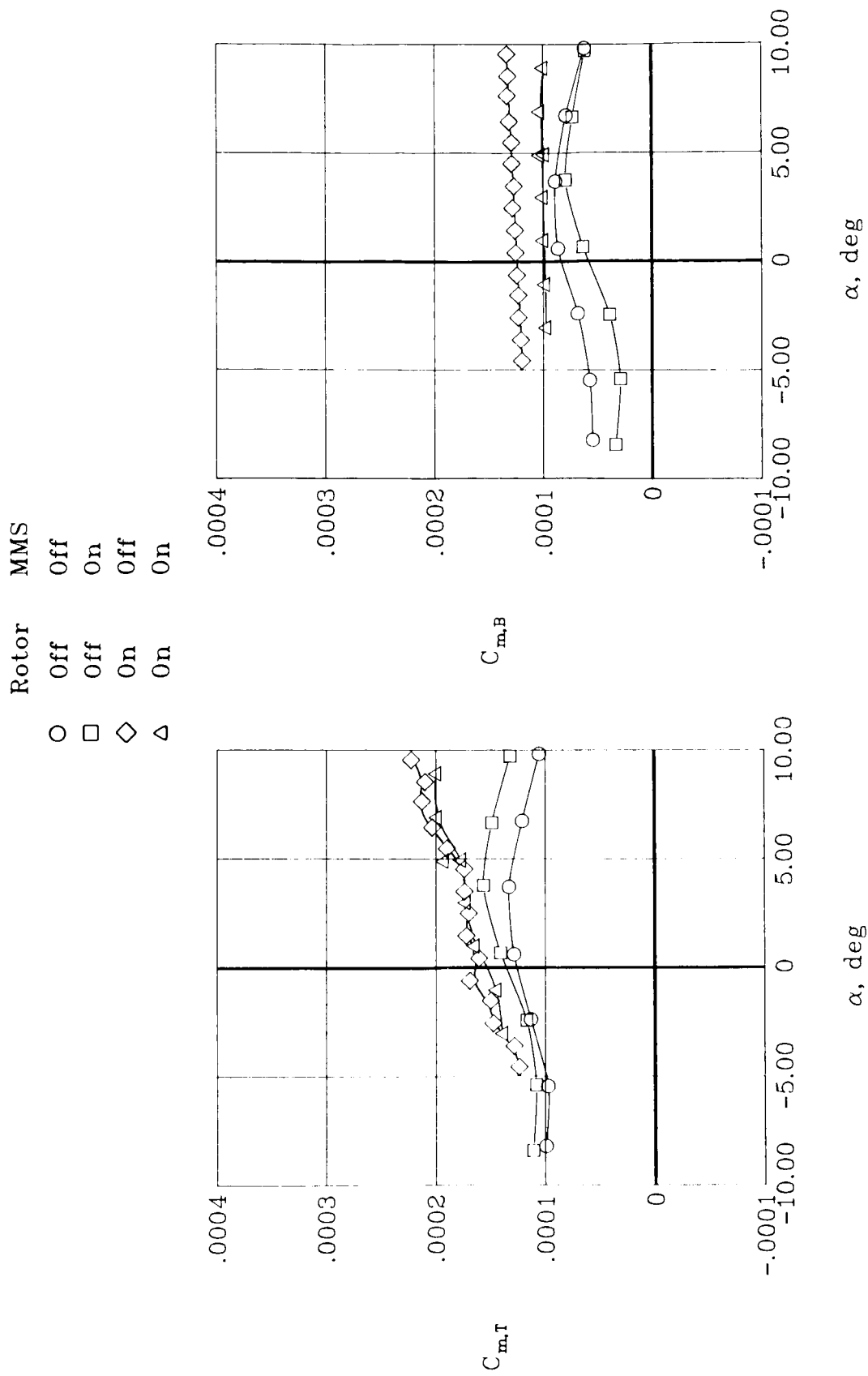
Figure 33. Effect of MMS on pitching-moment characteristics of model.

(a) $\mu = 0.04$.

Figure 33. Continued.

(b) $\mu = 0.10$.

(c) $\mu = 0.15$.

Figure 33. Continued.

	Rotor	MMS
○	Off	Off
□	Off	On
◇	On	Off
◁	On	On
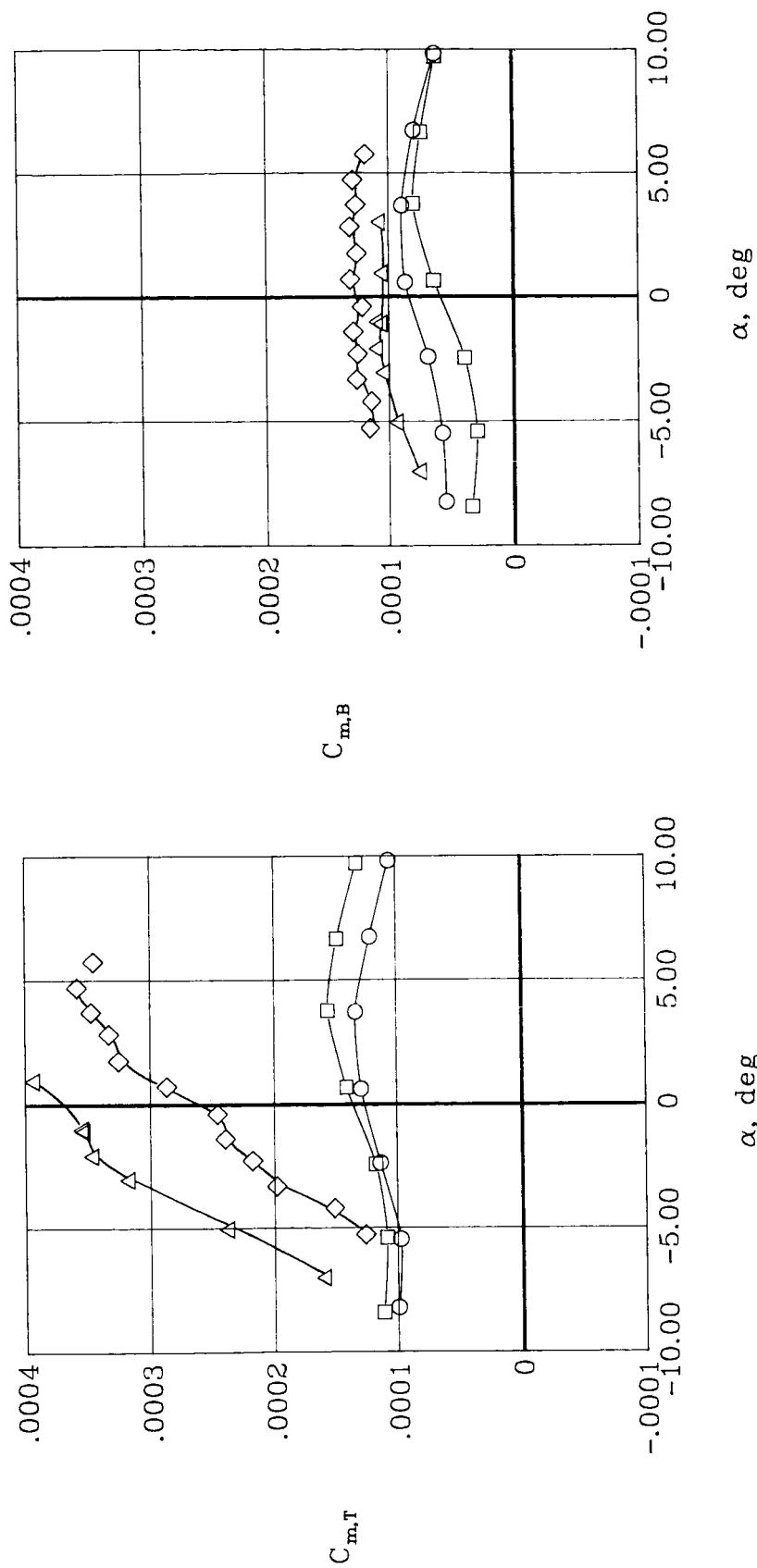
(d) $\mu = 0.20$.

Figure 33. Concluded.

1. Report No. NASA TP-2420 AVSCOM TR 85-B-2	2. Government Accession No.	3. Recipient's Catalog No.
4. Title and Subtitle Wind-Tunnel Evaluation of a 21-Percent-Scale Powered Model of a Prototype Advanced Scout Helicopter		5. Report Date June 1985
		6. Performing Organization Code 505-45-43-02
7. Author(s) Arthur E. Phelps III and John D. Berry		8. Performing Organization Report No. L-15895
9. Performing Organization Name and Address Structures Laboratory USAAVSCOM Research and Technology Laboratories NASA Langley Research Center Hampton, VA 23665		10. Work Unit No.
		11. Contract or Grant No.
12. Sponsoring Agency Name and Address National Aeronautics and Space Administration Washington, DC 20546 and U.S. Army Aviation Systems Command St. Louis, MO 63120		13. Type of Report and Period Covered Technical Paper
		14. Army Project No. 1L162209AH76

16. Abstract

An exploratory wind-tunnel investigation of a 21-percent-scale powered model of a prototype advanced scout helicopter was conducted in the Langley 4- by 7-Meter Tunnel. The investigation was conducted to define the overall aerodynamic characteristics of the Army Helicopter Improvement Program (AHIP), to determine the effects of the rotor on the aerodynamic characteristics, and to evaluate the effect of a mast-mounted sight on the aircraft stability characteristics. Tests covered a range of thrust coefficients, advance ratios, angles of attack, and angles of sideslip and were run for both rotor-on and rotor-off configurations. Results of the investigation showed that the prototype configuration was longitudinally unstable with angle of attack for all configurations tested. The instability was due to unfavorable interference effects between the horizontal tail and the wake shed from the engine pylon and rotor hub, which caused a loss of horizontal-tail effectiveness. The addition of the mast-mounted sight had little effect on the stability of the model, but it caused an alteration in the rotor lift distribution that resulted in substantial interference drag for the sight.

17. Key Words (Suggested by Authors(s)) Scout helicopter Mast-mounted sight Powered rotor testing Rotor interference effects	18. Distribution Statement Unclassified Unlimited Subject Category 02
19. Security Classif.(of this report) Unclassified	20. Security Classif.(of this page) Unclassified	21. No. of Pages 74	22. Price A04

THIRD-CLASS BULK RATE

4   2 IU,A,   850020 5001010SR
DEPT OF THE AIR FORCE
ARNOLD ENG DEVELOPMENT CENTER(AFSC)
ATTN: LIBRARY/DOCUMENTS
ARNOLD AF STA TN 37389

NASA